Supernovae Interacting with their Circumstellar Medium

Bob van Veelen

ISBN 978-90-393-5436-0

Cover image: A breaking wave due to the interaction of the wave with the shore. Similar to the subject of this thesis, this process is described by hydrodynamics.

Supernovae Interacting with their Circumstellar Medium

De Interactie van Supernovae met hun omgeving

(met een samenvatting in het Nederlands)

Proefschrift

ter verkrijging van de graad van doctor aan de Universiteit Utrecht op gezag van de rector magnificus, prof.dr. J. C. Stoof, ingevolge het besluit van het college voor promoties in het openbaar te verdedigen op 19 november 2010 des ochtends te 10.30 uur

door

Bob van Veelen

geboren op 22 mei 1983 te Nijmegen

Promotor: Prof.dr. N. Langer

Contents

Chapter 1

Introduction

1.1 General

The night sky is not as static as once thought. Even though looking to the stars gives the impression that the night sky does not change, everything in the universe is most certainly in motion. While most events in the universe take place on such long time scales that we do not see any change within a human life time, there are events, typically more dramatic, which lead to changes in a split second.

Among these most dramatic events are supernovae: exploding stars that outshine everything (even entire galaxies) for periods of days. In some cases they become bright enough to be visible with the naked eye. Historically, the appearance and disappearance of stars has put an end to the notion of a never changing universe. With time came knowledge and some of these 'new stars' are now known to be the end result of stellar evolution.

In this thesis we will look at the evolution of supernovae. More specifically, we will investigate how the star, prior to the explosion, affects its surrounding medium and therefore influences the evolution of the subsequent supernova explosion. Different types of supernovae are connected to different mass ranges, and therefore different evolutionary paths. This results in specific features in terms of the explosion energy, the ejected mass and the composition of the ejected mass, among other things. However, the progenitor evolution prior to the explosion also proceeds differently and has to be taken into account. By combining both the pre-supernova evolution of the circumstellar medium and the subsequent interaction with the supernova ejecta a better understanding can be gained regarding supernovae and their remnants.

1.2 Stellar evolution and winds

This thesis focuses on single massive stars, which start their lives with a mass greater than approximately 8 times the mass of the sun ($M_{\odot}$). Although less mas-

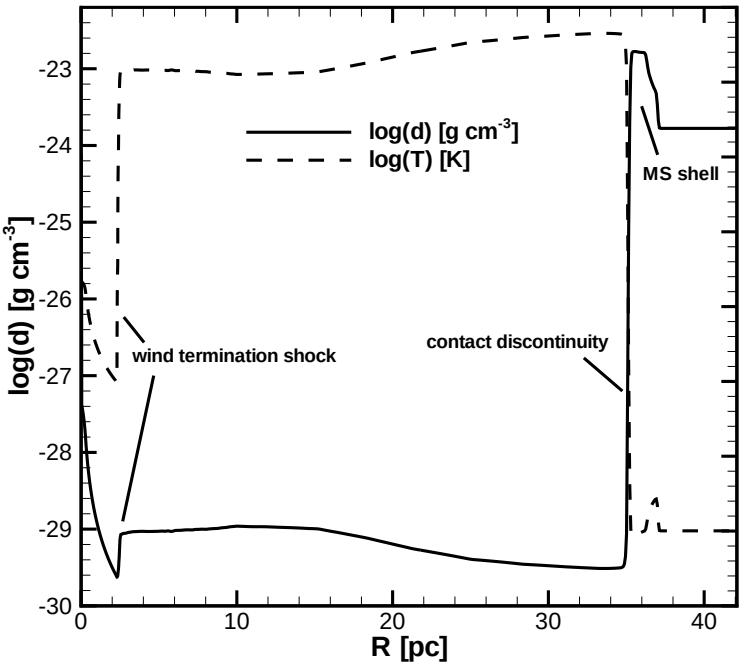

Figure 1.1: Example of density and temperature structure of the circumstellar medium at the end of the Main Sequence of a 9 $M_\odot$ star. The material surrounding the star which was first evenly distributed in the ISM, is now swept up into a cold, dense shell residing at 36 pc. The density in the interior region has dropped by roughly 5 orders of magnitude.

sive stars can also change their surroundings significantly, they do not explode as supernovae. The most important effect these stars have on their surroundings, prior to the supernova explosion, is through the influence of their stellar wind. Material is blown away from the stellar surface which alters the shape of the interstellar medium (ISM).

A star can lose a significant portion of its mass before exploding as a supernova. The mass loss rate and the velocity of the stellar wind are determined by the conditions at the surface of the star, which change strongly during its life. The link between the surface properties of the star and its evolutionary state couple the different phases in stellar evolution with different mass loss phases.

During the first $\sim 90\%$ of its life, a star fuses hydrogen in its core into helium, the main sequence (MS) phase. This process creates the energy which is needed to compensate for the energy loss at the surface of the star. The majority of this energy loss is caused by the emission of electromagnetic radiation. A part of this energy loss however is also due to the stellar wind.

During the MS phase, the star has a supersonic wind, which shocks and sweeps

up the ISM. The structure of the ISM during the MS phase can be separated into four different zones (see Fig.1.1). Moving from the outside inward we first find the undisturbed ISM. In the next zone, the swept up and shocked material from the surroundings of the star is accumulated into a cold dense shell, called the MS shell. This shell of shocked circumstellar material is separated from the third zone by a contact discontinuity[1], which consists of shocked stellar wind. The shocked wind material has a very low density compared to the MS shell and a very high temperature, and is therefore referred to as the hot bubble. Much closer to the star is the wind termination shock which is the shock that slows down the free streaming wind which constitutes the last zone. For a more thorough review regarding a steady stellar wind interacting with a constant density ISM we refer to Weaver et al. (1977).

When all the hydrogen in the core of the star has been converted into helium the star needs another source of energy. The star makes a transition from hydrogen fusion in the core to hydrogen fusion in a shell surrounding the core. Simultaneously it also starts fusing helium into carbon in its core. During this transition from a main sequence star to the next burning phase, the star increases its radius while keeping its luminosity. The temperature at the surface of the star therefore goes down and the star becomes red. The star has become a red supergiant (RSG).

During the RSG phase, the velocity of the stellar wind becomes lower and the mass loss rate increases (compared to the MS mass loss). The material lost during this phase accumulates into another shell which is located at the region where the ram pressure of the current stellar wind is equal to the thermal pressure of the hot bubble. This shell is called the RSG shell. For stars with masses between 8 and roughly 30 $M_{\odot}$, the RSG phase is the final phase during which it will explode (Schaller et al. 1992, Woosley et al. 2002).

For more massive stars the RSG will eventually become a Wolf-Rayet (WR) star. These stars have smaller radii and higher surface temperatures, which causes a high mass loss rate and a high wind velocity. Because the wind during the WR phase is fast, the shell that is created by the WR wind sweeping up the material lost during the RSG phase is very thin. Due to a hydrodynamical instabilities this shell will be unstable and fragment into smaller pieces (García-Segura et al. 1996a). If the WR phase lasts long enough it might even destroy the previously formed RSG shell.

The picture painted above of the evolution of the circumstellar medium (CSM) already shows that the CSM of stars can take on a multitude of forms. The stellar wind can create multiple shells and large cavities, which will strongly influence the supernova ejecta moving through the different regions. Nevertheless, this picture remains a rather simple one. Changes due to the rotation of the star, magnetic fields, binarity or an inhomogeneous ISM can change the stellar wind. In extreme cases the mass loss might behave more like an eruptive event rather than a quiescent wind slowly blowing off material from the surface of the star. In some cases these eruptive events might even be mistaken for supernovae. Supernova 2006jc was seen to have a massive outburst, which was first taken for a supernova explosion, 2 years prior to the supernova actually occurring (Pastorello et al. 2007b).

[1] A transition along which the pressure is constant but the density may change. No flow across this discontinuity occurs.

The mechanism behind the mass loss is not always the same and depends on the specific phase the star is currently in. During the MS and the WR phase the star is hot and the wind mass loss is thought to be driven by radiation pressure from the star. This pressure is exerted on the metal ions which share the momentum they gained from the photons with the more abundant hydrogen and helium in the gas. In phases in which the star is cooler the mass loss can also driven by radiation pressure but this time the pressure is exerted on condensed dust higher in the atmosphere of the star. Small amounts of material at low velocities are moved from the surface of the star to a small distance. At this distance dust can form which is then accelerated by radiation pressure, and drags along the surrounding gas. For a review on mass loss from massive hot stars see Puls et al. (2008). A more general overview, also including mass loss from cooler stars, can be found in Lamers & Cassinelli (1999).

To be able to predict how the interaction of the supernova ejecta with the CSM evolves, it is important to know how the star changed its CSM before it exploded. The presence or absence of certain evolutionary phases can have a significant effect on the details of the CSM structure. Stellar evolution therefore has an important impact on the way the CSM is shaped, and therefore on the interaction of the supernova ejecta with the CSM.

1.3 Supernova explosions

The reason why only stars with masses larger than approximately 8 $M_\odot$ are considered is set by the minimum mass at the start of the MS that is required for single massive stars to undergo carbon burning in the core of the star. Above this boundary there are several mass ranges which differentiate between different kinds of supernova explosions.

Electron Capture Supernovae Stars that are able to burn carbon but are not able to burn neon in their core (which is the subsequent burning phase) can undergo a core collapse. These stars, which prior to the supernova explosion are called super-asymptotic giant branch stars, have an electron degenerate oxygen-neon-magnesium core which grows due to the nuclear burning in a shell around the core. If the core reaches a critical mass of approximately 1.375 $M_\odot$ (Nomoto 1984, 1987) the electrons in the core are captured by the nuclei and the supporting pressure of the core drops. After the collapse of the core a mechanism is needed to accelerate the supernova ejecta outward. The neutrino's emitted by the proto-neutron star are currently thought to be the main driving force behind the expulsion of the supernova ejecta, giving the supernova ejecta a kinetic energy of approximately 10^{50} erg (Kitaura et al. 2006)

Only if the core reaches the critical 1.375 $M_\odot$ can an electron capture supernova occur. Whether or not this happens is determined by the core growth in the center of the star and the mass loss at the surface of the star. If the mass loss rate at the surface is too high, the core growth does not increase the mass of the core fast enough to be able to reach this critical mass and an oxygen-neon-magnesium white dwarf is formed. These two effects are therefore in a race against one another. Poelarends et al. (2008) found that stars with a mass between 7.5 and 9.25 $M_\odot$ can become a super-asymptotic giant branch star and that within this range the stars

between 9 and 9.25 $M_\odot$ are able to explode as electron capture supernovae.

Iron Core Collapse Supernovae When a star is more massive and is therefore able to go through all burning phases including silicon burning, it consists of an iron core surrounded with shells of lighter elements. Since the star is still losing energy due to the emitted radiation, it needs to find a new energy source. As it has done multiple times during its life the stellar core begins to contract to gain energy. Because the binding energy per nucleon is the highest for iron, the star will not be able to find a new energy source by fusing lighter elements into heavier ones, and it thus continues to contract. At a critical point the temperature in the core becomes so high that the iron will disintegrate into lighter elements. This creates a strong energy loss and the core of the star begins to contract even faster to compensate. Unfortunately for the star this means more disintegration and thus more energy loss and thus a faster contraction. The result is a runaway process in which the core collapses and which, through a mechanism that is still not completely understood, finally results in the explosion of the star. The typical kinetic energy of the supernova ejecta connected to this kind of explosion is 10^{51} erg.

The details of the explosion mechanism in this picture of core collapse supernovae is not yet completely understood. What seems clear is that when the densities in the core approach nuclear densities the core collapse halts. The infalling material 'bounces' on the core and an outgoing shock is created. The infalling material is shocked; converting kinetic energy into thermal energy. The thermal energy in this shocked material somehow needs to be transferred back into kinetic energy which will then be seen as the fast moving outward expanding supernova ejecta. Several mechanisms have been proposed to do this (see Janka et al. 2007).

What remains of the star in this scenario depends on the mass of the core of the star. For the most massive cores in the iron core collapse regime the entire core will directly form a black hole. The lightest cores will become neutron stars. In an intermediate region first a neutron star forms, but due to fallback of material onto the neutron star it will collapse into a black hole somewhat later (see Heger et al. 2003).

Pair Instability Supernovae Finally, the most massive stars (above $\gtrsim 140 M_\odot$) (Heger et al. 2003) display another mechanism with which the supernova explosion occurs. Before core oxygen burning, the core of these stars reaches a critical temperature at which it creates electron-positron pairs from photons (Fowler & Hoyle 1964). Since the core is supported by the radiation pressure from these photons, the pressure drops and core collapse starts. Due to explosive burning of the oxygen in the core the collapse is reversed into an explosion. In this scenario the entire star is disrupted. With a predicted energy of approximately 10^{52} ergs, the pair instability supernovae is the most energetic supernova mechanism.

The pair-instability supernovae are perhaps the best understood type of supernovae in terms of the explosion mechanism. How to form these stars and to make sure that they do not lose the majority of their mass in a stellar wind prior to central oxygen burning is the difficulty for this scenario. The above mentioned minimum mass above which these supernovae can occur is dependent on the metallicity of the star. More metals results in a higher mass loss rate. The increase in mass loss rate causes the star to lose a significant portion of its mass and as a result the core of the star will not reach the critical temperature needed to create the electron-

positron pairs. Increasing the metallicity therefore increases the minimum mass above which these supernovae can occur. Since these stars favor regions of low metallicity, they are most likely found in such regions or in the early universe where the metallicity is also low. Recently, pair instability supernovae have received increased attention due to observations of SN2007bi, which is thought to be the first observed pair instability supernova (Gal-Yam et al. 2009, Langer 2009).

1.4 The Interaction of supernovae with their CSM

Regardless of the explosion mechanism, due to the explosion of the star, its outer layers are expelled into the surroundings with high velocities. The supernova ejecta are moving at supersonic speed through the CSM thus creating a forward moving shock. The forward shock of the supernova ejecta (also called the supernova blast wave) shocks and sweeps up the surrounding material. The shocked CSM is heated to millions of degrees and its density is increased. As a result, the pressure just behind the forward shock is also increased strongly. This pressurized region creates another shock, the reverse shock, which will be moving backward into the supernova ejecta (in Lagrangian coordinates), slowing down and heating the supernova ejecta. Between the two shocks is a contact discontinuity which separates the shocked CSM from the shocked supernovae ejecta (see Fig.1.2).

The interaction of the supernova ejecta with its surroundings was classically divided into four important phases (Woltjer 1972). In this picture the density of the CSM was assumed to be constant. During the first phase, the ejecta dominated phase, the supernova ejecta moves outward without being significantly affected by the material in the close surroundings of the star. The amount of material that is being swept up by the supernova ejecta is negligible compared to the amount of material contained within the ejecta.

The second phase, the Sedov-Taylor phase, starts when the total amount of material that is swept up is larger than the mass in the supernova ejecta. Alternatively, one could say that this phase starts when about half of the supernova ejecta is shock heated by the reverse shock. The amount of material shocked by the forward and reverse shock are not independent of one another. The pressure behind the forward shock is proportional to the amount of material that is being shocked. When this pressure is higher, the reverse shock travels faster into the ejecta, and therefore also more material is shocked by the reverse shock.

In the above two phases the energy losses due to radiation do not play a significant role. The supernova ejecta still expand with such a high velocity that the majority of the cooling is a result of the adiabatic cooling of the material. After the supernova remnant has expanded for a long enough time, radiative cooling becomes more and more important. The cooling will initially only influence the swept up CSM. At this point the thermal energy (i.e pressure) of the supernova ejecta is driving the expansion, and therefore this phase is called the pressure driven snow plow phase.

The final phase occurs when the radiative cooling starts decreasing the thermal energy of the supernova ejecta. The driving force behind the expansion is then no longer the thermal pressure of the supernova ejecta, but is now governed by mo-

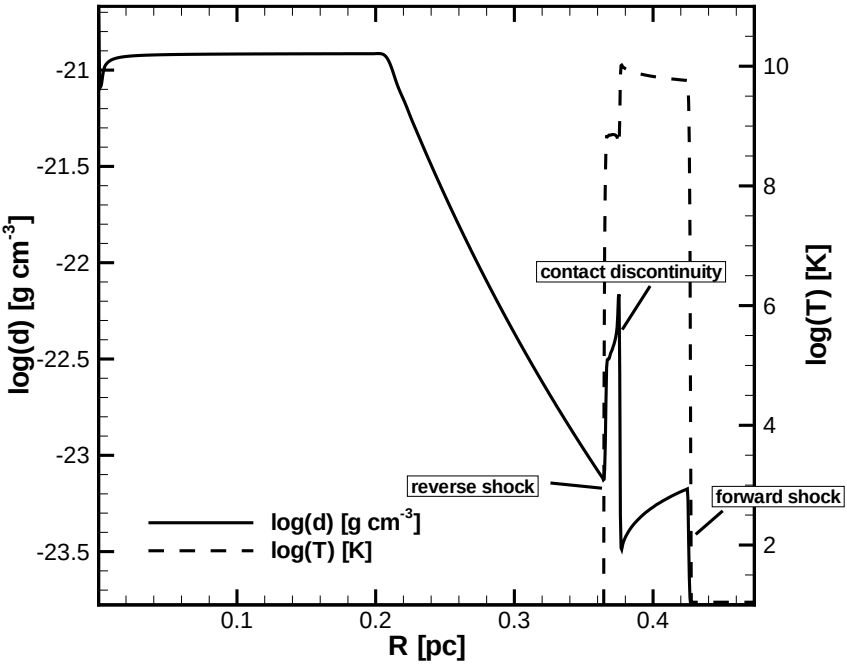

Figure 1.2: Example of density and temperature structure of 1 $M_{\odot}$ of supernova ejecta with an energy of 10^{51} ergs after interacting with a constant density CSM of 1 cm^{-3} for approximately 20 years.

mentum conservation. This final phase is called the momentum driven snowplow phase.

The above description of the evolution of supernova remnants is true as long as the medium into which the supernova ejecta expands does not contain discontinuous changes in density or pressure. When this is not the case, the distinction between the different phases, as described above, is sometimes hard or even impossible to make. If we want to investigate these cases one needs to perform hydrodynamical simulations to be able to predict the evolution of the CSM.

To illustrate that reality is more complicated, consider a forward shock of a supernova encountering a massive shell. At the moment of collision the blast wave shocks a very large amount of material in a very short amount of time. The sudden strong increase in thermal pressure behind the forward shock increases the rate with which supernova ejecta is shocked by the reverse shock. Since the overall amount of material that is shocked increases dramatically, the amount of light emitted from that material is increased. A sudden re-brightening of the supernova can occur. A clear example of this is SN1987A. After approximately 13 years the ring surrounding the supernova lit up due to the collision of the supernova ejecta with the

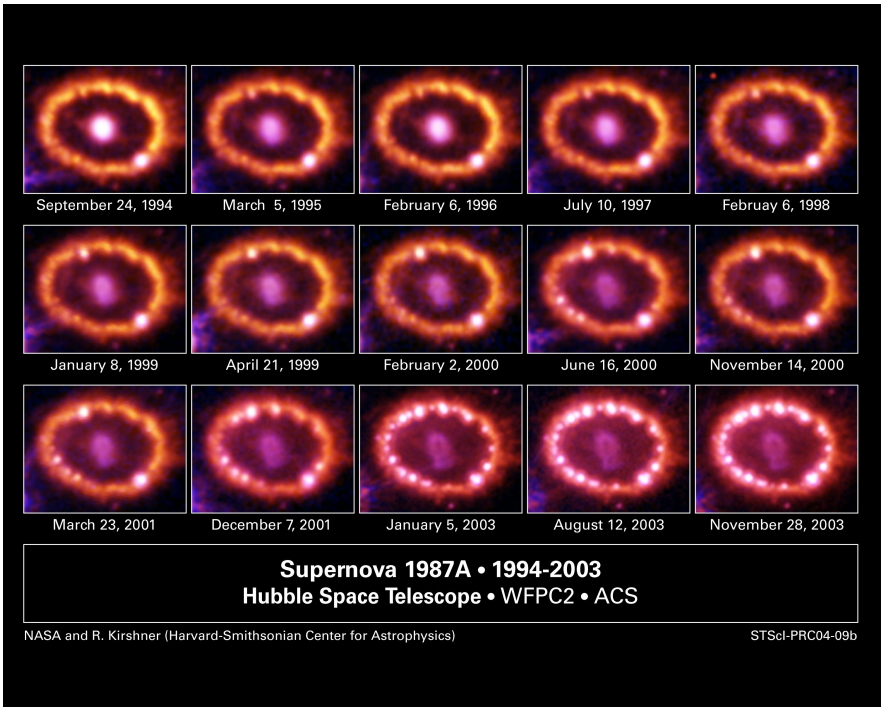

Figure 1.3: A set of images of the region in which SN1987A exploded. The ring of material, which was formed prior to the supernova explosion, starts to re-brighten after approximately 13 years due to the collision with the supernova ejecta.

pre-existing dense ring (Fig. 1.3).

1.5 This Thesis

By looking at the interaction of supernova ejecta with the CSM we hope to learn more about the evolution, stellar winds and supernova explosions of massive stars, since they play an important role in our universe. They are one of the primary sources of chemical enrichment of the universe, by ejecting material either through their stellar wind or the supernova explosion. They are also an important source of energy and momentum for the ISM.

In this thesis we aim to look at the complete picture of the interaction of supernova ejecta with the CSM. During the time shortly after the supernova explosion (time < several years) a comparison with supernova observations can be made. We also look at much longer time scales (time > hundreds of years) during which we can investigate supernova remnants. While these two extremes are the most obvious choices, the time in between should not neglected since the effects of the CSM on the evolution occur at all times.

Chevalier (1982) already showed that there are analytical solutions if simplifying assumption regarding the structure of the CSM and the structure of the super-

nova ejecta are made. While the importance of the CSM structure was already recognized at that point, hydrodynamical investigations including both stellar evolution models, to look at the pre-supernova evolution of the structure of the CSM, and the interaction of the supernova ejecta with the evolved CSM are scarce (Dwarkadas 2005, Schure et al. 2008).

Only in simplified situations can analytical solutions for the evolution of the CSM be found. This holds for both the evolution of the CSM under the influence of stellar winds and the explosion of supernovae. To be able to investigate the interaction of the supernova ejecta with the CSM we use a 3D hydrodynamics code called ZEUS MP (Hayes et al. 2006) in this thesis. By performing multi-dimensional simulations we allow hydrodynamical instabilities to occur. If we were to perform one-dimensional simulations such instabilities could not occur which in some cases would dramatically alter the results.

The layout of this thesis is as follows:

Chapter 2: The hydrodynamics of the supernova remnant Cassiopeia A: The influence of the progenitor evolution on the velocity structure and clumping

In this chapter we will discuss the young supernova remnant Cassiopeia A. We investigate the CSM evolution of a 20 $M_{\odot}$ star which may have had a WR phase. If the star goes through this WR phase a clumpy shell in the CSM will occur. This shell has a strong influence on the final state of the supernova remnant. Observations show the presence of clumps in the supernova remnant, which may have originated from the clumpy WR shell. By comparing the results of our calculations with the observed properties of the supernova remnant we found that the remainders of the clumps in our models did not match the observed clumps in the supernova remnant. This suggests that the progenitor star of Cas A did not have a WR phase. Also, the shock structure was best modelled by assuming that the star did not go through a WR phase.

Chapter 3: The Destruction of Cosmological Minihalos by Primordial Supernovae

Here we will discuss the effects of the very first supernovae. The first stars in the universe are born in massive halos which can become ionized due to the radiation coming from the surface of the star. By looking at different masses for the stars and the halos we investigate the survival or destruction of the halo by the supernova explosion. We find that when the halo is ionized the star will sweep up the material in the central regions of the halo. The subsequent supernova explosion will therefore first expand adiabatically and start radiating strongly when it interacts with the swept up material. Supernova explosions within neutral halos start radiating promptly but can retain enough energy and momentum to disrupt the halo. The least energetic of the supernovae, connected to the stars that are least massive at birth, are capable of destroying halos $\lesssim 10^7\ M_{\odot}$. This disruption is important with respect to the distribution of the very first heavy metals coming from these supernovae. These metals are essential in the formation and evolution of the second generation stars.

Chapter 4: The Circumstellar Interaction of electron capture Supernovae

Electron capture supernovae constitute a specific class of sub-energetic supernovae at the lower end of the allowed mass range for stars that explode. During the super-AGB phase of the progenitor star of these supernovae they have an enhanced mass loss rate. In this chapter we investigate the evolution of the circumstellar medium of these stars, followed by the interaction of the supernova ejecta with the circumstellar medium. We find that, although the supernova explosion might be sub-energetic, the amount of light we see from these supernovae is on par with supernovae formed through iron core collapse. This is a result of the high amount of mass close to the star when it explodes. The supernova ejecta collide with this material at a very early stage and the collision causes the high amount of energy lost through radiation. We provide a simple fitting formula, which predicts the expected amount of light as a function of the supernova ejecta mass and the density structure of the circumstellar medium. Finally, we have also compared our results with the observations and found that several supernovae exhibit properties similar to our model predictions.

Chapter 5: Pulsating Red Supergiants as possible progenitors of type IIn supernovae

During the Red Supergiant phase a star undergoes a phase in which the pulsations that occur in the envelope may become strong enough to drive an increasingly stronger stellar wind. We investigate the evolution of the CSM of such a star and the following interaction of the CSM with the supernova ejecta. We specifically look at the possibility of these stars to create the conditions for type IIn supernovae. These type of observed supernovae have a narrow Hα emission line in their spectrum which originates from the circumstellar medium. The fact that this emission line is narrow tells us that it must originate from the *undisturbed* circumstellar medium, and it therefore tells us something about the pre-supernova mass loss of the star. We investigate three different progenitor models, which have different time spans between the peak of the pulsationally enhanced mass loss and the supernova explosion. We find that when the supernova explodes during the peak mass loss rate or shortly afterwards (4 000 yr) it is possible to observe such a narrow Hα emission line.

Chapter 2

The hydrodynamics of the supernova remnant Cassiopeia A

The influence of the progenitor evolution on the velocity structure and clumping.

B. van Veelen, N. Langer, J. Vink, G. García-Segura and A.J. van Marle
based on *Astronomy & Astrophysics 2009; 503* (p. 495-503)

There are large differences in the proposed progenitor models for the Cas A SNR. One of these differences is the presence or absence of a Wolf-Rayet (WR) phase of the progenitor star. The mass loss history of the progenitor star strongly affects the shape of the Supernova remnant (SNR). In this paper we investigate whether the progenitor star of Cas A had a WR phase or not and how long it may have lasted. We performed two-dimensional multi-species hydrodynamical simulations of the CSM around the progenitor star for several WR life times, each followed by the interaction of the supernova ejecta with the CSM. We then looked at the influence of the length of the WR phase and compared the results of the simulations with the observations of Cas A. The difference in the structure of the CSM, for models with different WR life times, has a strong impact on the resulting SNR. With an increasing WR life time the reverse shock velocity of the SNR decreases and the range of observed velocities in the shocked material increases. Furthermore, if a WR phase occurs, the remainders of the WR shell will be visible in the resulting SNR. Comparing our results with the observations suggests that the progenitor star of Cas A did not have a WR phase. We also find that the quasi-stationary flocculi (QSF) in Cas A are not consistent with the clumps from a WR shell that have been shocked and accelerated by the interaction with the SN ejecta. We can also conclude that for a SN explosion taking place in a CSM that is shaped by the wind during a short ($\leq$ 15000 yr) WR phase, the clumps from the WR shell will be visible inside the SNR.

2.1 Introduction

One of the challenges of supernova remnant (SNR) research is to link the properties of the remnant with the properties and the evolution of the progenitor star. Ideally one would hope to learn about the late stages of stellar evolution from the properties of the SNR. In that respect one of the best-studied SNRs is the bright Galactic remnant Cas A.

For a long time Cas A has been thought to be the remnant of a very massive star, possibly that of an exploding Wolf-Rayet (WR) star (e.g. Fesen et al. 1987, Woosley et al. 1993, Borkowski et al. 1996). In that case one would expect the supernova to be of Type Ib/c. However, recently Krause et al. (2008) obtained a spectrum of the supernova by observing its light echo, identifying it as a Type IIb explosion. This indicates that the progenitor lost most, but not all of its hydrogen envelope.

X-ray observations indicate that the ejecta mass was only 2 - 4 $M_{\odot}$ with about 1 - 2 $M_{\odot}$ of oxygen (Vink et al. 1996, Willingale et al. 2003). The latter suggests an initial mass for the progenitor of approximately 20 $M_{\odot}$, which is close to the lower limit of the mass of a star at the start of the main sequence (MS) in the Galaxy that can become WR stars (Meynet & Maeder 2005, Massey et al. 2000). However, it is not clear whether the low ejecta mass is due to heavy mass loss of a single massive star that was on its way, or just entered the WR phase, or whether mass loss was induced by a common envelope phase in a binary system (Young et al. 2006). Also the presence of a jet-counter-jet system in Cas A (Vink 2004, Hwang et al. 2004) puts strong constraints on the duration of a possible WR phase (Schure et al. 2008). Furthermore, the high density of the shocked circumstellar material (CSM) indicates that the shock wave is currently moving through the red super giant (RSG) wind of the progenitor (Chevalier & Oishi 2003).

Although recent studies (Schure et al. 2008, Krause et al. 2008) seem to suggest an extended progenitor star, the presence of a WR shell, i.e. the shell of red supergiant (RSG) wind material swept up by the fast WR wind, has been invoked to explain the presence of numerous slow moving ($\leq$ 500 km/s van den Bergh & Kamper 1985) nitrogen rich knots, often called quasi-stationary flocculi (QSF). García-Segura et al. (1996a) suggested that these knots are the remnants of the broken up WR shell. Note that also a binary common envelope phase is likely to be followed by a WR-like mass loss phase (Young et al. 2006). Both the fact that the QSF lie within the boundary of the forward shock, and the inferred density behind the forward shock of Cas A, limits the possible duration of a WR phase to $\sim 10^4$ yr (García-Segura et al. 1996a).

Here we report on our investigation of the imprint of the progenitor's stellar wind evolution, i.e. the existence and duration of a WR phase, on the morphology and kinematics of Cas A. For the first time we study the hydrodynamical evolution of a SNR in 2-D using multi-species advection, which allows us to separate the location and kinematics of wind material from the supernova ejecta.

Table 2.1: Adopted progenitor star wind parameters for our Cas A hydrodynamic simulations: final evolutionary phase of the progenitor star, duration of this phase, corresponding mass loss rate and wind velocity, total amount of mass and kinetic energy lost during this phase, and model acronym.

	τ[yr]	$\dot{M}[M_\odot\ \mathrm{yr}^{-1}]$	v[km s^{-1}]	$\Delta M[M_\odot]$	$\Delta E[10^{45}$ erg]	Model
Red Supergiant	$8.75 \cdot 10^5$	$1.54 \cdot 10^{-5}$	4.70	13.5	5.93	WR0
Wolf Rayet	$5 \cdot 10^3$	$9.72 \cdot 10^{-6}$	$1.716 \cdot 10^3$	0.05	$1.42 \cdot 10^3$	WR5
Wolf Rayet	$10 \cdot 10^3$	$9.72 \cdot 10^{-6}$	$1.716 \cdot 10^3$	0.10	$2.85 \cdot 10^3$	WR10
Wolf Rayet	$15 \cdot 10^3$	$9.72 \cdot 10^{-6}$	$1.716 \cdot 10^3$	0.15	$4.27 \cdot 10^3$	WR15

2.2 Method and Assumptions

2.2.1 The adopted stellar evolution model

As discussed in Section 2.1, the progenitor star of Cas A has evolved through a RSG phase and perhaps a WR phase before exploding. This evolutionary history gives us constraints on the mass of the progenitor. Unfortunately, the allowed mass range of stars that have a WR phase during their evolution is not very well known. Meynet & Maeder (2005) show that stars with an initial mass as low as 20 $M_\odot$may end up as a WR star, and that those stars will have a short WR life time. Alternatively, the progenitor of Cas A may have gone through a binary common envelope phase. However, we treat here the evolution of the progenitor as that of a single massive star. The reason for that is partly practical; there are no good analytical models of the hydrodynamics of a common envelope phase, and a full numerical simulation of this is beyond the scope of this study. Moreover, one may expect that a common envelope phase results in a non-spherically symmetric outflow. Although there is evidence for non-sphericity of the supernova ejecta in Cas A (e.g. Willingale et al. 2002), the outer shock wave is surprisingly circular (Vink 2004), suggesting a more or less spherically symmetric CSM. The CSM structure that we assume, i.e. one that is shaped by a spherically symmetric wind of a single massive star, seems valid for Cas A.

We have chosen an initial mass for the progenitor star of 20 $M_\odot$, in accordance with previously suggested ZAMS masses (Vink 2004). The stellar evolution model of this 20 $M_\odot$, non-rotating star was calculated by Hirschi et al. (2004). In this model the star does not have a WR phase and we thus assumed an enhanced RSG mass loss in such a way that during the RSG phase the entire hydrogen envelope is lost. It does not matter for the evolution of the core if the star loses its envelope entirely or only partly in this case, which means that we can assume the enhanced mass loss without affecting other parameters of the stellar evolution model. An enhanced mass loss rate is not unreasonable given by the uncertainty there currently is in RSG mass loss rates (see de Jager et al. 1988, van Loon et al. 2005, and discussion therein).

The core mass at the end of the RSG phase is 6 $M_\odot$which is also the final mass of the progenitor, due to our assumed enhanced mass loss rate. This mass is also roughly consistent with the ejecta mass of Cas A of about 2 - 4 $M_\odot$, taking the presence of the neutron star in Cas A into account(Tananbaum 1999, Chakrabarty

et al. 2001). We adopt an ejecta mass of 4 $M_\odot$, and an ejecta kinetic energy of $2 \cdot 10^{51}$ erg (Vink 2004).

The mass loss rate and velocity of the stellar wind are calculated by combining the observational constraints and the parameters of the stellar evolution model. We can derive the total mass lost during the RSG phase by comparing the mass at the end of the MS phase, 19.5 $M_\odot$, with the final mass of the progenitor, 6 $M_\odot$. This gives a total mass loss of 13.5 $M_\odot$. The RSG life time is $8.75 \cdot 10^5$ years which implies a mass loss rate of $1.54 \cdot 10^{-5}$ $M_\odot$ yr^{-1}. Since we assume that all the mass is lost during the RSG phase, we also have to assume that during the short duration WR phase the total amount of mass lost to the CSM does not increase significantly (see Table 2.1).

The radii of the forward and reverse shock of Cas A are $2\farcm55 \pm 0\farcm2$ and $1\farcm58 \pm 0\farcm16$ (Gotthelf et al. 2001), which at a distance of $3.4^{+0.3}_{-0.1}$ kpc (Reed et al. 1995), correspond to 2.52 ± 0.2 pc and 1.58 ± 0.16 pc respectively. Since the amount of mass within the radius of the forward shock has to be ~ 8 $M_\odot$(Vink et al. 1996), we can determine the RSG terminal wind velocity by using the following relation between the mass loss rate, wind velocity and forward shock radius:

$$8M_\odot = \int 4\pi r^2 \rho(r) \mathrm{d}r = \int 4\pi r^2 \frac{\dot{M}}{4\pi r^2 v_w} \mathrm{d}r = \frac{\dot{M} \cdot 2.52 \text{ pc}}{v_w} , \tag{2.1}$$

in which we assume that the mass loss rate and the velocity are constant, and that the density is consistent with a r^{-2} profile shaped by the free streaming RSG wind.

When we assume that the density profile, within the current forward shock radius, at the end of the RSG phase is consistent with an r^{-2} profile shaped by the free streaming RSG wind, we have to check if the RSG shell is well outside the current shock radius.[1] For this purpose we used equation (22) from Weaver et al. (1977), which gives the pressure inside the MS hot bubble, and the equation for the ram pressure of a stellar wind $P_{ram} = \rho v^2$. Using the parameters for the MS phase of the stellar wind given in Hirschi et al. (2004), a typical MS wind velocity of 1000 km s^{-1}, a ISM density of 10^{-23} g cm^{-3} and the parameters for the RSG wind given in Table 2.1, we obtain a radius for the RSG shell of approximately 4 pc.

Because in our simulations we only consider the inner 3 pc of the CSM and the RSG shell is located at approximately 4 pc, the assumption of an initial r^{-2} density profile at the end of the RSG phase for the inner 3 pc is justified. Since the structure of the CSM at the end of the RSG phase can be determined with the above mentioned assumptions, it was not necessary to perform a hydrodynamical simulation of the CSM during the RSG phase, which saved considerable computing time.

The values for the WR mass loss rate and wind velocity are calculated with help of the equations (12), (15), (17) and (22) from Nugis & Lamers (2000). The parameters needed for the calculation of the mass loss rate and velocity of the WR wind are taken from the stellar model of Hirschi et al. (2004). All the values for stellar wind are summarized in Table 2.1. Since we do not know the WR life time, or whether there was a WR phase, we treat the WR life time as a free parameter.

[1] This shell is created by the outflowing RSG wind and a hot MS bubble pushing inward.

2.2.2 Numerical method

All the simulations presented here are done with the ZEUS MP code (Hayes et al. 2006). This is a three dimensional Newtonian magneto-hydrodynamics code, which solves the Euler equations on a staggered mesh grid. Magnetism and gravity can also be treated by the code, but are not used here.

In order to separate the CSM from the SN ejecta we use the multi-species advection available in ZEUS MP by considering two 'species', corresponding to the above mentioned components. The real composition of each of these species is not of importance since no feedback effects from the species back into the hydrodynamic calculations are taken into account.

Radiative cooling is included using the cooling curve from MacDonald & Bailey (1981), which is valid for a gas of approximately solar composition, but is applied to all the gas in the simulations. Applying this cooling curve to the gas consisting of CSM material is reasonable since it has a composition comparable to the solar composition. Applying it to the gas consisting mainly of SN ejecta material is not correct. However, the most important cooling in these regions is adiabatic cooling due to the expansion of the SN ejecta, and thus the error we make in this respect is small. By calculating how much energy we lose and assuming that all the gas is optically thin, we can use the cooling curve to estimate the radiative energy loss from these simulations.

Our simulations were done in two stages, the first stage was that of the interaction of the stellar wind with the CSM, which we calculated only once, and the second stage concerned the SNR evolution. Simulating the stellar wind was done in the same manner as described in García-Segura et al. (1996a). In this method the innermost radial grid cells are given a density and velocity corresponding to the stellar wind at that point in time. This is done each time step to simulate the star blowing out its stellar wind. We simulated the evolution of the CSM due to the stellar wind only once, but used the output of the calculation at different evolutionary phases as input for stage 2, the collision of the supernova ejecta with the CSM.

Simulating the supernova explosion was done in the same manner as described in Whalen et al. (2008). This method uses the following assumption for the radial density and velocity profile of the supernova ejecta, which at a given time has a flat inner core and a steeply declining outer edge:

$$\rho(v,t) = \begin{cases} F \cdot t^{-3} & \text{for} \quad v \le v_{core} \\ F \cdot t^{-3} \cdot (\frac{v}{v_{core}})^{-n} & \text{for} \quad v_{core} < v \le v_{max} \\ \rho_{CSM} & \text{for} \quad v > v_{max} \end{cases} , \tag{2.2}$$

$$v(r,t) = \frac{r}{t} \quad \text{for} \quad t > 0 \, . \tag{2.3}$$

Here ρ is the density, t is the time, v is the velocity and r is the radius. F and v_{core} are normalization constants which are determined through the assumed SN explosion energy and ejecta mass. The maximum velocity (v_{max}) is set to $3 \cdot 10^4$ km/s, which roughly corresponds to the maximum observed velocity in core collapse supernovae. The supernova explosion energy is assumed to be kinetic. The supernova ejecta are assumed to be spherically symmetric, so no clumps are present in the ejecta. The value for the exponent n is set to 9 for all simulations, which is usually assumed for core collapse supernovae (Truelove & McKee 1999, Dwarkadas

2005, Chugai & Chevalier 2006). We calculated four different SNR scenarios, corresponding to an explosion inside a CSM shaped only by the RSG wind (model WR0), and three explosions inside a CSM shaped by the WR star wind, with WR life times of 5000 yr (WR5), 10000 yr (WR10), and 15000 yr (WR15).

For all the results shown, a spherical coordinate system was used (r,θ,φ), with an assumed symmetry in the φ-direction. The number of grid cell in the radial direction was always equal to 1000. The physical size, in the radial direction, of the grid in the pre-supernova evolution simulations was ranging from 0 to 3 pc, and the grid cells were equally spaced over this range.

In the case of the supernova calculations the physical size of the radial grid was enlarged each time step, which is also done in the same manner as described in Whalen et al. (2008). For each time step the total number of grid cells was redivided over the grid, which resulted in an equally spaced grid for the radial direction at every time. The number of angular grid points, in the φ direction, was equal to 200 for all simulations. The angular grid ranged from 0 to $\frac{\pi}{4}$ over which the number of grid cells were equally spaced.

Finally, we do not intend to match the observational properties of Cas A to the last detail. This would require considerable fine tuning. For example, if we want to match our forward shock radius to the observations we could change both the SN explosion energy or the SN explosion mass which both affect the shock radius. We are more interested in looking at the influence of the presence or absence of a WR phase, and its duration, on the resulting SNR.

2.3 Results

We have performed only one simulation for the evolution of the CSM prior to the supernova explosion. We take the output of this simulation at different times and use these different outputs as an input for the simulations of the SN ejecta interacting with the CSM.

2.3.1 Pre-Supernova Evolution

Figure 2.1 shows four snapshots of the CSM density structure approximately 5000, 10000, 15000, and 19000 years after the start of the WR phase. The figure shows a stable WR shell is not formed: rather a fragmented shell forms in which there are several small and larger clumps with a higher density than the density in the free streaming RSG wind. This clumping is due to the Vishniac/thin shell instability (Vishniac 1983, Mac Low & Norman 1993, García-Segura & Mac Low 1995).

The clumping of the WR shell and its evolution affect the interaction of the supernova ejecta with the shell. We illustrate this in Fig. 2.2 which shows the cumulative amount of mass for one angular grid cell and along all radial cells for the different angles of the three models with a WR phase. The relative difference between the amount of mass at angles where there is a clump compared to the angles where there is no clump becomes larger when the WR phase lasts longer. This implies that the clump masses grow with time. As a result of the clumping the supernova ejecta will be able to pass the WR shell easier at certain angles, which will affect the shock structure of the resulting SNR. When the WR phase

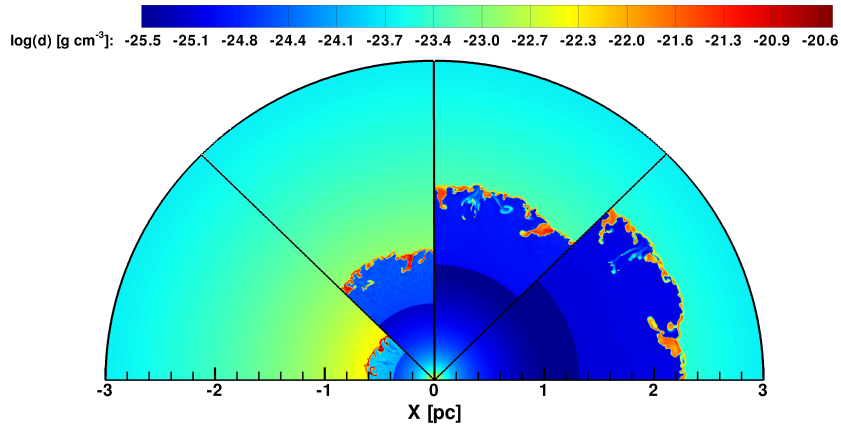

Figure 2.1: From left to right the figure shows the CSM density structure approximately 5000, 10000, 15000 and 19000 years after the start of the WR phase. Looking from the first to the last slice (clockwise) the outward moving WR shell can be seen. This shell is unstable and will form clumps due to the Vishniac instability. Outside the WR shell the CSM structure is shaped by the wind of the previous RSG phase.

lasts longer the clumps in the WR shell will be harder to destroy and to accelerate by the SN blast wave.

2.3.2 Supernova Remnants

SNR structure

Figure 2.3 shows CSM and SN ejecta density structure of the resulting SNR for our models WR0 (first slice) and WR15 (second slice) 335 years after the supernova explosion. This corresponds approximately to the age of Cas A assuming an explosion date of 1671 ± 0.9 (Thorstensen et al. 2001). In both slices the forward and reverse shock appear as a discontinuous jump in the density. The contact discontinuity (CD), which marks the boundary between the shocked SN ejecta and shocked CSM, can no longer be seen in the second slice, due to the collision of the SN ejecta with an irregularly shaped WR shell. In the first slice the fingers of the Rayleigh-Taylor instabilities at the CD show the mixing of the SN ejecta with the CSM. This instability is caused by the high density shocked SN ejecta being decelerated by the low density shocked CSM.

The most important difference between these two models is the different structure and corresponding density contrast within the SNR. Because the supernova ejecta encountered a smooth, spherically symmetric CSM in WR0 the only non-spherical component is the one caused by the Rayleigh-Taylor instability at the CD. The large density contrasts within the second slice of Fig. 2.3 are caused by the supernova ejecta colliding with a clumpy WR shell, instead of a smooth CSM. The high density clumps in the WR shell of the progenitor are not completely destroyed by the supernova ejecta and can still be seen as high density clumps within the SNR. Since they contain a lot of mass compared to their surroundings they are

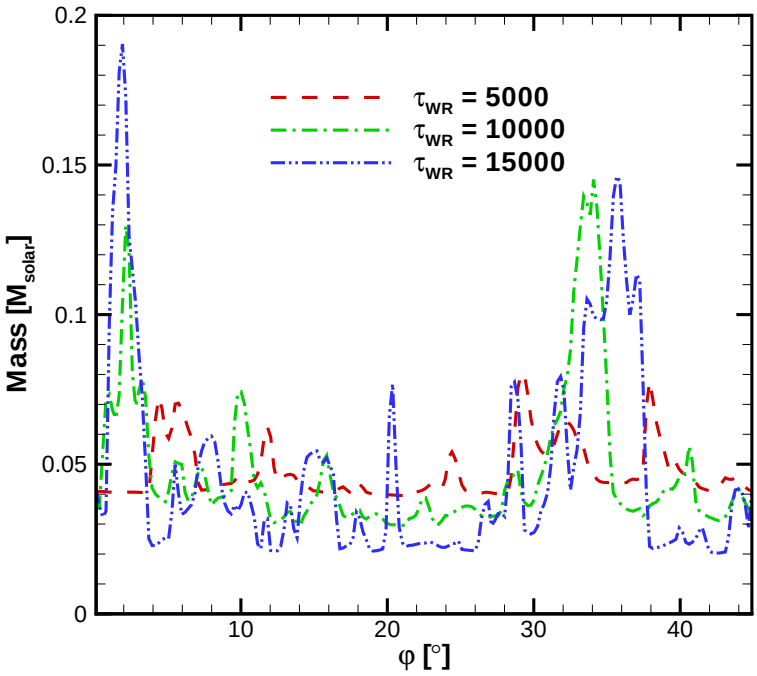

Figure 2.2: Cumulative amount of mass in one angular grid cell and along all radial cells, from 0 to 3 pc, plotted against angle for Model WR5, WR10 and WR15. The zero degree angle corresponds to the left border of the slices of Fig. 2.1, with the 3 models corresponding to the first 3 slices. When the WR phase lasts longer with each model, the contrast of the total amount of mass at different angles also becomes larger. The peaks in the curves correspond to the angles at which clumps are located in the WR shell.

hard to accelerate and the supernova ejecta moved around them. This is reflected in the structure of the shocks, which is somewhat different for angles where there is a clump compared to the the angles where there is no clump.

The distribution of CS mass with respect to the density and velocity can be seen in Fig. 2.4. These figures are mass histograms showing the amount of circumstellar mass in a bin corresponding to a specific range in velocity and density. They were made by adding the mass of every grid cell which had a CSM composition in excess of 70%, placing it in the corresponding bin in velocity and density. In the upper left mass histogram of Fig. 2.4 there are two regions with a considerable amount of CS mass. The first is the unshocked CSM which can be seen as the peak at low density and zero velocity. The second is the shocked CSM with a velocity exceeding 3500 km $s^{-1}$and a density of approximately $10^{-22.8}$ g cm^{-3}. All the other mass histograms still show the unshocked CSM as a high peak in mass at zero velocity and low density, but the shocked material is spread out over a much larger range in velocities, due to the violent interaction with the WR shell. It can also

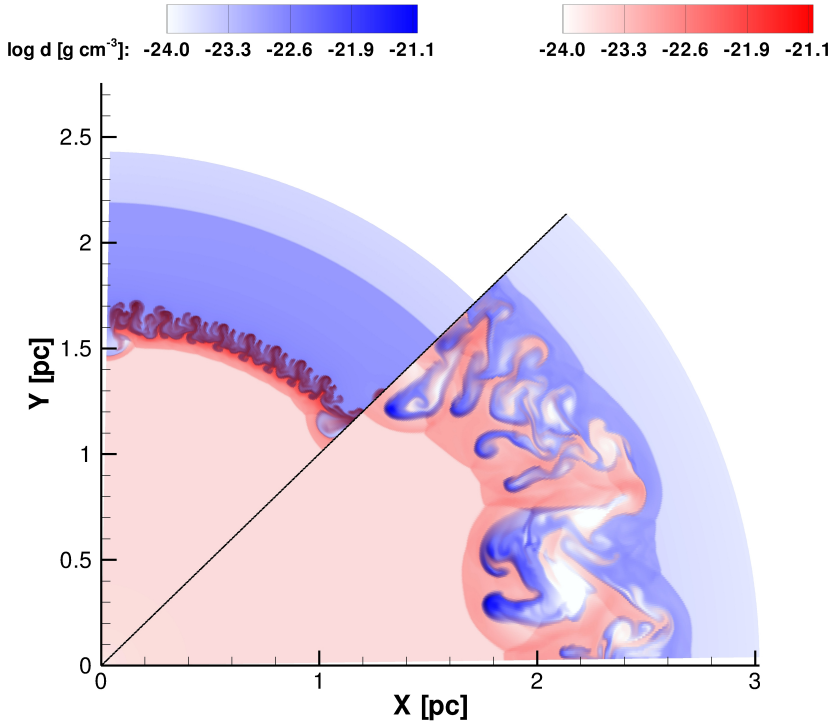

Figure 2.3: CSM (blue) and SN ejecta (red) density structure of the SNR of Models WR0 (first slice counting clockwise) and WR15 (second slice), 335 years after the supernova explosion. The blue color corresponds to the circumstellar material and red to the supernova ejecta. In regions where both material originating from the SN ejecta and from the CSM are present, the colors are added and will thus become purple.

be seen that the range of velocities seen in the shocked CSM becomes larger with increasing WR life time. This is due to the increasing amount of mass within the WR shell for a longer WR life time. Another apparent component in the lower two histograms is the slow moving, highest density material which corresponds to the high density clumps in the remnant. Model WR5 does not show this feature but the remainders of the WR shell remain visible even in that model, as we will discuss below.

Figure 2.5 shows the mass histograms for the SN ejecta for all models. The unshocked, freely expanding ejecta are visible as a horizontal line in the histograms. Similar to what was seen in the shocked CSM distribution, the shocked SN ejecta of Model WR0 span a much smaller range in velocities compared to the shocked SN ejecta of the models with a WR phase. Also similar is that the range of velocities seen in the shocked SN ejecta increases with a longer WR life time.

Figure 2.6 shows the radiative energy loss of Models WR0 and WR15 corresponding to the density plots in Fig. 2.3. In the figure, only the material between the forward and reverse shock is visible. The material outside this region does not

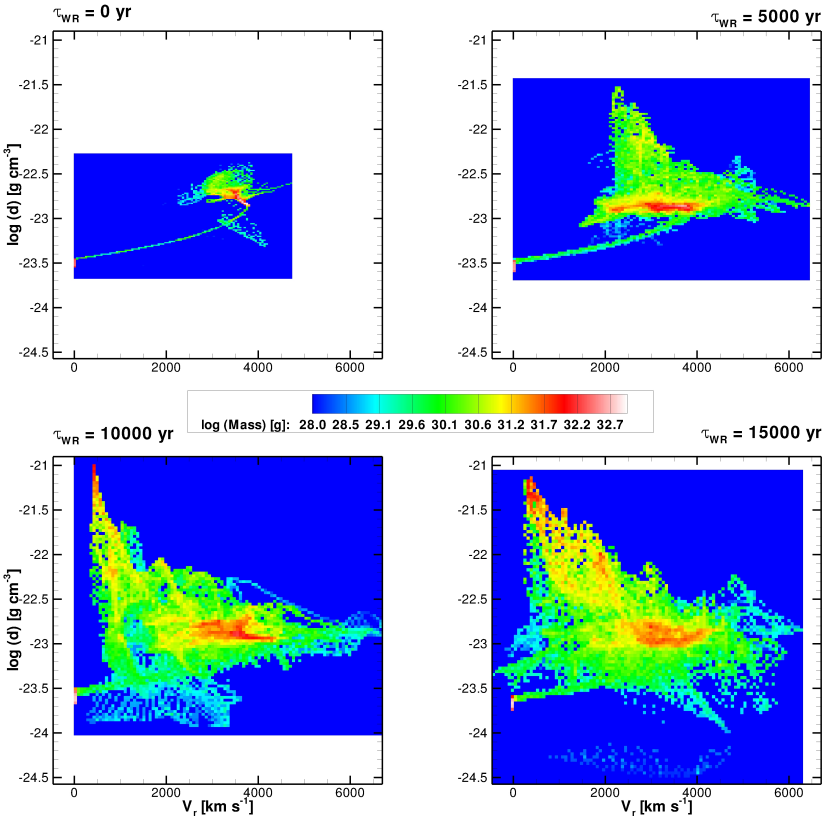

Figure 2.4: Circumstellar mass histogram of Model WR0 (top left), WR5 (top right), WR10 (bottom left) and WR15 (bottom right), which shows the amount of circumstellar mass in a bin corresponding to a certain range in velocity and density. In all figures the high amount of mass at low density and low velocity represents the unshocked CSM. In the upper figures the curved line is an artifact from the artificial viscosity, which smears out the forward shock over several radial grid cells. For better comparison we have kept the color coding and the axis ranges the same for all subfigures.

have a high enough temperature to emit enough radiation compared to the other components. In the first slice the Rayleigh-Taylor instabilities dominate, while in the second slice the high density clumps are most apparent. WR0 also shows that the RT instabilities are composed of both circumstellar material and SN ejecta. In the second slice the clumps are by far the most visible feature in the SNR, brighter by more than 2 orders of magnitude when compared to other material in the SNR. Although we believe that the qualitative result of the radiative energy loss is valid, one has to be cautious when looking at the results qualitatively. For instance, non equilibrium ionization and higher metal composition would increase line emission and are thus expected to increase the cooling rates.

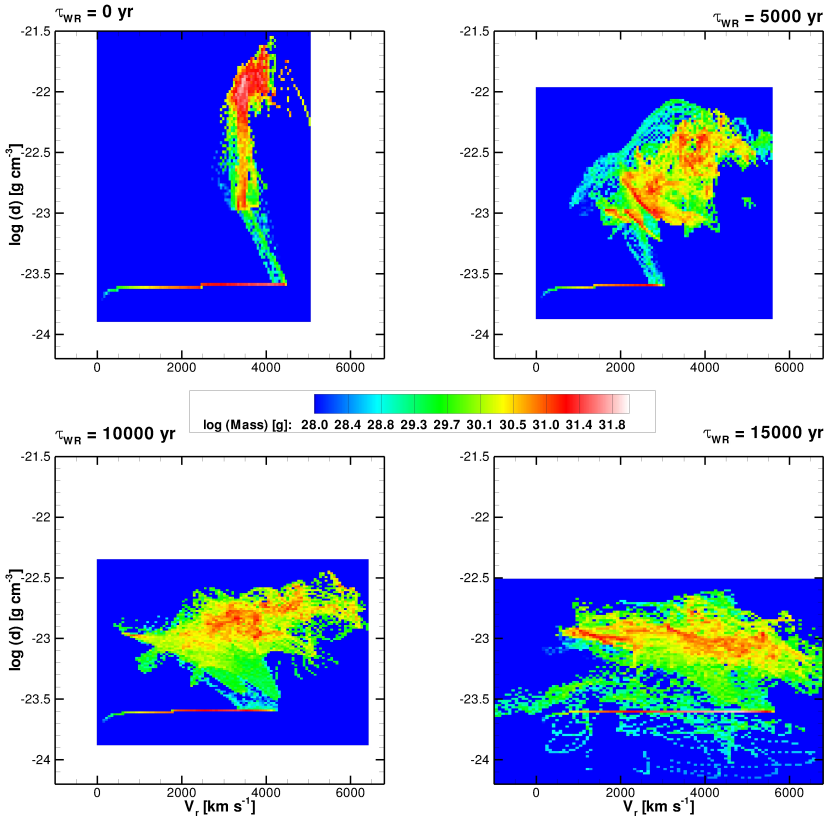

Figure 2.5: Supernova ejecta mass histograms of Model WR0 (top left), WR5 (top right), WR10 (bottom left) and WR15 (bottom right), similar to Figure 2.4. The freely expanding ejecta can be seen as the horizontal line in all histograms. The rest of the mass in the histograms represents the shocked ejecta.

Shock structure and kinematics

Figures 2.7 to 2.10 show the angle-averaged values of the radius of the forward shock, the radius of the reverse shock, the velocity of the forward shock, the velocity of the reverse shock and the observed values. The radii of the forward and reverse shock were mentioned in Section 2.2.1, the velocity of the forward shock is 4990 ± 150 km s^{-1}(Vink et al. 1998, DeLaney et al. 2004, Patnaude & Fesen 2008) and the velocity of the reverse shock is approximately 2000 ± 400 km s^{-1}(Morse et al. 2004). The value of the reverse shock velocity that is mentioned in the latter paper is actually 3000 km s^{-1}. However, that is measured in the frame of the unshocked ejecta, whereas we are considering the velocity of the reverse shock in the observers frame, and should thus use 2000 km s^{-1}, which also comes from that paper.

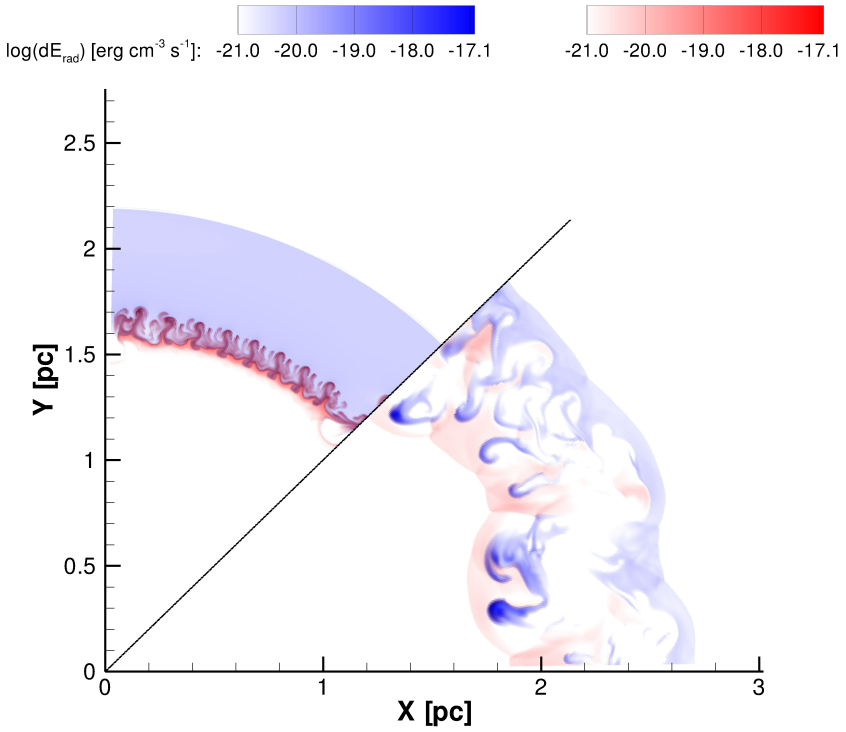

Figure 2.6: Radiative energy loss of the CSM (blue) and SN ejecta (red) components of the SNR Models WR0 (first slice) and WR15 (second slice), 335 years after the supernova explosion. The energy loss is calculated by using the MacDonald & Bailey (1981) cooling curve. The second slice clearly shows that due to the clumped structure of the WR shell the majority of radiating material consists of shocked CSM. The fingers due to the Rayleigh-Taylor instability in the first slice show emission from both shocked CSM and shocked ejecta.

In Fig. 2.7 it can be seen that for a given explosion energy and age of Cas A, the longer the WR phase lasts, the larger is the radius of the forward shock. As the WR phase lasts longer, the low density region blown by the WR wind becomes larger, which enables the supernova ejecta to expand freely over a longer period which increases the forward shock radius. Although the measurement does not agree with the result of all models, the differences are small compared to the differences in the results for the reverse shock which we discuss below. A small change in the model parameters, or a difference due to the uncertainties within the models themselves, could already change the results such that all models could agree with the observations. The reason for the small variations in shock radius is that all models have roughly the same amount of swept up CSM. At the current age of Cas A the forward shock velocities of all four models are also very similar to one another (Fig. 2.8), and lie within 10% of each other.

The comparison of the results for the reverse shock radius (Fig. 2.9) and the observations tell us more, since there is a clear difference between the models. For

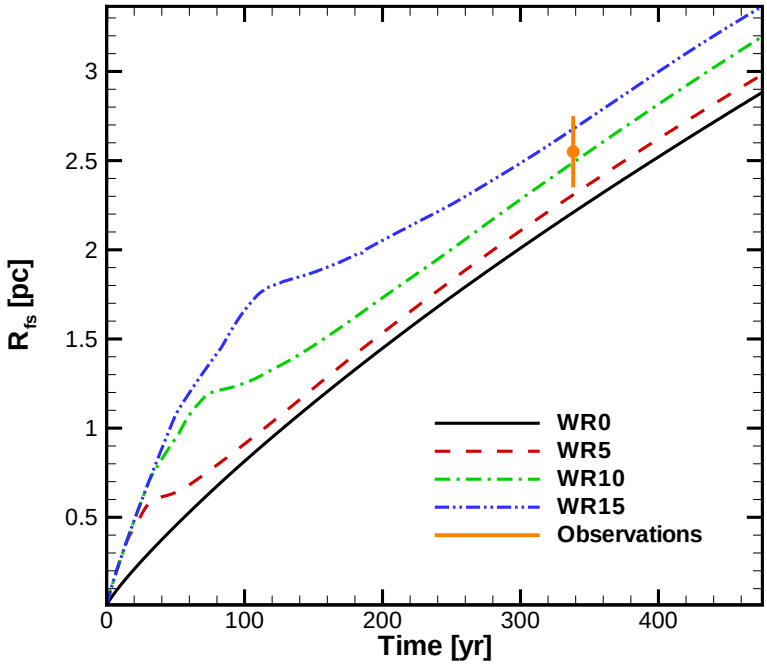

Figure 2.7: Angle averaged radius of the forward shock, for the different models, plotted against time. The orange dot shows the observational value for the forward shock radius at the age of Cas A and the line shows the observational uncertainty in radius. The uncertainty in the age is too small to be visible in this figure. After the initial free expansion phase, the models with a WR phase collide with the WR shell at a different time and the expansion of the forward shock slows down.

the models with a WR shell there are two important parameters which determine the radius of the reverse shock. The first is the radius at which the WR shell was located at the time of the supernova explosion, since that determines the time frame during which the supernova ejecta could expand freely. This is reflected in the different turn off times of the initial fast increase in the reverse shock radius for the models which contain a WR phase. Model WR0 does not expand as fast initially because the supernova ejecta encounter a higher density CSM, corresponding to the RSG wind, which creates a reverse shock that moves more slowly initially.

The second important parameter is the amount of mass in the WR shell compared to the supernova ejecta mass. Since the latter is constant, only the mass in the WR shell is important this case. The longer the WR phase lasts, the more mass is accumulated in the shell. As a result the collision between this shell and the supernova ejecta will be more violent and cause a reverse shock which moves inward faster with respect to the forward shock. This is represented in the time dependence of the reverse shock radii for the different models. The reverse shock radius

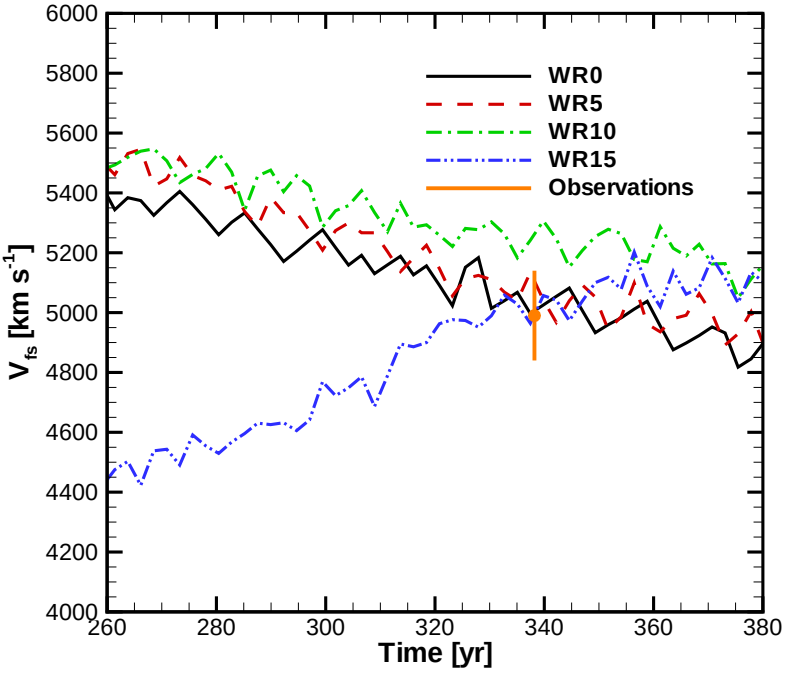

Figure 2.8: Velocity of the forward shock, for the different models, plotted against time. The observations and corresponding uncertainty are again shown in orange. Because of the large differences in the forward shock velocity during the total evolution of the SNR we only plotted a specific range in time. This range shows how the values for the forward shock velocity evolve around the age at which Cas A is thought to be now.

of WR5 keeps on increasing after the collision with the WR shell while the reverse shock radius of WR15 starts moving inward after approximately 300 years.

This is also visible in Fig. 2.10, which shows that the reverse shock velocity of WR15 becomes negative. By comparing the models in this figure we can see that for a longer WR life time, the velocity of the reverse shock at a given time will decrease, which is what we expect from the arguments given above. Together with the reverse shock radius, the velocity shown in Fig. 2.10 shows the largest differences between the four models. These differences give us the best tools to constrain the progenitor of Cas A.

2.4 Discussion and conclusions

We have shown the results of 2-D simulations for the hydrodynamic evolution of a SNR in which, for the first time, the SN ejecta was separated from the CSM. With the Cas A SNR in mind, we investigated the influence of the progenitor wind and

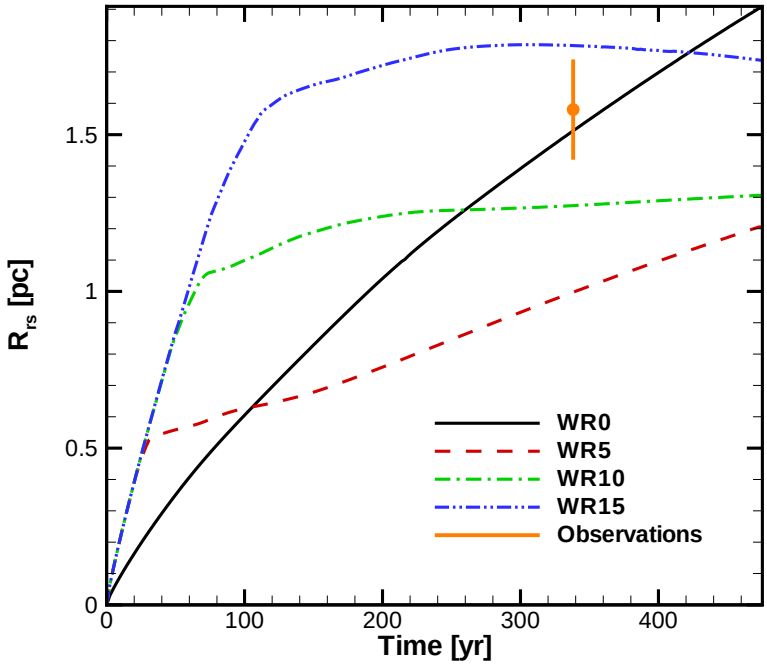

Figure 2.9: Similar to Figure 2.7, but in this case the reverse shock radius is plotted. In orange we show the observational value and its uncertainty. Initially all the reverse shock radii are the same for the models with a WR shell. However, the WR shell radius is different for each model and thus the onset of the decrease in expansion, i.e. the collision of the supernova ejecta with the WR shell, occurs at different times for WR5, WR10 and WR15, ~ 30, ~60 and ~110 years respectively.

the interaction of the supernova ejecta with the wind shaped CSM on the clumping and shock structure of the SNR.

From our simulations we can draw the following conclusions which can be compared with the observations of Cas A:

- When a WR phase occurs, the SNR shows the remainders of the WR shell.
- With an increasing WR life time, the reverse shock velocity in the observers frame, at the current age of Cas A, decreases.
- The longer the WR life time, the larger the range of velocities of both the shocked SN ejecta and the shocked CSM.

The clumping that we find in the result of our SNR models that include a WR phase, is *not* comparable to the QSF seen in Cas A. In the highest density material we find a somewhat larger velocity range, extending to ~1000 - ~2000 km $s^{-1}$for

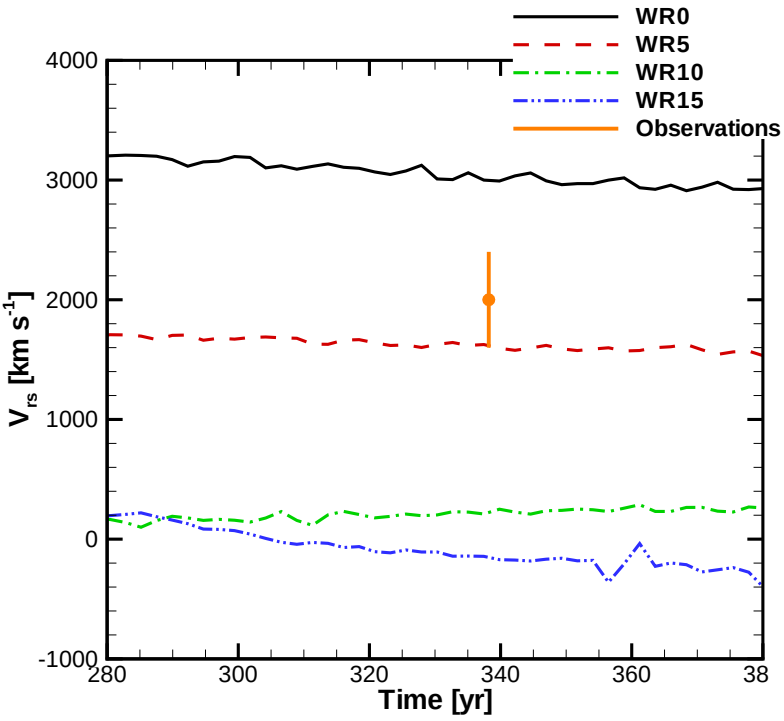

Figure 2.10: Similar to 2.8, but in this case the reverse shock velocity is plotted. The models with a longer WR life time have a more massive WR shell which causes a higher inward velocity of the reverse shock. The model with the highest WR shell mass should thus show the largest inward reverse shock velocity in our frame, which is consistent with our results.

Model WR10 and WR 15, depending on what density range one would consider as a clump. This is inconsistent with the observations for the QSF. For Model WR5 the clumps are destroyed, since no slow moving high density component is visible (Fig. 2.5). Nevertheless, the remainders of those clumps should still be visible in the remnant and are even the dominant emitting component, which we illustrate by showing the radiative energy loss of WR5 and WR10 in Fig. 2.11. This means that even for a very short WR life time of 5000 years remainders of a WR shell will be seen in the SNR. The QSF are therefore an argument against the occurence of a WR phase, which was also suggested by Chevalier & Oishi (2003).

The clumps in our results are located in between the forward and the reverse shock, and their expansion in a 3D picture would correspond to a slowly expanding shell. Since all the emitting components of our result lie in between the two shocks, they should all show a similar distribution when projected onto the sky. This is in contrast with what is seen in the observations. Fig. 3 in Lawrence et al. (1995) shows that the QSF distribution does not coincide with the distribution of the other

emitting components of the Cas A SNR, and that the distribution of the QSF does not have a spherical shape. The same can be seen by comparing Fig. 5 and 10 in Fesen (2001). This comparison also shows that there are some QSF outside the main shell in the southwestern part of the remnant, which does not occur in the models. Also, the spatial scale of the clumps in our results can range up to 0.2 pc, which is inconsistent with the measured sizes of the QSFs in Cas A. The cooling times of the clumps in our results are of the order of hundreds of years ($\tau_{cooling} = \frac{e}{\dot{e}} \geq 100$ yr), which does not correspond to a typical QSF life time of 25 years found by van den Bergh & Kamper (1985).

To be able to explain the QSF in Cas A we would have to invoke another source of clumpiness, since our models are not able to explain the QSF. This other source would have to consist of clumps with properties similar to the QSF currently seen in Cas A. The small size of the QSF in Cas A tells us that they do not significantly influence the large scale dynamics of the SNR. The effect of the clumps from this other source would thus not affect the shock radii and velocities to a large extent and our conclusions would remain valid.

Due to our multi-species approach it can be clearly seen that clumps of SN ejecta can be found very close to the forward shock in models with a WR phase. This is solely due to the presence of a clumpy shell. Although it is of no specific significance to our current investigation, there are other remnants in which similar features are also observed and explained by invoking cosmic ray acceleration at the forward shock (Warren et al. 2005, Cassam-Chenaï et al. 2008). While our models and results do not apply to these specific SNRs, the fact that a clumpy CS shell can have this effect might be of interest to those investigations.

Cosmic ray acceleration is also invoked by Patnaude & Fesen (2008), who find that they need the energy loss due to this process to be able to explain the shock radii and velocities of Cas A. We have not included this process in our simulations. Within our models there is a large set of parameters to be considered, and we have shown that within this parameter space it is possible to find radii and shock velocities which are largely consistent with the observed values. This does not mean we believe cosmic ray acceleration is not of importance, but given the uncertainty in the amount of energy involved in this process one can not unequivocally conclude that cosmic rays are needed in order to explain the structure and kinematics of Cas A.

The differences in the forward shock radii and velocities of our results are not really meaningful, as we could accommodate those by small changes in explosion energy and ejected mass. However, the reverse shock structure varies considerably in our models, and can be used to constrain the progenitor model. The radii of the reverse shock in Models WR0 and WR15 lie closest to the observed value. From this figure alone one could argue that either a WR life time between 10000 and 15000 years or no WR phase at all would give us the required shock radius. By comparing the reverse shock velocity of WR10 and WR15 with the observations it can be seen that the difference is too large and that those models cannot explain the reverse shock velocity seen in the observations. The reverse shock velocity of WR0 does not match the observed value either, but the difference is smaller. If we want to match the reverse shock radius *and* the reverse shock velocity at the same time, a model in which there is no WR phase seems most likely. However, recently there

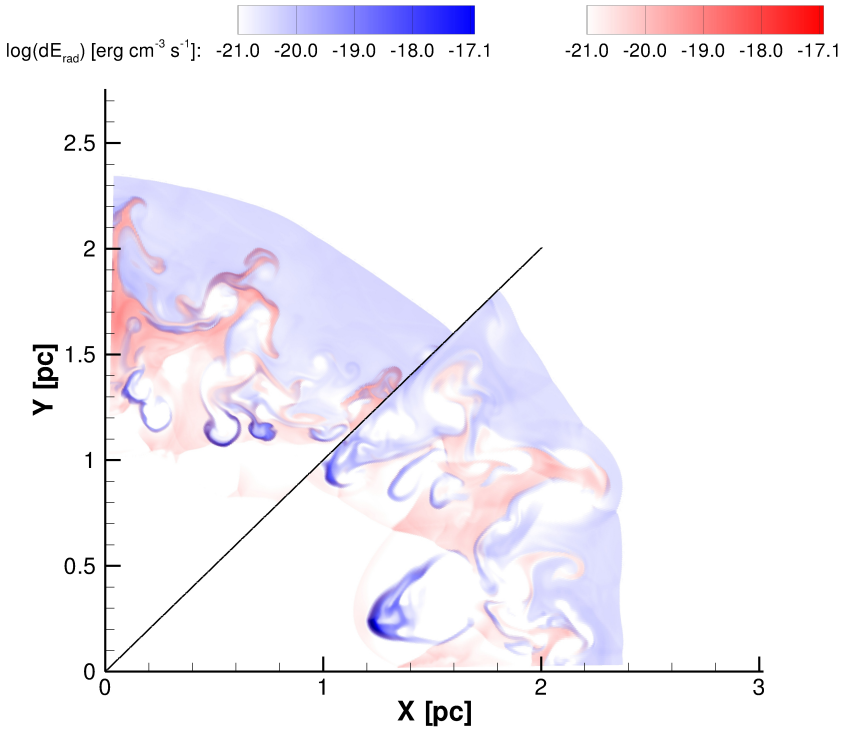

Figure 2.11: Radiative energy loss of the SNR of WR5 (first slice counting clockwise) and WR10 (second slice), similar to Figure 2.6. In both slices the clumps, which are the remnants of the WR shell, can be seen as the strongest emitting component.

has been a debate about the reverse shock velocity in the western part of Cas A, where the velocity is almost zero in our frame, and would be more in line with a long WR phase (Helder & Vink 2008).

Measurements of the reverse shock velocity are sparse and the value mentioned in Morse et al. (2004) is rather uncertain. Fig. 4.6 of DeLaney (2004) shows that the proper motions of X-ray emitting components, which might (Helder & Vink 2008), or might not (Patnaude & Fesen 2008) be identified with material shocked at the reverse shock, show large differences in their expansion rates. In the west of the remnant the expansion rate seems to be smaller ($-0.1\% \sim 0.1\%$ yr^{-1}) than that of the majority of the material ($\sim 0.2\%$ yr^{-1}). An expansion rate of $\sim 0.2\%$ yr^{-1} corresponds to a velocity of the X-ray emitting components of approximately 3000 km s^{-1}, given the reverse shock radius of 1.58 pc. This would imply a reverse shock velocity of approximately 2500 km s^{-1}, which is slightly higher than the value given in Morse et al. (2004) and would be even more consistent with Model WR0.

Our conclusion regarding the visibility of remainders of the WR shell in the SNR only holds for the short WR life times considered here. If the WR life time was much longer, the interaction of the WR wind with other parts of the CSM,

the RSG shell for instance, would alter the structure of the CSM and consequently also the structure and visibility of the SNR. Nevertheless, this does not change our overall conclusion, since we can exclude longer WR life times on the basis of the shock structure and kinematics.

Because the presence of the QSF in Cas A cannot be explained with help of the remainders of the WR shell and because the remainders of that shell do not correspond to any other observed component in the SNR, we can exclude the occurrence of a WR phase. This strengthens the growing evidence for not having a WR phase during Cas A's progenitor life (Schure et al. 2008, Krause et al. 2008, Pérez-Rendón et al. 2009).

Acknowledgments

We thank Michael L. Norman and the Laboratory for Computational Astrophysics for the use of ZEUS MP. This work was sponsored by the Stichting Nationale Computerfaciliteiten (National Computing Facilities Foundation, NCF) for the use of supercomputer facilities, with financial support from the Nederlandse Organisatie voor Wetenschappelijk Onderzoek (Netherlands Organisation for Scientific Research, NWO).

Chapter 3

The Destruction of Cosmological Minihalos by Primordial Supernovae

D. Whalen, B. van Veelen, B.W. O'Shea and M.L. Norman
based on *The Astrophysical Journal; 682-1* (p. 49-76)

We present numerical simulations of primordial supernovae in cosmological minihalos at $z \sim 20$. We consider Type II supernovae, hypernovae, and pair instability supernovae (PISN) in halos from 6.9×10^5 - 1.2×10^7 $M_\odot$, those in which Population III stars are expected to form via H_2 cooling. Our simulations are novel in that they are the first to follow the evolution of the blast from a free expansion on spatial scales of 10^{-4} pc until its approach to pressure equilibrium in the relic HII region of the progenitor, $\sim$ 1000 pc. Our models include nine-species primordial chemistry together with all atomic H and He cooling processes, inverse Compton cooling and free-free emission. The supernovae evolve along two evolutionary paths according to whether they explode in HII regions or neutral halos. Those in HII regions first expand adiabatically and then radiate strongly upon collision with baryons ejected from the halo during its photoevaporation by the progenitor. Explosions in neutral halos promptly emit most of their kinetic energy as x-rays, but retain enough momentum to seriously disrupt the halo. We find that the least energetic of the supernovae are capable of destroying halos $\lesssim 10^7$ $M_\odot$, while a single PISN can destroy even more massive halos. Blasts in HII regions disperse heavy elements into the IGM, but neutral halos confine the explosion and its metals. Primordial supernova remnants develop dynamical instabilities at early times capable of enriching up to 10^6 $M_\odot$ of baryons with metals to levels $\gtrsim 0.01$ $Z_\odot$, well above that required for low-mass star formation. In HII regions, a prompt second generation of stars may form in the remnant at radii of 100 - 200 pc in the halo. Explosions confined by large halos instead recollapse, with infall rates in excess of 10^{-2} $M_\odot$ yr^{-1} that heavily contaminate their interior. This fallback may either fuel massive black hole growth at very high redshifts or create the first globular cluster with a radius of 10 - 20 pc at the center of the halo. Our findings allow the possibility

that the first primitive galaxies formed sooner, with greater numbers of stars and distinct chemical abundance patterns, than in current models.

3.1 Introduction

Numerical studies indicate that primordial stars form in the first pregalactic objects to reach masses of $\sim 5 \times 10^5\ M_\odot$ at $z \sim 20$ - 50 (Bromm et al. 1999, Abel et al. 2000, 2002, Gao et al. 2007). The models suggest that Population III stars form in isolation (one per halo) and that they are likely very massive, from 100 to 500 $M_\odot$. More recent work surveying a larger sample of halos (O'Shea & Norman 2007) extends the lower mass limit of primordial stars down to 15 $M_\odot$. Very massive stars easily photoionize their halos, typically in a few hundred kyr with final HII region radii of 2500 - 5000 pc while HII regions of less massive stars are confined to very small radii ($< 10^{-3}$ pc) by the high central densities deep in the halo (Whalen et al. 2004, Kitayama et al. 2004, Alvarez et al. 2006, Abel et al. 2007, Johnson et al. 2007, Yoshida et al. 2007, Wise & Abel 2008b,a). In the latter case, high recombination rates and pressure from overlying matter due to the depth of the halo dark matter potential well halts the expansion of the heated bubble (Franco et al. 1990). Unlike massive stars in the Galaxy today, little mass loss occurs in Population III stars because there are no line-driven winds from their pristine atmospheres (Baraffe et al. 2001, Kudritzki 2000, Vink et al. 2001), although mixing in rapidly rotating stars may cause some mass loss later in their lives (Meynet et al. 2008). Consequently, winds do not clear gas from cosmological halos in the first generation of stars as they do from molecular cloud cores today. However, if the ionization front (I-front) of the star breaks out of the halo it will sweep more than half of the baryons interior to the virial radius into a thick shell $\sim$ 100 pc in radius by the end of the life of the star (Whalen et al. 2004, Kitayama et al. 2004). The diffuse gas enclosed by the shell is uniform and at densities far lower than in the original halo, 0.1 - 1 cm^{-3} instead of more than 10^{10} cm^{-3}.

The ultimate fate of a Population III star depends on its mass at the end of its main sequence lifetime (MSL). Those lying between 10 $M_\odot$ and 40 $M_\odot$ die in Type II supernova explosions, ejecting roughly 20% of their mass into the intergalactic medium (IGM) as metals and leaving behind a compact remnant. Stars between 140 $M_\odot$ and 260 $M_\odot$ explode in extremely energetic pair instability supernovae (PISN) hundreds of times more powerful (Heger & Woosley 2002). As much as 50% of the mass of the star is dispersed as heavy elements into the IGM in such events, with no compact remnant. However, these predictions are based on one-dimensional non-rotating stellar evolution models that make a range of assumptions (e. g. mixing parameters) and should be considered qualitative, rather than quantitative, in nature. How far elements are expelled from the star depends strongly on the state of the halo prior to the explosion. Supernova (SN) remnants in halos completely ionized by the star typically expand to half the diameter of the HII region. The shock front comes into pressure equilibrium with the hot recombining gas more quickly than if the blast propagates in a neutral medium of comparable density (Greif et al. 2007). Supernovae in neutral halos, which result when low-mass Population III stars fail to ionize them, evolve quite differently. Because no winds evacuate gas from the

center of the halo, the blast encounters circumstellar densities several orders of magnitude greater than in OB associations in the Galaxy, with much higher energy losses at very early times. Since the blast energy is much greater than the binding energy of the gas in the halo, it is often supposed that PISN easily destroyed halos. Here, destruction of the halo means complete expulsion of its gas, not dispersal of the dark matter itself, which remains mostly undisturbed. However, as Kitayama & Yoshida (2005) point out, this argument ignores radiative losses from the shock in the large densities deep in the halo. They find that bremsstrahlung and inverse Compton cooling (IC) radiate away the explosion's energy before it even sweeps up its own mass in ambient gas, quenching the blast and preventing any dissemination of metals into the halo. Explosions with hundreds of times the binding energy may be necessary to disperse more massive halos under these conditions.

However, a difficulty with this and other studies of primordial supernovae in cosmological halos is how the explosion itself is initialized. This is typically done by depositing the energy of the blast as thermal energy on the mesh and allowing pressure gradients to launch shocked flows into their surroundings (Bromm et al. 2003, Kitayama & Yoshida 2005, Greif et al. 2007). This is partly justified for explosions in HII regions whose central densities are quite low and in which early radiative losses from the remnant are minimal. Too much energy loss from the early remnant would be ignored by this approach for SN in neutral halos, which cool strongly from very early times due to high ambient densities. In fact, explosions initialized by thermal pulses in neutral halos cool before any of their energy can be converted into motion (Kitayama & Yoshida 2005). When the energy of the blast is deposited as heat to central mesh zones, their temperatures skyrocket to tens of billions of degrees K, driving extreme bremsstrahlung and IC losses before pressure gradients can accelerate any flows. These initial conditions do not properly represent the free expansion that actually erupts through the stellar envelope and whose momentum cannot be radiated away. The early stages of the explosion in a nearly undisturbed halo are much better modeled by a cold free expansion in which the energy of the blast is kinetic rather than thermal. Furthermore, supernovae modeled in cosmological density fields with smoothed particle hydrodynamics methods (Bromm et al. 2003, Greif et al. 2007) also lack the numerical resolution to capture the early hydrodynamic behavior of the blast wave. Dynamical instabilities might manifest that lead to early mixing of heavy elements in the ejecta with ambient halo material on much earlier time scales than in current simulations.

How easily neutral halos are destroyed by primordial supernovae and how metals mix with the early IGM thus remains unclear. One key issue is how much gas is displaced in the halo by the momentum of the ejecta after its energy is lost to cooling processes in the expanding flow at early times. In HII regions the shock later strongly interacts with the dense shell of ionized gas expanding within the HII region. How well do metals in the remnant mix with the dense shell, and if dynamical instabilities arise that fragment the shock into enriched clumps, are they liable to collapse into new stars? Numerical simulations excluding these phenomenon indicate that metals do not significantly mix with the IGM until gas falls back into the dark matter potential after about a Hubble time (Greif et al. 2007).

Capturing the true evolution of the blast presents numerical challenges due to the spatial scales at play. To accurately represent the initial ejecta as a free ex-

pansion, its hydrodynamical profile cannot extend beyond radii that enclose more surrounding gas than ejecta mass. In the high central densities of neutral halos such radii are 5×10^{-4} - 1×10^{-3} pc, but the blast must then be evolved to tens or hundreds of parsecs to evaluate its true impact on the halo. Furthermore, multiple sites of intense luminosity will erupt in the flow over all these scales from the earliest times, so the chemistry of the flow must be solved consistently with hydrodynamics to determine where gas is collisionally ionized and therefore strongly radiating. The attendant time scales can restrict integration times to much lower values than Courant times.

To address these questions we have performed one-dimensional models of Type II supernovae, hypernovae, and PISN in neutral and ionized cosmological halos at redshift 20. Our initial conditions are spherically-averaged halos derived from cosmological initial conditions with the Enzo adaptive mesh refinement (AMR) code (O'Shea et al. 2004) that are photoionized by the star in the ZEUS-MP reactive flow radiative transfer code (Whalen & Norman 2006). The aim of our survey is to determine the explosion energies required to destroy cosmological halos that are thought to form primordial stars by H_2 cooling. We also evaluate their observational signatures and how their metals will mix with the ambient medium as a prelude to three-dimensional AMR calculations now in progress.

Our radiation hydrodynamics scheme and initial profiles for the free expansion are presented in § 2. We also describe the expanding grids used in this study and the time-dependent boundary conditions that present the ambient medium to the expanding flow. HII region profiles for the explosions and the grid of supernova and halo models selected for this survey are outlined in § 3. The evolution of blasts in both neutral halos and HII regions are examined together with dominant energy loss mechanisms for each case in § 4. We discuss observational measures for both kinds of explosion in § 5, chemical enrichment of baryons in the halos in § 6 and conclude in § 7.

3.2 Numerical Method

Three-dimensional halo baryon profiles computed from cosmological initial conditions are extracted from an Enzo AMR run and spherically averaged into one-dimensional density fields. These profiles are then photoionized over the main sequence lifetime of the SN progenitor with the ZEUS-MP astrophysical fluid hydrodynamics code. We then initialize one-dimensional explosion profiles in the ionized halos and evolve the blasts in a separate calculation. ZEUS-MP has been modified to solve explicit finite-difference approximations to Euler's equations of fluid dynamics coupled to 9-species primordial chemistry with photoionization rate coefficients computed from multifrequency photon-conserving UV transport (Whalen & Norman 2008a). The fluid equations are

$$\frac{\partial \rho}{\partial t} = -\nabla \cdot (\rho \mathbf{v}) \tag{3.1}$$

$$\frac{\partial \rho v_i}{\partial t} = -\nabla \cdot (\rho v_i \mathbf{v}) - \nabla p - \rho \nabla \Phi - \nabla \cdot \mathbf{Q} \tag{3.2}$$

$$\frac{\partial e}{\partial t} = -\nabla \cdot (e\mathbf{v}) - p\nabla \cdot \mathbf{v} - \mathbf{Q} : \nabla \mathbf{v} \tag{3.3}$$

where ρ, e, and the v_i are the mass density, internal energy density, and velocity components of each zone, and p = (γ-1) e and **Q** are the gas pressure and the von Neumann-Richtmeyer artificial viscosity tensor (Stone & Norman 1992).

Nine additional continuity equations are solved to advect H, H^+, He, He^+, He^{++}, H^-, H_2^+, H_2, and e^-, which are assumed to share a common velocity distribution. Thirty reactions among these primordial species are followed with the nonequilibrium rate equations of Anninos et al. (1997)

$$\frac{\partial \rho_i}{\partial t} = \sum_j \sum_k \beta_{jk}(T)\rho_j\rho_k + \sum_j \kappa_j \rho_j \tag{3.4}$$

where β_{jk} is the rate coefficient of the reaction between species j and k that creates (+) or removes (-) species i, and the κ_j are the ionization rates. The continuity equations for each reactant are updated in the advection routines and the reaction network is evolved in a separate operator-split semi-implicit substep. We enforce charge and baryon conservation at the end of each hydrodynamic cycle by assigning any error between the species or charge sums and ρ to the largest of the species to bring them into agreement with ρ. Microphysical cooling and heating are included with an isochoric operator-split update to the energy density evaluated each time the reaction network is solved:

$$\dot{e}_{\rm gas} = \Gamma - \Lambda \tag{3.5}$$

Here, Γ is the rate at which photons at all frequencies in the calculation deposit heat into the gas as described in Whalen & Norman (2008a) and Λ is the sum of the cooling rates due to collisional ionization and excitation of H and He, recombinations in H and He, inverse Compton scattering (IC) from the CMB, and bremsstrahlung emission. H_2 cooling (Galli & Palla 1998) is included in the HII region calculation but not in the evolution of the SN blast, whose high temperatures and strong shocks destroy the fragile hydrogen molecules on the time scales of our models. We do not include metal line cooling, but reserve it for three-dimensional models now in preparation.

Photon-conserving UV transport in the spherical polar coordinate grid used in this study is performed by solving the static approximation to the equation of radiative transfer in flux form

$$\nabla \cdot \mathbf{F} = -\chi \mathbf{F}_r, \tag{3.6}$$

where χ is the inverse mean free path of a UV photon in the neutral gas

$$\chi = \frac{1}{n\sigma}, \tag{3.7}$$

to compute the total absorption rate in each zone by photon conservation, which mandates that the number of absorptions in a zone is equal to the photons entering the zone minus those exiting each second. In terms of flux, this difference reduces to

$$\begin{aligned} n_{\rm abs} &= F_i \left(1 - e^{-\chi(r_{i+1}-r_i)}\right) \\ &\times \frac{r_i^2\ (\phi_{k+1} - \phi_k)\left(\cos\theta_j - \cos\theta_{j+1}\right)}{h\nu} \end{aligned} \tag{3.8}$$

Individual interaction rates (photoionizations, photodetachments, and photodissociations) are obtained from the total rate according to the prescription

$$n_i = \frac{1\ -\ e^{-\tau_i}}{\sum_{i=1}^{n} 1\ -\ e^{-\tau_i}}\, n_{\rm abs}. \tag{3.9}$$

which are then converted into the photoionization rate coefficients required by the reaction network

$$k_i = n_i \cdot \frac{1}{n_{\rm spec}\, V_{\rm cell}}, \tag{3.10}$$

where n_{spec} is the number density of the species with which the photons are interacting. We adopt the on-the-spot (OTS) approximation by assuming that recombinations to the ground state balance photoionizations by diffuse photons within a zone, so we do not explicitly transport recombination radiation. Complete descriptions of the photon conserving UV transport from which radiative rates in the reaction network are derived can be found in Whalen & Norman (2006, 2008a).

3.2.1 Free-Expansion Blast Profiles

We take density and velocity profiles for the free expansion from Truelove & McKee (1999), where it is shown that at a given time the ejecta density can be approximated by a flat inner core and steeply declining outer edge:

$$\rho(v,t) = \begin{cases} F \cdot t^{-3} & \text{for} \quad v \le v_{\rm core} \\ F \cdot t^{-3} \cdot (\frac{v}{v_{\rm core}})^{-n} & \text{for} \quad v_{\rm core} < v \le v_{\rm max} \\ 0. & \text{for} \quad v > v_{\rm max} \end{cases}, \tag{3.11}$$

$$v(r,t) = \frac{r}{t} \ \text{ for } \ t > 0\ . \tag{3.12}$$

Here, ρ is the density, t is the time, v is the velocity and r is the radius. F and $v_{\rm core}$ are normalization constants which must be determined. The time dependence in the density is due to the expansion of the ejecta: as it grows in volume by r^3 its density decreases by $r^{-3} \propto t^{-3}$. The inner region of the free expansion, $v \le v_{\rm core}$, has a constant density and the outer region, $v > v_{\rm core}$, decreases by a power law with index n. Such profiles, with $n = 9$, are usually assumed for core collapse supernovae (Truelove & McKee 1999, Dwarkadas 2005, Chugai & Chevalier 2006). The early evolution of the blast is insensitive to the choice of $r_{\rm max}$, unless it exceeds the radius enclosing an ambient mass greater than the ejecta mass.

The two normalization constants, F and $v_{\rm core}$, are determined from the ejecta mass $M_{\rm ej}$ and energy $E_{\rm ej}$. The energy is assumed to be entirely kinetic. To calculate these constants we first choose a maximum radius $r_{\rm max}$ (> 0) that defines the leading

edge of the SN ejecta and a maximum velocity $v_{\rm max}$ for the remnant. This radius is a free parameter and is usually set so that the enclosed baryonic mass in the halo equals $M_{\rm ej}$. The maximum velocity is set to 3×10^4 km/s, corresponding roughly to that observed in core-collapse supernova explosions. We set $r_{\rm min} = 0$ in all our models.

To determine F and $v_{\rm core}$, we first set $t = t_{\rm max} = r_{\rm max}/v_{\rm max}$, the time by which the leading edge of free expansion has self-similarly grown to $r_{\rm max}$, the initial radius we have chosen for the blast. Using equations 3.11 and 3.12 and choosing $F = 1$ and $v_{\rm core}$ to be some small arbitrary value, we perform the following integrations:

$$M_{\rm ej} = \int_{r_{\rm min}}^{r_{\rm max}} 4\pi r^2 \cdot \rho(v,t) {\rm d}r \, . \tag{3.13}$$

$$E_{\rm ej} = \int_{r_{\rm min}}^{r_{\rm max}} 4\pi r^2 \cdot \frac{1}{2}\rho(v,t) v(t)^2 {\rm d}r \, , \tag{3.14}$$

Neither of these integrations will return correct values for $M_{\rm ej}$ and $E_{\rm ej}$ at first because F and $v_{\rm core}$ were arbitrarily chosen. Selecting a new F' equal to $M_{\rm ej}$ divided by the mass obtained from Eq. 3.13, which guarantees the first integration equals the correct ejecta mass by construction, we repeat the second integration and check if it is equal to $E_{\rm ej}$. If so, F' and $v_{\rm core}$ are those needed to construct the density profile. If not, we increase the value for $v_{\rm core}$, again set $F = 1$, obtain a new F', which partly depends on the new $v_{\rm core}$, from the first integral, and then compute a new $E_{\rm ej}$ with the second integral. We repeat this two-step procedure until the latest choice of $v_{\rm core}$ and F' returns the correct value of $E_{\rm ej}$ in the second integration; the F' in this final cycle is the F we apply to the density profile on the grid. Once we have F and $\rm v_{core}$, and recalling that $t = t_{\rm max} = r_{\rm max}/v_{\rm max}$ and $v = r/t_{\rm max}$, we recast eq 3.11 as a function of r in order to initialize densities on the grid.

Analytical expressions can be found for the normalization constants F and $v_{\rm core}$ without resorting to iteration in certain circumstances. Equations (3.11) and (3.12) can be substituted into Equations (3.14) and (3.13) to obtain

$$M_{\rm ej} = 4\pi t_{\rm max}^{-3} F \left(\frac{r_{\rm core}^3 - r_{\rm min}^3}{3} - r_{\rm core}^n \frac{(r_{\rm max}^{3-n} - r_{\rm core}^{3-n})}{3-n} \right) , \tag{3.15}$$

$$E_{\rm ej} = 2\pi t_{\rm max}^{-5} F \left(\frac{r_{\rm core}^5 - r_{\rm min}^5}{5} - r_{\rm core}^n \frac{(r_{\rm max}^{5-n} - r_{\rm core}^{5-n})}{5-n} \right) , \tag{3.16}$$

Here, $t_{\rm max} = r_{\rm max}/v_{\rm max}$, $r_{\rm core} = v_{\rm core} \cdot t_{\rm max}$ and $r_{\rm min}$ and $r_{\rm max}$ are the minimum and maximum radius of the free expansion, respectively. If $r_{\rm min} \ll r_{\rm core} \ll r_{\rm max}$, which is generally true, then F and $v_{\rm core}$ can be expressed as (Truelove & McKee 1999):

$$v_{\rm core} = \frac{r_0}{t_{\rm core}} = \left(\frac{10 E_{\rm ej}(n-5)}{3 M_{\rm ej}(n-3)} \right)^{\frac{1}{2}} , \tag{3.17}$$

$$F = \frac{1}{4\pi n} \cdot \frac{(3(n-3)M_{\rm ej})^{\frac{5}{2}}}{(10(n-5)E_{\rm ej})^{\frac{3}{2}}} = \frac{10(n-5)E_{\rm ej}}{4\pi n} \cdot v_{\rm core}^{-5} \, . \tag{3.18}$$

We iterate to find F and $v_{\rm core}$ because the assumptions underlying the analytical forms might not be satisfied for all ejecta profiles discretized on a mesh. At times $r_{\rm core}$ could lie close to the inner or outer boundary of the grid. In this case the analytical solution is different from the one found iteratively and could introduce errors in the mass and energy on the grid if applied. To prevent such errors we always solve for F and $v_{\rm core}$ numerically.

3.2.2 Moving Grid/Boundary Conditions

As noted earlier, to realistically represent the early remnant as a free expansion in neutral halos it cannot enclose more halo gas than its own mass in ejecta, which confines its initial extent to less than 0.001 pc if the halo. This restriction is problematic, given that its expansion must be accurately resolved out to the virial radius of the halo, $\sim$ 100 pc. However, this can be accomplished with a fixed number of mesh points if the grid itself expands with the flow and always maintains its outer boundary beyond the expanding shock front. In this scenario only the surrounding halo just beyond the shock can be present on the grid at any time, so as the outer boundary of the grid grows with time its densities, energy, and velocities must be updated according to its given position within the halo. In this way the expanding flow always encounters the densities it would if the entire halo resided on the grid. An additional benefit is that Courant times become longer as the grid grows, accelerating the execution of the calculation.

We activate moving grids in the radial coordinate in ZEUS-MP for the models in this study, modifying the outer boundary conditions every hydrodynamical time step with an operator-split update following the calculation of a new grid. At the start of the simulation we allocate 80% of the mesh to the free expansion profile, reserving the outer 20% for the ambient halo. Every time step thereafter the outer 10% of the grid is swept for the maximum radial gas velocity and its position on the mesh. A grid velocity describing homologous expansion is then assigned to each grid point such that the grid velocity at the radius of the previous maximum in gas velocity is three times this maximum. The factor of 3 guarantees that the flow never reaches the outer boundary, where inflow conditions are reset each time step to ensure the remnant always encounters the correct ambient medium. If the velocity of the grid is non-zero, the entire radial grid is updated in the following manner. First a new outer boundary is determined from the old boundary, the grid velocity and the current time step. A new grid is then computed such that the radial cells, whose number remains fixed, are redistributed equally over the new range in radius. See Hayes et al. (2006) for a discussion of ZEUS-MP's moving Eulerian grid option.

Species densities, energies, and velocities on the outer boundary are updated each hydrodynamical time step by interpolating from a data table whose entries are binned by radius. The profiles in these tables are those of the halo photoionized by the original star over its main sequence lifetime, which were computed in the separate calculation with nine-species primordial chemistry and radiative transfer that was described above. The flow values assigned to the outer boundary depend upon the position bin into which the boundary falls at a given time step. We describe the stellar masses and halos used in our models in the following section.

3.2.3 Static Dark Matter Potential

Primordial supernova remnants evolved in much deeper gravitational potentials due to dark matter than SN in the galaxy today. Gravitational potentials in the halos in our study are dominated by baryons at radii of less than a parsec and by dark matter at larger radii. We neglect the self-gravity of the remnant on scales below a parsec because of its large kinetic energy but include the potential of the dark matter on all scales. Since merger times at $z \sim 20$ are approximately 20 Myr, much longer than the dynamical times of the remnant, to good approximation the gravitational potential of the dark matter can be held fixed in our simulations. We interpolate the dark matter potential of the halo onto the initial grid at the beginning of the run and onto each new grid thereafter, but the potential itself never evolves. We apply this potential to force updates to the gas velocities throughout the calculation. The interpolation substep is operator split from the time-dependent boundary updates of the fluid variables described above.

3.3 SN Progenitor HII Regions

Table 3.1: Halos

Halo	$J_{\rm LW}$	M ($M_\odot$)	$z_{\rm coll}$	$E_{\rm B}$ (erg)
1	0	6.9E+05	24.1	1.53E+49
2	3.16E-23	2.1E+06	20.4	1.10E+50
3	1.00E-21	1.2E+07	17.3	2.50E+51

The halos adopted for our study were taken from O'Shea & Norman (2008), who examined the formation of Pop III stars in a range of Lyman-Werner (LW) backgrounds (11.18 - 13.6 eV). Since more baryons are required to shield H_2-cooled cores from dissociation as the LW background rises, the minimum halo mass required to form a star rises with decreasing redshift. We consider three different halos that span the masses for which Pop III stars are expected to form by H_2 cooling. Their properties are summarized in Table 3.1 and their spherically-averaged baryon density profiles are shown in Figure 3.1. In column 1, we list the halo number, in column 2 the LW background in which they form, in column 3 their mass, in column 4 their redshift, and in column 5 their binding energy. SN progenitors were chosen according to the types of explosions that were possible in primordial halos: 15 $M_\odot$ (Type II supernova), 40 $M_\odot$ (hypernovae), and 260 $M_\odot$ (PISN). Their properties are tabulated in Table 3.2 (Schaerer 2002). To obtain accurate circumstellar media for the supernovae, each star was allowed to ionize each halo and then explode, for a total of nine models listed in Table 3.3. In Table 3.1 $J_{\rm LW}$ is the mean intensity of LW photons in which the halos form, centered at 12.87 eV in units of erg^{-1} cm^{-2} Hz^{-1} sr^{-1} and $z_{\rm coll}$ is the redshift at which the star appears in the halo. The binding energy of the gas $E_{\rm B}$ in each halo can be approximated by that of a homogeneous sphere, which is given by

$$E_{\rm B} = \frac{3}{5}\,\frac{GM_{\rm h}m_{\rm b}}{R_{\rm vir}}, \tag{3.19}$$

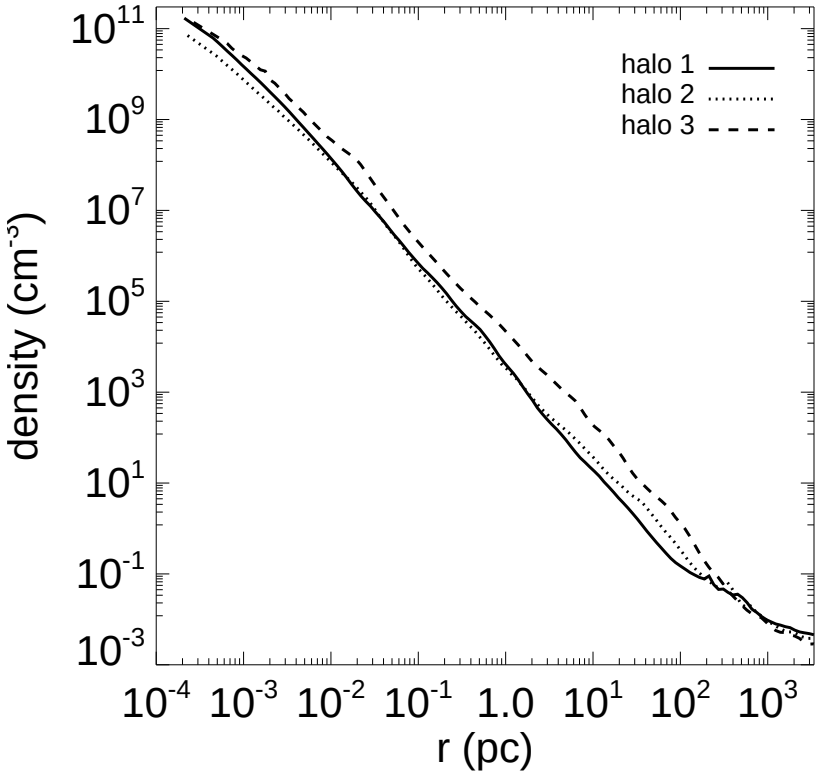

Figure 3.1: Spherically-averaged baryon density profiles for the halos examined in this study.

where $M_{\rm h}$ and $m_{\rm b}$ are the total halo and baryon masses, respectively, and $R_{\rm vir}$ is the virial radius of the halo. In Table 3.2 $\dot{n}_{\rm ph}$ is the total number of ionizing photons emitted per second.

Table 3.2: SN Progenitors

M ($M_\odot$)	$t_{\rm MSL}$ (Myr)	log $T_{\rm eff}$	log $L/L_\odot$	$\dot{n}_{\rm ph}$ (s^{-1})
15	10.4	4.759	4.324	1.861E+48
40	3.864	4.900	5.420	2.469E+49
260	2.106	5.004	6.721	3.272E+50

3.3.1 Problem Setup

The star was centered in a 200 zone one-dimensional spherical coordinate mesh with reflecting and outflow inner and outer boundary conditions, respectively. Cell

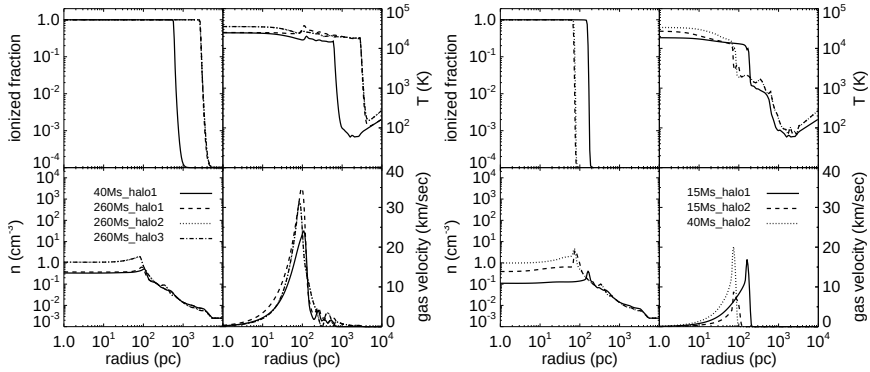

Figure 3.2: Density, temperature, ionization fraction, and velocity profiles of the SN progenitor HII regions at the end of the life of the stars. Left: HII regions that break out of the halo. Solid: 40Ms_halo1; dashed: 260Ms_halo1; dotted: 260Ms_halo2; dot dash: 260Ms_halo3. Right: HII regions that are confined to the virial radius of the halo. Solid: 15Ms_halo1; dashed: 15Ms_halo2; dotted: 40Ms_halo2. Since the HII region radii of the 15 $M_\odot$ and 40 $M_\odot$ stars in halo 3 are below the resolution limit of the radiation calculation, their hydrodynamical profiles are considered to be those of the neutral halo.

sizes were ratioed by the parameter β according to the prescription

$$\frac{\Delta r_{i+1}}{\Delta r_i} = \beta. \tag{3.20}$$

Table 3.3: Primordial SN Explosion Models

halo	15 $M_\odot$	40 $M_\odot$	260 $M_\odot$
1	15Ms_halo1	40Ms_halo1	260Ms_halo1
2	15Ms_halo2	40Ms_halo2	260Ms_halo2
3	15Ms_halo3	40Ms_halo3	260Ms_halo3

We applied β from 1.049 to 1.055 to concentrate zones at the origin, both to resolve the central core and density drop and to obtain the maximum time step capable of accurately capturing the emergence of the I-front from the core. The outer boundary in all the HII region models was 10 kpc and the inner boundary of each model was chosen to enclose a volume at the center of the neutral halo equal in mass to the star. In doing so, we assume that all of this enclosed gas goes into forming the star and that the densities just beyond this volume are those that the nascent I-front encounters. In lieu of more accurate models of the environment of the newborn star, these measures ensure the I-front breaks out into the proper ambient densities. For a given star and halo, the inner boundary for the HII region calculation is thus different for the inner boundary chosen for the explosion, which is zero in our models as noted in section 2.1. This choice is inappropriate for the HII region calculation because it would present higher initial densities to the emerging

front than it really encounters. The inner problem radii vary from 2.6×10^{-3} - 1.4 $\times 10^{-2}$ pc.

Forty equally-spaced energy bins were allocated to the radiation transport from 0.755 eV to 13.6 eV and 80 logarithmically-spaced bins were partitioned from 13.6 eV to 90 eV. We found it necessary to include all nine species in our UV breakout models. Breakout of the I-front from the 15 $M_\odot$ star is borderline in the more massive halos and may be prevented if a dense shell forms in the front by H_2 cooling. However, H_2 chemistry is problematic at the inner boundary as photons propagate through the central zone. The hard UV spectrum significantly broadens the emergent front, resulting in a protracted period of partial ionization at warm temperatures in the first zone. This, together with very large central densities, results in unrealistically high H_2 formation rates that violate species conservation. This difficulty was eliminating by simply turning off H_2 chemistry until the central zone was completely ionized. Each model was evolved for the main sequence lifetime of the star in the halo. We tabulate final HII region radii for each model in Table 3.4. Final densities, temperatures, ionization fractions, and velocities for all runs in which HII regions form are shown in Figure 3.2.

Table 3.4: HII Region Radii (pc)

halo	15 $M_\odot$	40 $M_\odot$	260 $M_\odot$
1	161.5	599.2	2843
2	70.1	74.1	2694
3	———	———	2694

3.3.2 HII Region Breakout

The HII regions in this survey fall into two classes. Those confined to the virial radius of the halo or less and are bounded by subsonic D-type fronts are shown in the right panel of Figure 3.2. Those that flash-ionize the halo on relatively short time scales and propagate into the IGM as supersonic R-type fronts appear in the left panel of Fig 3.2. The I-fronts of very massive primordial stars in cosmological halos first transform from R-type to D-type at radii of less than a parsec but then revert back to R-type in a few hundred kyr and completely overrun the halo (Whalen et al. 2004, Kitayama et al. 2004). The I-front exits so rapidly that steep drops in the halo density profile are frozen in place as they are ionized. Once ionized and isothermal, the density gradients become large pressure gradients that launch shocked flows outward from the center. Ionized core shocks can evict more than half of the baryons from the virial radius of the halo over the lifetime of the star, piling the gas up into a dense shell that surrounds an evacuated cavity of very diffuse gas ($\lesssim 0.1$ cm^{-3}). This is evident for the 260 $M_\odot$ star in halos 1, 2 and 3 in the left panel of Figure 3.2, which are ionized out to kpc scales. The velocity of the ionized core shock is determined both by the postfront temperature and the slope of the density profile when ionized: it is typically 20 - 40 km s^{-1}. This is reminiscent of the velocities found in self-similar flow of an ionized r^{-2} medium (Chevalier 1997, and references therein). We note that the 40Ms_halo1 model is an intermediate case

in that the R-type front breaks through the neutral shell just at the end of the star's life and barely overruns the halo.

3.3.3 Trapped HII Regions

Less massive stars drive weaker I-fronts that either do not revert to R-type or even propagate into the halo at all, as in the case of the 15 $M_\odot$ or 40 $M_\odot$ stars in halo 3. At the inner radii at which we initialize the respective H II region calculations (2.0e-3 - 0.01 pc), the densities in halo 3 are 2 - 5 times greater than those in halo 1, so recombination rates are greater there by a factor of 4 - 25. There is also more pressure downward on the HII region bubble in halo 3 because there is more overlying matter in its deeper potential well. The lower photon emission rates of the 15 $M_\odot$ and 40 $M_\odot$ stars cannot compete with these effects, and the HII region radius remains below the resolution limit of the radiation calculation. Not even an ultracompact (UC) HII region forms, so we take the halo to be essentially neutral and undisturbed at the end of the life of the star. In contrast, the I-fronts in the 15Ms_halo1, 15Ms_halo2, and 40Ms_halo2 models do escape the core but cannot escape the virial radius. They remain D-type, as seen in the relative positions of the breaks in the ionization fractions and the shocks in the right panel of Figure 3.2. The density structure of the D-type fronts differs from the R-type fronts above. Since the expansion rate of the dense neutral is subsonic with respect to the sound speed in the HII region, acoustic waves level the densities in the ionized gas to flat uniform values as the shock expands.

We expect a supernova remnant's greatest energy losses in HII regions to occur upon impact with the shocked neutral or ionized shell. Prior to its encounter with the shock the remnant will generally experience greater radiative cooling in HII regions bounded by D-type fronts than in halos that are flash-ionized because their interiors have somewhat higher densities. However, to first order the effect of any HII region that forms in a cosmological halo is to greatly reduce the ambient densities into which the SN ejecta erupt, from $\sim 10^{11}$ cm^{-3} to $\lesssim 1$ cm^{-3}. This prolongs the free-expansion of the blast and delays cooling. Radiative and losses in neutral halos will be prompt because the remnant initially encounters much higher densities than in HII regions. In the majority of our models, the H II region of the star drives most of the baryons from the halo by photoevaporation, but a supernova explosion is still necessary to remove 90% of the gas from the halo, which is the criterion for its destruction (Kitayama & Yoshida 2005). The final density, energy, velocity, and abundance profiles for each HII region are tabulated in data files. The time-dependent outer boundary updates interpolate these data to ensure that the SN remnant expands into the correct ambient medium.

3.4 SN Blast Wave Evolution

The Truelove & McKee (1999) free-expansion solution for the supernova blast is completely parametrized by the mass, kinetic energy, and maximum velocity of the ejecta, which are listed in Table 3.5 (Heger & Woosley 2002, Tominaga et al. 2007). We also include the mass of the heavy elements expelled by each supernova, $M_{\rm el}$, in Table 3.5. It should be noted that pair-instability blast energies are not well

constrained in present stellar evolution models, and that while the star is thought to be completely dispersed it is not clear how much of its mass goes into the ejecta. For simplicity, we assume that all the mass of the PISN progenitor is in the free expansion. We overlay initial density and velocity profiles for the 15Ms_halo3 and 40Ms_halo1 models in Figure 3.3. Note the enormous disparity in ambient density between blasts initialized in neutral halos and in HII regions. We adopt a power law $n = 9$ in eq 3.11 for all of our blast profiles. The free expansion is initialized on a spherical coordinate mesh with 250 uniform zones with reflecting and outflow boundary conditions, respectively. The free expansion occupies the first 200 zones and is joined directly without smoothing or interpolation to the circumstellar medium, which occupies the outer 50 zones. The temperature of the ejecta is set to 1000 K (the temperature of the ambient medium is determined by the gas energy density interpolated in each zone from the halo table data). Since it is relatively cool, the ejecta is assumed to be nearly neutral, with only the small ionization fraction $\sim 10^{-4}$ expected for primordial gas at $z \sim 20$. In reality, whether the ejecta is ionized or neutral matters little because the energy required for its complete ionization is only a small fraction of the energy of the blast and is not significant to its kinematics, as will be shown later.

We deactivate the transport of ionizing radiation during the evolution of the ejecta but retain nine-species primordial chemistry and gas energy updates due to radiative cooling with the hydrodynamics. Collisional excitation and ionization cooling of H, He, and He^+, recombinational cooling of H^+, He^+, and He^{++}, bremsstrahlung cooling, and inverse Compton cooling are included in the energy equation. The inner boundary of each problem was $r = 0$ and the outer boundary was that which would enclose a volume of neutral halo equal in mass to the ejecta, whether or not the halo is ionized by the star. For halos 1 and 3 the outer problem radius was 0.0005 pc and for halo 2 it was 0.0015 pc, whether or not the halo was ionized by the progenitor. This guarantees that the blast has not yet swept up its own mass in the halo or departed from a free expansion, and that all energy losses from the remnant are captured from the earliest times. Such small radii for the outer boundary are unnecessary for explosions in HII regions, in which blasts remain free expansions for a parsec or more, but are adopted anyway for simplicity.

Table 3.5: Blast Parameters

star	M_{ej} ($M_\odot$)	M_{el} ($M_\odot$)	E_{ej} ($M_\odot$)	v_{max} (km s^{-1})
15 $M_\odot$	13.52	5.94	1.0E+51	30000
40 $M_\odot$	34.43	20.43	3.0E+52	30000
260 $M_\odot$	260	125.27	1.0E+53	30000

Primordial supernovae in cosmological halos follow two distinct evolutionary paths depending on whether they explode in neutral clouds or in HII regions. We now examine the evolution of each type of remnant.

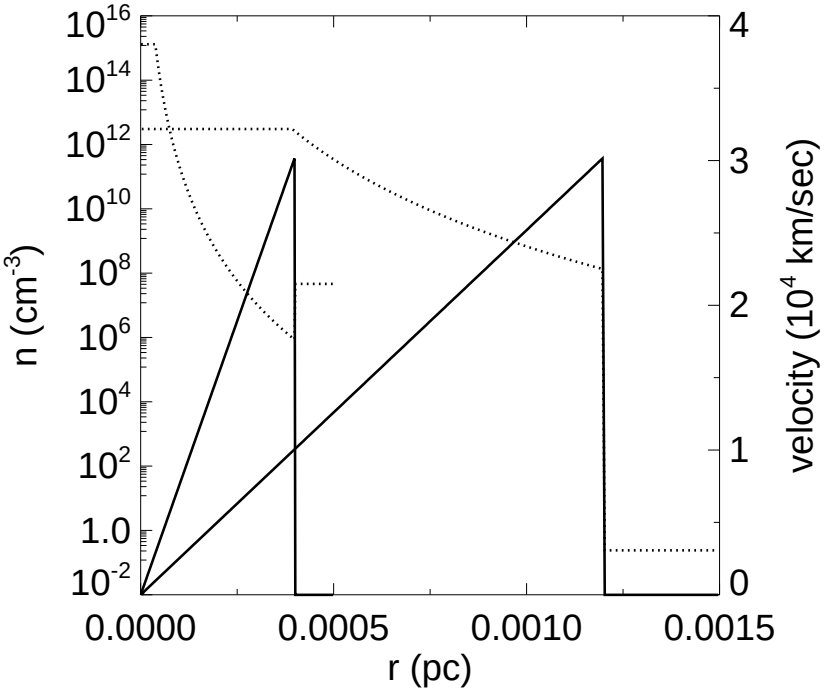

Figure 3.3: Density and velocity profiles of two free expansion blast profiles used in this study. Left: 15Ms_halo3; right: 40Ms_halo1. Dotted: number density; solid: velocity.

3.4.1 Supernovae in HII Regions

In Figures 3.4 and 3.5 we show four stages of a 260 $M_\odot$ pair-instability supernova in halo 1, which is completely ionized by the progenitor. We show in Figure 3.6 cumulative radiation losses together with kinetic energy for all nine models. The radiative processes tallied are H, He, and He^+ collisional excitation and ionization losses, bremsstrahlung, and IC scattering from the CMB.

$t <$ 10 yr: Initial Shock

Even though its surroundings are diffuse, n $\lesssim 0.1$ cm^3, the free expansion drives a shock into the HII region that heats immediately to over 10^{11} K, as shown in Figure 3.4c. The shocked gas is collisionally ionized and accelerates to 67000 km s^{-1}. This occurs because the abrupt drop in density at $r \sim 0.004$ pc in the initial blast profile generates a sharp pressure gradient when it is ionized, and hence isothermal. The gradient accelerates the small amount of gas lying within it to nearly three times its

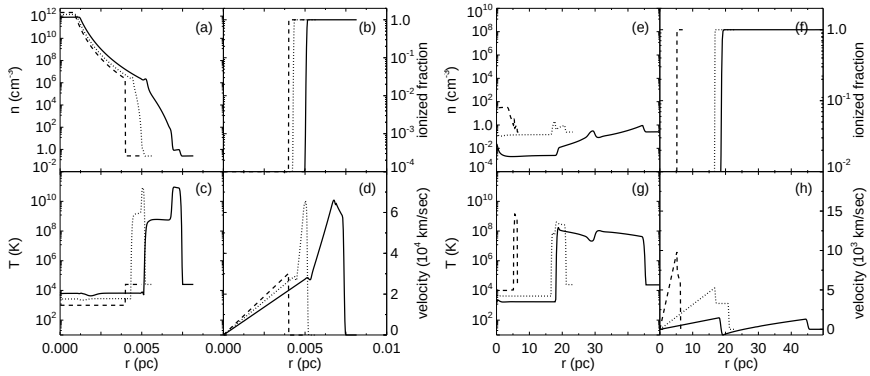

Figure 3.4: Early evolution of the 260 $M_\odot$ pair-instability supernova in halo 1. Panels (a) - (d): early free expansion. Dashed: t = 0; dotted: 2.9 days; solid: 14.5 days. Panels (e) - (h): end of the free expansion. Dashed: t = 515.6 yr; dotted: t = 3093 yr; solid: t = 6347 yr.

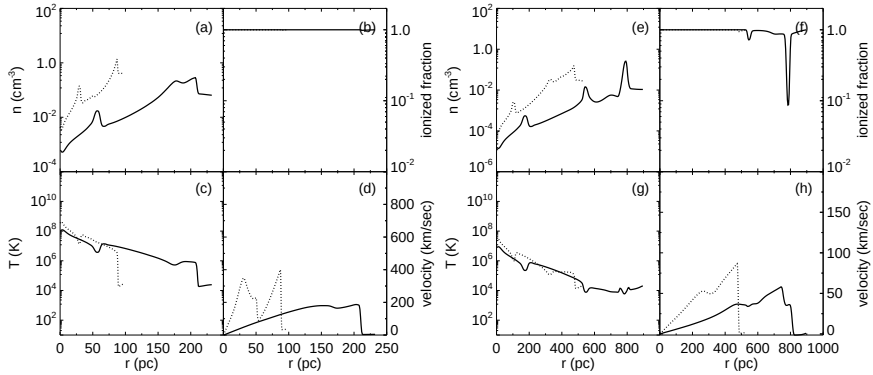

Figure 3.5: Later evolution of the 260 $M_\odot$ pair-instability supernova in halo 1. Panels (a) - (d): interaction of the 260 $M_\odot$ pair-instability remnant with the relic ionized core shock. Dotted: t = 19.8 kyr; solid: t = 420 kyr, respectively. Panels (e) - (h): flow profiles at 2.0 Myr (dotted) and 7.93 Myr (solid).

original velocity, driving a rarefaction wave backward into the denser gas behind that is visible in the velocity profile at $r \sim 0.0045$ pc at t = 2.9 days. The drop in velocity of the dense gas in this wave and the speedup at the edge of the expansion are insignificant compared to the blast energy, so the kinetic energy of the ejecta remains steady for $t < 700$ yr, as seen in the solid black plot in Figure 3.6g. The temperature of the ionized gas in the rarefaction wave falls from 10^{11} - 2 $\times 10^9$ K at 2.9 days and then to 7 $\times$ 10^8 K by 14.5 days in exchange for PdV work on its surroundings. We note that the density jump conditions for a strong shock are satisfied at $r \sim 0.0075$ pc at 14.5 days.

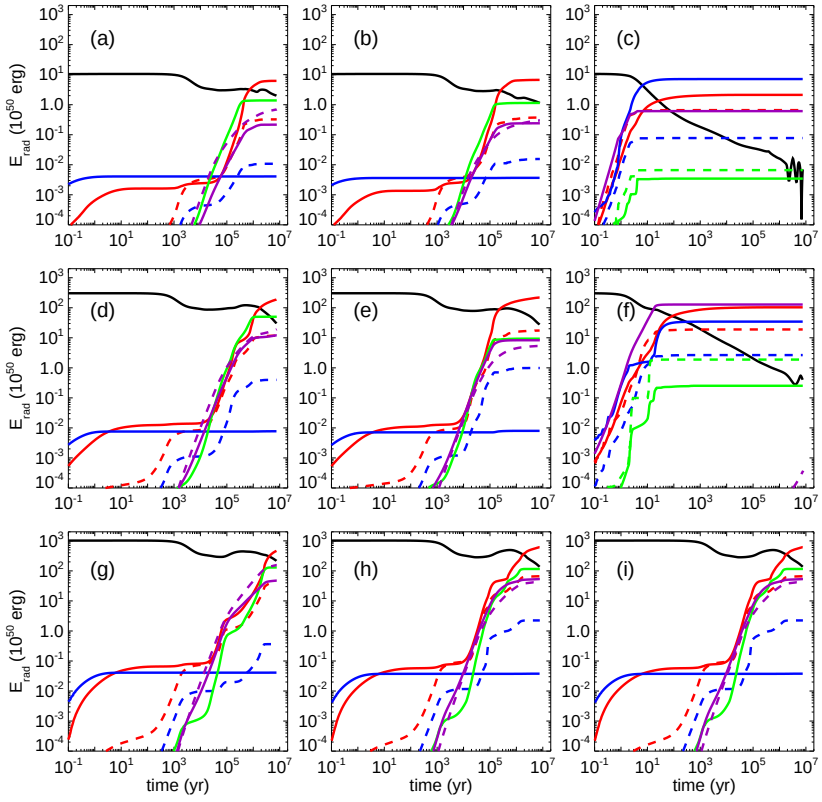

Figure 3.6: Radiative energy losses in all nine remnants *vs* time. Black solid: total kinetic energy; red solid: collisional excitation of H; red dashed: collisional ionization of H; blue solid: collisional excitation of He; blue dashed: collisional ionization of He; green solid: collisional excitation of He^+; green dashed: collisional ionization of He^+; purple solid: bremsstrahlung; purple dashed: inverse Compton scattering. Panels (a) - (c): 15 solar mass Type II SN in halo 1, halo 2, and halo 3, respectively. Panels (d) - (f): 40 solar mass hypernova in halo 1, halo 2, and halo 3, respectively. Panels (g) - (h): 260 solar mass pair-instability SN in halo 1, halo 2, and halo 3, respectively.

The early H and He excitational losses over $t < 10$ yr in Figure 3.6g are due to the ionization of forward edge of the ejecta. They are minute compared to the kinetic energy of the ejecta, which freely expands until it has swept up its own mass in the HII region at a radius of ~ 20 pc. The 'broken sawtooth' velocity profile at 2.9 and 14.5 days soon relaxes into a new free expansion with a peak velocity of 55000 km s^{-1}.

500 yr < t < 6350 yr: End of the Free Expansion

At 515.6 yr a homologous free expansion can still be seen in the density profile, which retains a flat central core and power-law dropoff. At this point its radius is only 7.5 pc and the blast has not yet accumulated its own mass in the relic HII region. By 3093 yr it grows to 21 pc and has swept up 260 $M_{\odot}$. This marks the end of the free expansion: the density profile flattens out and and a reverse shock forms at r = 16 pc. The reverse shock strengthens, backstepping through and completely ionizing the remnant as shown in Figures 3.4f and 3.4h. As this reverse shock propagates backward through the ejecta from 500 - 6000 yr in Figure 3.4e, collisional ionization losses in H and He rise over approximately the same interval of time in Figure 3.6g. Inverse Compton scattering with the cosmic microwave background (CMB) begins to remove energy from the hot, ionized interior of the blast after 1 kyr as it grows in volume. Compton losses reach 20% of the energy of the explosion in this run, raising the possibility of small scale fluctuations in the CMB that might be observable through the Sunyaev-Zel'dovich (SZ) effect. We examine this issue in greater detail in § 5.

In this era, the remnant is still well short of the dense shell, and has thus evolved in a uniform medium, as shown in the left panel of Figure 3.2, which shows the density profile of the HII region. Although not included in Figures 3.4 and 3.5 for brevity, reflected shocks traverse the interior of the remnant twice before it reaches the shell. They are less important to the dynamics of the remnant than the adiabatic expansion against the surrounding material, but as will be shown later, they never permit the flow to fully settle into an adiabatic Sedov-Taylor solution. By the time the remnant collides with the shell it has lost 70% of its kinetic energy.

19.8 kyr < t < 420 kyr: Collision with the Shell and the Radiative Phase

The 400 km s^{-1} shock overtakes the 25 km s^{-1} HII region shell at r = 85 pc at 59.5 kyr. Its impact is so strong that a second reverse shock forms and separates from the forward shock at 420 kyr. Both shocks are visible in the density and velocity profiles of Figure 3.5a at 175 and 210 pc. In reality, the interaction of the SN and shell is more gradual: the remnant encounters the tail of the shell at 60 pc at 19.8 kyr, at which time the greatest radiative losses begin, tapering off by 7 Myr with the formation of another reverse shock. Hydrogen Ly-α radiation dominates, followed by inverse Compton scattering, collisional excitation of He^+ and bremsstrahlung, but the remnant also collisionally ionizes H and He in the dense shell as evidenced by the sharp rise in ionization losses at 40 kyr. The rise in total kinetic energy at late times is due to the appearance of the dense shell of the HII region on the grid at 60 kyr, which cannot be separated from the remnant.

t > 2 Myr: Dispersal of the Halo

Hydrodynamical profiles of the remnant at 2 Myr and at 7.93 Myr, the time to which the simulation was run, appear in Figures 3.5e-h. Figure 3.6g reveals that H Ly-α radiation drains the kinetic energy of the remnant out to 7 Myr and that collisional ionization continues to 4 Myr, well after the remnant has struck the shell. These additional losses occur as the supernova overtakes a series of smaller subsidiary

shocks in the relic HII region visible just beyond the dense shell in the velocity profile of the left panel of Figure 3.2. One feature of these secondary collisions is the formation of a dense shell at 500 pc at 2 Myr that persists to 800 pc. The large recombination rates in this shell drop its ionization fraction to 0.08. Since densities elsewhere in the remnant are nearly 100 times smaller, this shell is likely the site of the H Ly-α losses for $t > 2$ Myr, which grow to 50% of the original energy of the blast.

The density plot at 7.93 Myr clearly shows that nearly all the baryons are ejected from the halo at velocities well in excess of the 2 - 3 km s^{-1} escape speed. The blast scours gas from inside the virial radius, to densities much lower than in the HII region: 10^{-4} cm^{-3} as opposed to 0.1 cm^{-3}. Only 10% of the energy of the blast survives radiative, gravitational, and adiabatic losses, but the momentum associated with this energy, together with strong relic ionized flows, still easily unbinds the gas from the halo. In these circumstances the dispersal of heavy elements into the surrounding intergalactic medium (IGM) is arrested when the remnant comes to pressure equilibrium with the relic ionized gas, typically at half the radius of the progenitor HII region (one or two kpc) (Greif et al. 2007).

Both Compton and free-free losses from the remnant decline after 3×10^7 yr, in general agreement with their respective cooling timescales at these densities, temperatures, and redshift (Kitayama & Yoshida 2005)

$$t_{\rm ff} \sim 10^7 \left(\frac{n_{\rm H}}{cm^{-3}}\right)^{-1} \left(\frac{T_{\rm e}}{10^7 K}\right)^{1/2} \text{yr}, \tag{3.21}$$

and

$$t_{\rm IC} \sim 7 \times 10^6 \left(\frac{1+z}{20}\right)^{-4} \text{yr}. \tag{3.22}$$

At 2 Myr, $n_{\rm H} \sim 0.1$ cm^{-3}, $T_{\rm e} \sim 10^5$ K, and $z \sim 20$, so $t_{\rm ff}$ and $t_{\rm IC} \sim 10^7$ yr.

The other six supernovae that explode in HII regions follow nearly identical evolutionary paths. Most of the initial blast energy goes into adiabatic expansion and then radiation upon impact with the ionized core shock in the fossil HII region from 10^4 - 10^5 yr. This timescale is set by the dynamics of the HII region: the core shock radii fall within a fairly narrow band set by the sound speed of the ionized gas, which is a weak function of temperature and varies little for the three types of progenitor. Radiative losses at these later times originate from both the remnant and the dense shell of the HII region. In all seven cases the SN destroys the halo: baryon densities interior to the virial radius fall below 10^{-4} cm^{-3}.

3.4.2 Blasts in Neutral Halos

We show in Figures 3.7 and 3.8 four stages of evolution for a 40 $M_\odot$ hypernova in halo 3, the most massive halo. The HII region is trapped so close to the star that the halo is essentially neutral and undisturbed when the star explodes.

$t < 1$ yr: Free-Expansion Driven Shock

As before, the leading edge of the expansion promptly heats to extremely high temperatures, this time to approximately 10^{10} K. This is somewhat less than in

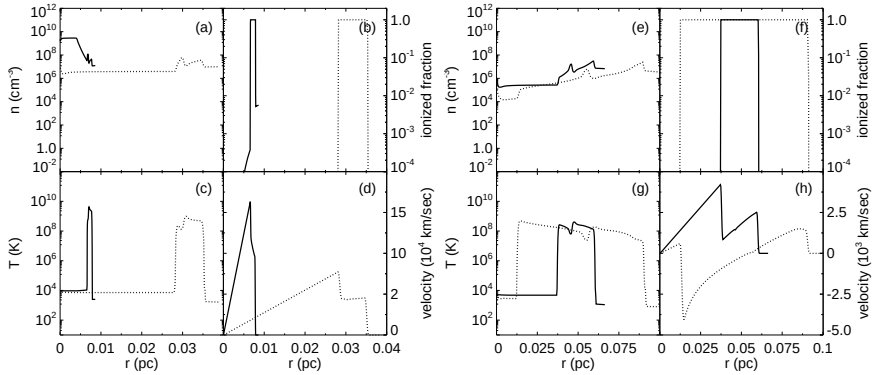

Figure 3.7: Early evolution of the 40 $M_\odot$ hypernova in halo 3. Panels (a) - (d): early free expansion. Solid: 0.301 yr; dashed: 3.01 yr. Panels (e) - (h): formation of the first reverse shock. Solid: 7.45 yr; dashed: 17.4 yr.

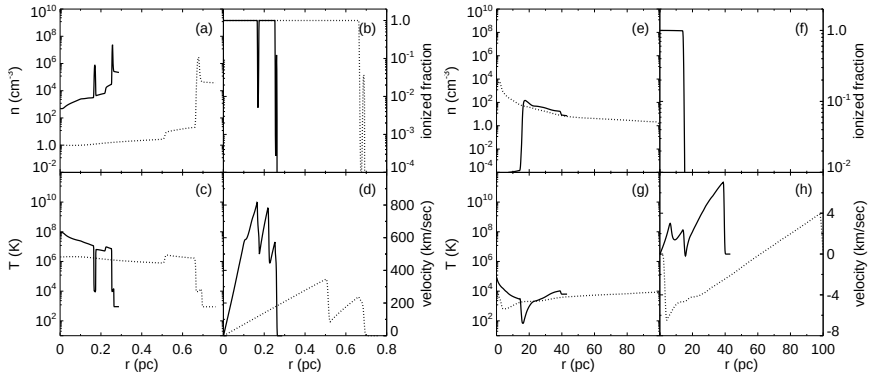

Figure 3.8: Later evolution of the 40 $M_\odot$ hypernova in halo 3. Panels (a) - (d): multiple strongly radiatively-cooling shocks. Solid: 214 yr; dotted: 1348 yr. Panels (e) - (f): fallback of the remnant to the center of the halo. Solid: 2.14 Myr; dotted: 6.82 Myr.

the PISN because of the inertia of the surrounding medium. Although the edge of the shock is again completely ionized, it fails to jet forward as before because the ambient densities are so large, 10^7 cm^{-3} instead of 0.1 cm^{-3}. The shock strongly radiates, primarily by bremsstrahlung and excitation of He, although the latter falls off rapidly as shown in Figure 3.6f. Unlike PISN in the HII region, this blast loses large amounts of energy at very early times, 3×10^{50} erg by 1 yr. At 0.301 yr the density profile is still mostly that of a homologous free expansion, but by 3.01 yr it has leveled out and a reverse shock can be seen in the velocity at 0.03 pc. At this radius the blast has swept up several times its own mass in the neutral halo. The abrupt rise in collisional excitation and ionization losses in He^+ at $t \sim 1$ yr

coincides with the breakthrough of the dense shell, at 0.03 pc in Figure 3.7a, by the reverse shock, which requires 10^{50} erg.

$t <$ 20 yr: Early Radiative Phase

The second jump in He^+ excitation and ionization cooling at 20 yr in Figure 3.6 occurs when the reverse shock sweeps through and completely ionizes the dense interior of the fireball. From t = 2 - 20 yr, both adiabatic expansion and radiation drain two thirds of the internal energy from the blast in roughly equal proportions. At 7.45 yr the remnant exhibits a forward and reverse shock separated by a contact discontinuity (Fig. 3.7e). Bremmstrahlung losses level out after 20 yr because over the previous 10 yr the density of the shocked gas falls by a factor of 5 and cools below 10^8 K. This is again consistent with the free-free cooling time predicted by eq 3.21 for $n_{\rm H} \sim 2 \times 10^6$ cm^{-3} and $T_{\rm e} \sim 3 \times 10^9$ K at 0.3 yr.

100 $< t <$ 5000 yr: Late Radiative Phase

The inertia of the neutral halo rapidly slows the blast, allowing time for a series of reflecting shocks to reverberate between the edge of the blast and the center of the interior. Reverse shocks continue to break off from the leading shock as it plows up more of the neutral halo and is overtaken by reflected shocks emerging from the interior. Flow profiles of this process are shown in Figures 3.8a-d. At 214 yr a new reverse shock in the density profile at 0.25 pc is about to break away from the forward shock as a reflected shock approaches it from behind. At 1350 yr these two structures merge with another reverse shock about to depart toward the origin.

These crossing shocks form dense shells that rapidly recombine and become mostly neutral. The shells are luminous sources of H Ly-α emission, which cools them to 10000 K amidst the otherwise fully ionized and very hot gas. They are the sites of the H Ly α losses from the remnant from 50 to 5000 yr in Figure 3.6f that eventually amount to a third of the energy of the blast. In this period the kinetic energy of the remnant falls to 0.5% of the energy of the SN but at 5000 yr and 1.5 pc it still has sufficient momentum to expand.

Fallback

We show in Figures 3.8e-h the remnant at 2 Myr and 7.93 Myr. At 2 Myr the remnant has devolved into a slow dense shell of warm neutral gas extending from 15 to 40 pc and surrounding a hot, ionized diffuse ($\lesssim 10^{-4}$ cm^{-3}) interior. The inner surface of the shell soon falls back into the dark matter potential as shown at 7.93 Myr in 3.8e. The outer region of the shell ripples outward but at velocities well below that required for escape from the halo. By now the gas is fully neutral.

In contrast to blast models that 'fizzle' when initialized by thermal energy in massive neutral halos (Kitayama & Yoshida 2005), the free expansion in our model delivers enough impulse to the halo to seriously disrupt it out to 40 pc, even though the remnant retains less than 1% of the energy of the blast by 2 Myr. Although the baryons remain bound to the halo, the ejecta heavily enriches them with metals prior to fallback, radically altering their cooling and fragmentation timescales. We find that the baryons can rebound from the center more than once after their initial

recollapse into the halo, with large, episodic infall rates onto the central black hole. This may constitute a mechanism for the rapid growth of supermassive black hole seeds at high redshift. The explosion and its metals remain completely confined to the halo, unable to enrich the early IGM.

As another example of fallback in a trapped explosion, the evolution of the 15 $M_\odot$ supernova in halo 3 is qualitatively similar to that of the hypernovae, but with a few differences. First, the free expansion slows more quickly because it has less energy. The reverse shock at first fails to fully detach from the forward shock and instead forms a dense shell that emits extremely intense He lines. By approximately 1.1 yr this radiation slows the forward shock, cooling it suddenly from 1×10^8 to 10^4 K in just 3.5 yr, extinguishing bremsstrahlung x-rays at 6 yr and terminating all other radiative losses by $t \sim 20$ yr. Afterwards, the blast loses kinetic energy only to adiabatic expansion and gravity. The reverse shock is too weak to ionize the interior, and the reverberations back to the forward shock are too faint to form shells. The SN therefore remains mostly neutral. Gravity arrests its expansion at 2.5 pc at 1.35×10^5 yr, and it falls back to the center of the halo. Helium lines from the semi-detached reverse shock shell dominate the radiation from this remnant, emitting 75% of the energy of the blast.

We show central infall rates associated with the fallback of the 15 and 40 $M_\odot$ remnants in halo 3 from 10^6 yr to 2×10^7 yr in Figure 3.9. Infall occurs later in the more massive remnant because its greater explosion energy carries it farther from the center of the halo. There are three fallback phases in the 15 $M_\odot$ remnant over this time interval ranging from 10^{-3} - 10^{-2} $M_\odot$ yr^{-1} in magnitude and from 1 - 2 Myr in duration. The three episodes are punctuated by rebound from the core of the halo, which is not shown in the figure. The first infall phase of the 40 $M_\odot$ remnant manifests rates of 3.5×10^{-2} $M_\odot$ yr^{-1} and lasts 1.5 Myr. These are not the only occurrences of fallback; our numerical models indicate several more will occur in less than a merger time. In addition to fueling rapid growth of a black hole, these episodes will thoroughly mix metals from the ejecta in the central regions of high density in the halo because the leading shocks are subject to dynamical instabilities during both rebound and collapse. However, we point out that fallback of the remnant to the center of the halo is distinct from accretion onto the black hole, whose rates are governed by angular momentum and radiation transport away from the central object. Future radiation hydrodynamical simulations will determine the rates with which the black hole grows in mass.

Intense bursts of x-rays from the central black hole will likely accompany these periods of heavy accretion, ionizing and heating gas within the halo and perhaps driving strong H_2 formation. It is generally held that the broad I-fronts of black holes and quasars exert positive feedback on structure formation because H_2 formation is promoted in their partially ionized outer layers (e. g. Ricotti et al. 2001). However, this picture is complicated by the fact that the accretion shock might radiate strongly in UV, including the LW bands, which would suppress H_2 formation. Furthermore, recent work on the structure of quasar ionization fronts indicates that they are preceded by a 'T-front', or temperature front (Qiu et al. 2008). This is a layer of 10^4 K minimally-ionized gas formed beyond the broadened I-front of black holes and quasars by the few most energetic photons. These photons cause secondary ionizations in the pre-front gas that heat it but cannot sustain a large

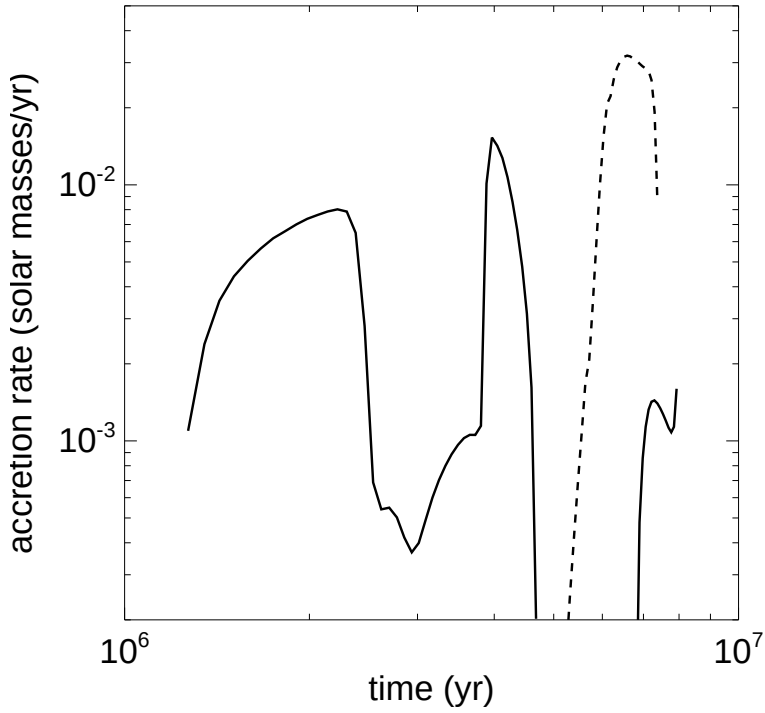

Figure 3.9: Infall rates $4\pi\rho(r)v(r)r^2$ associated with fallback of the 15 and 40 $M_\odot$ remnants in halo 3. Solid: 15 $M_\odot$; dashed: 40 $M_\odot$

ionization fraction. The preheated gas might pre-empt H_2 formation that would otherwise occur when the outer layers of the I-front reaches it. Detailed numerical simulations will be required to resolve the thermal and chemical evolution of the gas in the vicinity of the seed black holes at the centers of large halos at high redshifts.

The importance of including the dark matter gravitational potential in primordial SN models is particularly clear in trapped explosions. We performed experiments in which we set the halo in hydrostatic equilibrium and then evolved the blast without force updates by the dark matter potential. In these tests, the remnant simply continues expanding and there is no fallback. This provides a good check of the gravitational physics on the expanding grid and attests to the necessity of including dark matter in the calculation.

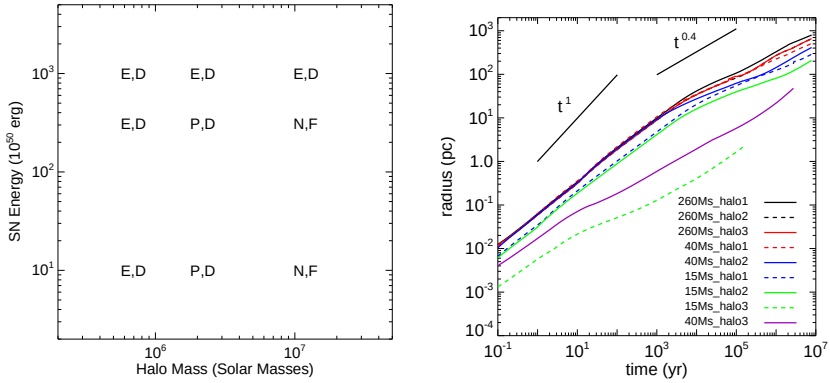

Figure 3.10: Left: eventual fate of a halo given the indicated explosion energy. The first letter refers to the final state of the halo prior to the explosion; E: photoevaporated; P: partly ionized, defined as the I-front not reaching the virial radius; N: neutral, or a failed HII region. The second letter indicates outcome of the explosion; D: destroyed, or F: fallback. Right: shock position *vs* time for the nine supernova remnants.

3.4.3 Halo Destruction Efficiency

We summarize the results of our explosion models in the left panel of Figure 3.10. Halos less massive than $2.1 \times 10^6\ M_\odot$ are destroyed by Population III stars as small as 15 $M_\odot$ (we reiterate that destruction of the halo refers to expulsion of its gas, not its dark matter). On the other hand, PISN disperse much larger halos, even the first that could cool by atomic lines ($\sim 1.0 \times 10^7\ M_\odot$). This in part is because the star preionizes the halo. Indeed, even lower-mass primordial stars finally eject more than 90% of the baryons from halos $\lesssim 10^7\ M_\odot$ because their HII regions impart considerable momentum to the baryons prior to the explosion that facilitates breakout of the remnant into the IGM.

In failed HII regions, enough momentum from even modest explosions, 10^{51} erg and 3×10^{52} erg, survives the enormous prompt radiative losses to disrupt halos out to a significant fraction of their virial radii. Nevertheless, we find that Type II supernovae and hypernovae are contained by halos more massive than 1.0×10^7 $M_\odot$, but will destroy less massive halos that cool mainly by molecular hydrogen. Recall that many primordial stars never explode: those lying between 50 and 100 $M_\odot$ and above 260 $M_\odot$ are not thought to exhibit any kind catastrophic mass loss (Heger & Woosley 2002). In these circumstances the halos are instead photoevaporated, with the loss of $\sim$ 50% of the gas rather than 95%, as expected for a SN. Although not all gas exits these halos, no subsequent star formation would follow for at least a merger time.

3.4.4 Comparison to the Canonical Phases of Idealized Remnants

In the classic problem of a supernova blast in a uniform medium, idealized remnants evolve in four distinct phases: the free expansion, the Sedov-Taylor (ST) phase, the pressure driven snowplow (PDS), and the momentum conserving snowplow (MCS). Each stage can be loosely associated with a power law for the position of the shock as a function of time: $R_S \propto t^\eta$. In the very early free expansion the flow is completely dominated by the momentum of each fluid element and this exponent is 1. Somewhat later in the free expansion phase the exponent tends to $\frac{n-3}{n-s}$, where where n and s are the density indices of the supernova ejecta and the ambient medium, respectively Chevalier (1982). When the blast has swept up many times its own mass it consists of a self-similar adiabatic hot interior and non-radiative shock: the ST phase (Sedov 1959, Taylor 1950) in which $\eta_{ST} = 2/5$. As the remnant grows, the shock begins to be driven by the pressure of its hot, now nearly isobaric interior in addition to its own momentum because the postshock fluid velocity approaches that of the shock (Cox 1972, Chevalier 1974). At about the same time, if the shocked gas can cool by radiation it collapses into a thin dense shell that accrues material as it 'snowplows' the interstellar medium (ISM). If the interior cannot radiatively cool in this pressure-driven snowplow (PDS) era its shock evolves according to $\eta_{PDS} = 2/7$ (McKee & Ostriker 1977). Finally, if the interior loses energy both to PdV work and radiation, the remnant becomes a momentum conserving snowplow (MCS) whose analytical solution yields $R_S \propto t^{1/4}$ (Oort 1951). The shell halts when it comes into pressure equilibrium with the ISM, after which it disperses and becomes indistinguishable from its surroundings.

We show in the right panel of Figure 3.10 shock position as a function of time for all nine remnants. All clearly exhibit an $\eta \sim 1$ expansion at early times but depart from the canonical stages of ideal remnants in uniform media thereafter. This is not surprising for several reasons. When the reverse shock breaks away from the contact discontinuity at the end of the free expansion, it reverberates back and forth across the interior, heating it and never allowing it to relax to an ST phase, even though the leading shock does not radiate. This is likely why $\eta < 2/5$ after the free expansion. When the remnant later mingles with the baryons that have been swept up into the HII region shock, it becomes strongly radiating without the formation of a thin shell. The curves taper somewhat more as the shock deaccelerates upon encountering the shell, as seen from 10^4 to 10^5 yr. The remnant cannot be disentangled from the strong fossil ionized flows thereafter.

On the other hand, supernovae in the dense cores of neutral halos depart from the standard behavior of ideal remnants in uniform densities because the cores are so stratified (with baryon densities falling by $r^{-2.2}$), and because they radiate strongly from very early times. As a result, the free expansion ends in less than a year, and shocks reverberate through interior of the remnant even more frequently than in HII regions due to the inertia of the surrounding gas, again preventing the ST phase from materializing. Two stages of radiative loss without the formation of thin shells in the metal-free shocked gas then follow. Through all three stages adiabatic expansion also slows the remnant, with eventual fallback into the halo. Note that the plots in Figure 3.10 trace the position of the leading velocity front

in the gas, which can continue outward into the halo even if the bulk of the remnant, which does not have a precise location, falls back toward the center. In short, we find that primordial supernovae do not conform to the usual paradigm for ideal remnants in uniform media.

Note from these profiles that the shock experiences brief periods of acceleration in neutral halos and may therefore be susceptible to Rayleigh-Taylor instabilities in three dimensions. Furthermore, the contact discontinuities separating forward and reverse shocks would also be prone to instabilities and breakup in multidimensional simulations (McKee & Ostriker 1977).

3.5 Observational Signatures of Primordial Supernovae

One trend that is immediately apparent in all nine remnants in Figure 3.6 is that adiabatic expansion losses precede radiative losses in blasts evolving in HII regions but are coincident in neutral halos. Another is that bremsstrahlung dominates energy losses in explosions in neutral halos but amounts to at most a few percent in HII regions. Inverse Compton scattering is greatest in the most powerful explosions in HII regions but virtually nonexistent in neutral halos, where the fireball cools before it can enclose large volumes of the CMB. In HII regions, H Ly-α finally dominates radiative losses from primordial remnants, with singly-ionized He excitation next in importance. Neutral He emission rivals or exceeds H Ly-α in less energetic blasts in neutral halos because He is not completely ionized. We plot luminosities due to excitation of H and He along with bremsstrahlung and IC for all nine remnants in Figure 3.11.

3.5.1 Luminosities in HII Regions

Type II supernovae and hypernovae in HII regions emit three flashes of Ly-α lines: the prompt flash when the free expansion forms a shock with its surroundings, a second flash as the reverse shock breaks free of the forward shock and ionizes the interior, and a final flash when the remnant collides with the dense HII region shell. Peak luminosities in the second and third flashes scale approximately with explosion yield: 10^{38} erg s^{-1} for the Type II supernova and 10^{39} erg s^{-1} for the hypernova and PISN. The third flash in more powerful explosions has twin peaks due to collisions with the smaller subsidiary shocks that lie just beyond the dense shell in the HII regions of more massive progenitors, as discussed in section 3.4.1. The contributions to each flash by H and He$^+$ are in proportion to their abundances. Because He is always singly ionized at later times it is absent in the second and third flashes. The second flash is consistently two orders of magnitude less intense than the third flash because the mass of the remnant is much lower than that of the dense shell and remnant combined.

It has been suggested that Ly-α photons from Population III stars are scattered by H in the early IGM, coupling its spin temperature to its kinetic temperature without heating the gas (Chen & Miralda-Escudé 2004). If the scattering region is not first heated by hard photons, the spin temperature would rapidly fall to the

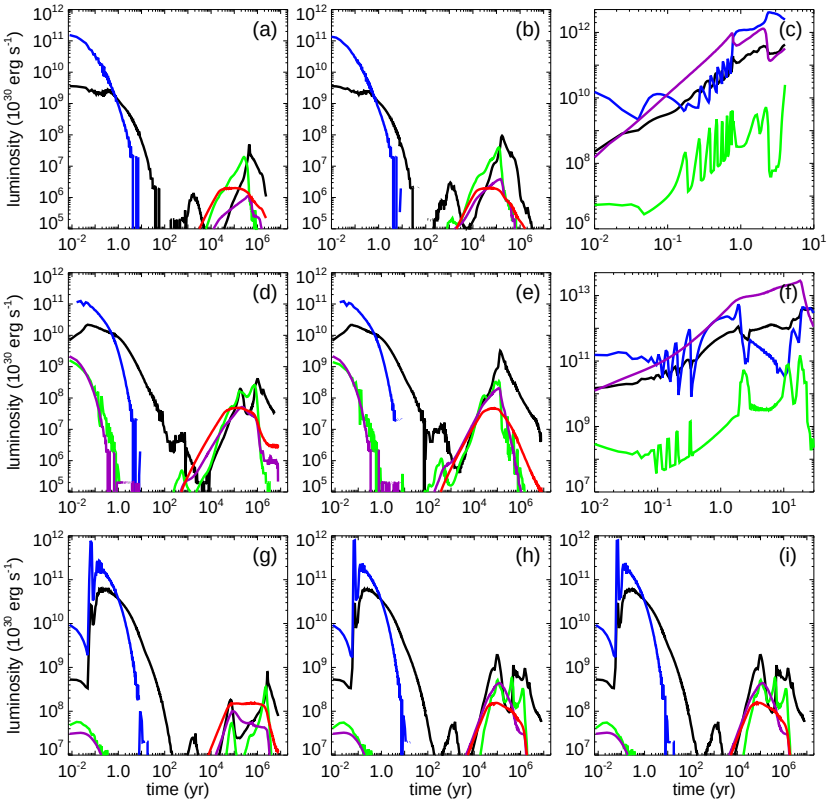

Figure 3.11: Luminosities of all nine primordial SN remnants *vs* time. Black: collisional excitation of H; blue: collisional excitation of He; green: collisional excitation of He^+; purple: x-rays (bremsstrahlung); red: energy deposition rates into the CMB due to inverse Compton scattering. Panels (a) - (c): 15 solar mass Type II SN in halo 1, halo 2, and halo 3, respectively. Panels (d) - (f): 40 solar mass hypernova in halo 1, halo 2, and halo 3, respectively. Panels (g) - (h): 260 solar mass pair-instability SN in halo 1, halo 2, and halo 3, respectively. Note the different energy and time scales in panels (c) and (f), which describe the trapped explosions. As discussed in the text, the H and He line luminosities in the first pulse in H II region explosions should really be considered free-free losses.

low kinetic temperature of the gas and the region would appear in absorption in 21 cm against the CMB. If more energetic photons later heat the scattering volume it would then appear in emission against the CMB, creating a brief absorption signal followed by a weak emission signal that is unique to Population III stars. Our findings indicate that the same may be true of the supernova remnant but in reverse: x-rays from the collision of the remnant and the dense shell die out before the Ly-α pulse, resulting in a strong 21 cm absorption signal preceded by weak emission against the CMB. Given that the lifetime of the main flash can exceed that of the star and that the scattering region can span several kpc proper, it may be possible

to resolve them with the next generation of 21 cm observatories such as the *Square Kilometer Array* (*SKA*).

Although the Ly-α intensity of the first flash is at least a hundred times greater than in the next two, the actual energy released is minute due to its transience and is of little importance to the evolution of the free expansion. The large fluxes are in part numerical; they are emitted from the extremely large densities at the interface of the shock and the free expansion, which are not spatially resolved by the mesh. Artificial viscosity smears the enormous jump in density there over several zones, over which the temperature rises from a few thousand to several billion K. In one of the zones the temperature crosses the threshold for H and He line emission, activating these cooling channels for the entire zone when in reality they originate from only an extremely thin shock layer that is a tiny fraction of the width of the zone. The Ly-α luminosity is thus overestimated by a factor roughly equal to the ratio of the widths of the zone and the shock; it is probably several orders of magnitude lower than free-free emission for $t < 10$ yr. Little inaccuracy is introduced to the energetics of the ejecta by this artifact, not only because the energies involved are small. If excitational cooling of H and He are deactivated in this phase the shock simply remains hotter, with elevated free-free emission rates that are nearly identical to the total rates when excitational cooling is included. Thus, nearly all the radiation in this era is really in x-rays, with peak luminosities of 10^{41} erg s^{-1}. Because the energy liberated is less than a millionth of the blast energy it does not appear in Figure 3.6. All three types of supernovae have similar luminosity profiles in HII regions in this era because the ejecta was assumed to have the same initial velocity profiles. Note that the energy of the first pulse, which is from the interaction of the shock and ambient HII region, does not include the energy of radioactive decay in the ejecta, which is expected to be similar to that observed in SN today, $\sim 10^{42}$ erg s^{-1}.

Hypernovae and PISN in HII regions emit a second x-ray flash during the collision with the dense shell. In contrast to the prompt flash, the second burst is longer, $\sim 10^6$ yr with luminosities of 10^{38} erg s^{-1}. Type II supernovae emit only the second flash, with emission rates that are lower by two orders of magnitude. The durations of the second x-ray pulse and the inverse Comptonization of the CMB are again in agreement with the free-free and IC cooling times of eqs 3.21 and 3.22 for densities of 0.1 cm^{-3} and temperatures of 10^7 K at 1 Myr. Although primordial supernovae were the first x-ray sources in the early universe they probably did not contribute to cosmological reionization (Tegmark et al. 1993). After examining early reionization by x-rays released by primeval supernovae, Kitayama & Yoshida (2005) concluded that unrealistically large explosion rates are required to create significant x-ray backgrounds at high redshift. However, prompt x-rays from blasts completely contained within neutral halos, although not visible to external observers, may drive strong H_2 formation that enhances the cooling and collapse of gas in the halos.

As noted earlier, Figures 3.6 and 3.11 show that cooling via inverse Compton scattering of cosmic microwave background photons contributes strongly to the loss of kinetic energy in supernova remnants evolving in HII regions. In some cases, such as the one shown in Figure 3.6, it is more than 10% of the overall energy loss, but more generally only a few percent of the supernova's kinetic energy is

deposited into the CMB. The strength of this cooling component is due to the high energy density of the CMB at the redshifts of these SN, and has been predicted by previous work (Tegmark et al. 1993, Voit 1996, Madau et al. 2001). One result will be a distortion of the CMB due to the Sunyaev-Zel'dovich effect, predicted to be on the order of $\delta y \sim \text{few} \times 10^{-6}$ (Oh et al. 2003). The angular size of a given HII region and supernova remnant at $z \sim 20$ is quite small, however – on the order of 100 kpc (comoving), which corresponds to an angular size of a few arc seconds. While individual Pop III supernovae would be essentially impossible to detect in the SZ with current telescopes, clusters of supernovae would create spectra distortions with a power spectrum that can be predicted by making assumptions about clustering bias. We have examined the assumptions made by Oh et al. (2003), and our results for radiative losses due to inverse Compton scattering are generally much lower than their predictions of 30-100% of the supernova kinetic energy, suggesting that their results would be an upper bound on the contribution of Population III supernovae to the SZ effect. Indeed, recent work by O'Shea & Norman (2008) suggests that the vast majority of Population III stars will form in halos with virial temperatures below 10^4 K, with a contribution to the angular power spectrum somewhere between cases B and C of Oh et al. (shown in Figure 1 of their paper). This implies that contributions to the SZ effect from Population III SN would be negligible in comparison to that from galaxy clusters, making them extremely difficult to detect.

3.5.2 Radiation from Neutral Halos

Table 3.6: Mass of Enriched Baryons

halo	Type II SN	Hypernova	PISN
1	8.59E+5 $M_\odot$	1.75E+6 $M_\odot$	5.35E+6 $M_\odot$
2	4.35E+5 $M_\odot$	1.61E+6 $M_\odot$	3.38E+6 $M_\odot$
3	8.84E+4 $M_\odot$	1.61E+5 $M_\odot$	3.38E+6 $M_\odot$

Luminosity profiles for blasts in neutral halos exhibit a single peak lasting from 2 - 20 yr that is dominated by free-free and He line emission. The duration and peak intensity both scale with explosion energy: 2 yr and 4×10^{42} erg s^{-1} for the Type II SN and 20 yr and 2×10^{43} erg s^{-1} for the hypernova. Approximately 75% percent of the blast energy is lost in this one burst of radiation, which emanates from a volume less than 0.1 pc in radius. Again, these luminosities originate from the shock and not the radioactive decay of the ejecta. The luminosity of the shock in the Type II SN is comparable to that due to decay in sn today.

Line emission from the 15 $M_\odot$ and 40 $M_\odot$ SNR in halo 3 exhibits rapid oscillations in the first year on periods of a few days. This interesting phenomenon is due to the reverse shock that is attempting to break free of the contact discontinuity. Just as it does so, its densities and temperatures rise, with a sharp increase in line emission which then cools the shock. Losing pressure support, the reverse shock retreats toward the contact discontinuity in the frame of the flow until gas from the interior again builds at the interface and causes the shock to break free, beginning the cycle once more. Oscillations in standing radiative shocks are well understood

in a variety of astrophysical contexts (Chevalier & Imamura 1982, Imamura et al. 1984, Anninos et al. 1997). The amplitudes of these variations in our luminosity profiles clearly demonstrate the reverse shock to be the origin of almost all the atomic lines for $t < 1$ yr. Although not shown for brevity, oscillations are also present in the ionization cooling rates, again revealing the reverse shock to be their origin. Corresponding variations in the x-rays are absent because they originate from the shocked gas on the other side of the contact discontinuity.

Because the fireball cools fairly deep inside the halo, few of its x-rays are likely to escape into the IGM. In ambient densities of 10^7 cm^{-3}, the mean free paths of 100 eV and 1 keV photons are 1.7×10^{-7} and 3×10^{-4} pc, respectively, so they would downscatter in energy many times before exiting the halo. It is possible that the x-ray photons would promote the formation of molecular hydrogen in the suppressed remnant, but this would be transient and only operate at intermediate radii. The resultant cooling would be much less important than the metal-line cooling near the center of the halo. As shown in Figure 3.11, confined explosions deposit little energy into the CMB because they cool before enclosing an appreciable volume of background photons. The visibility of atomic lines from deep inside the halo is also open to debate since the densities in the explosion envelope would cause many resonant scatterings for each photon. The photons may downscatter to radio wavelengths, as observed in hypercompact HII regions deep within molecular cloud cores (Churchwell 2002, Rodríguez 2005). Detailed calculations of Ly-α radiative transfer are necessary to evaluate the 21 cm footprint of these explosions.

3.5.3 Optical/IR Light Curves

Table 3.7: Average Metallicity of Enriched Baryons

halo	Type II SN	Hypernova	PISN
1	6.87E-3 $Z_\odot$	1.16E-2 $Z_\odot$	2.32E-2 $Z_\odot$
2	1.36E-2 $Z_\odot$	1.26E-2 $Z_\odot$	3.68E-2 $Z_\odot$
3	6.68E-2 $Z_\odot$	1.26E-3 $Z_\odot$	3.68E-2 $Z_\odot$

In our discussion we have neglected the optical/IR flash due to the radioactive decay of the ejecta, which would compete with the early radiation flash from the shock in both HII regions and neutral halos. Since nucleosynthetic yields are not well determined for these primordial events, we compare the peak optical luminosities of supernovae in the local universe to the first x-ray peaks in our simulations. First, it is worthwhile to note that at early times the ejecta is optically thick to its own decay photons, which diffuse out through the envelope. If we adopt the simple argument that the optical/IR flash reaches its peak when the radiation diffusion timescale through the envelope is equal to the age of the remnant, we find that (Arnett 1982, Pinto & Eastman 2001)

$$t_{\rm peak} = \left(\frac{\kappa M_{\rm ej}}{7 c v_{\rm ej}}\right)^{\frac{1}{2}}, \tag{3.23}$$

where M_{ej} and v_{ej} are the ejecta mass and peak velocity, respectively. Commonly used values of the opacity κ range from 0.1 - 0.4, depending on the inclusion of

heavier element lines in addition to Thomson scattering. Assuming ejecta masses of 13 - 50 $M_\odot$ and shock speeds of 25000 km s^{-1}, the light curves peak as early as 25 days and as late as 100 days, so they will compete with the early bremsstrahlung pulse.

Type Ia supernovae peak luminosities are clustered around 9.6×10^9 $L_\odot$ (e. g. Branch & Tammann 1992) but those of Type II supernovae vary from 0.4 - 4×10^9 $L_\odot$ (Tammann & Schroeder 1990). Maximum x-ray luminosities in our models fall between 2.6 - 7.8 $\times$ 10^7 $L_\odot$, hundreds of times lower than the optical/IR curves. However, the x-ray pulse lasts for 2 - 4 yr, approximately ten times longer than the decay flash. We conclude that visible and IR radiation outshine the x-rays but that the x-rays outlive the optical glow. As discussed in the previous subsection, atomic cascades in neutral halos likely downscatter these photons to much lower energies.

3.6 Chemical Enrichment

We find the early emergence of a phase in which a forward and reverse shock are separated by a contact discontinuity in all our models to be a predictor of efficient metal mixing at small radii in both HII regions and in neutral halos. In three dimensions, the susceptibility of the contact discontinuity separating the reverse and forward shocks to breakup (Cioffi et al. 1988) suggests that mixing would be prompt in neutral halos and be well underway by 25 pc in HII regions. However, the forward and reverse shocks may also exhibit Rayleigh-Taylor instabilities. This would enhance mixing in the outer remnant and perhaps allow ambient gas to reach the center as the reverse shock propagates through the interior. This is in contrast to earlier work (Greif et al. 2007), whose numerical resolution could not address these phenomena.

How much gas is enriched by metals in these models, and to what levels? In HII regions that completely break out of the halo, the processes just described would enrich only half of the baryons originally interior to the virial radius of the halo, since the remainder are swept up into a dense shell 100 pc from the star. The degree to which the shell would be contaminated is yet to be determined, and is the focus of three-dimensional multiscale calculations now under development. Even more gas will be enriched as the shell and remnant expand together and then stall, typically at half the final radius of the HII region. In cases where the HII region exits the halo, we estimate the mass and metallicity of the enriched gas by assuming the SN ejecta is uniformly mixed with all the baryons interior to the stall radius. If the I-front ionizes only part of the halo, we approximate the final radius of the remnant from its deceleration beyond the virial radius and assume the ejecta to mix with all the gas inside this region. Finally, in neutral halos disrupted by the blast we consider the gas displaced by the remnant prior to fallback to be well mixed, which will be true after repeated episodes of infall and rebound in the dark matter potential. Estimates of the mass and metallicity of enriched gas in each model are tabulated in Tables 3.6 and 3.7.

Explosions in both HII regions and neutral halos enrich 10^5 to 5×10^6 $M_\odot$ of gas with metallicities ranging from 7×10^{-3} to 7×10^{-2} $Z_\odot$. This is well above

the critical metallicity believed to result in a rollover from high-mass to low-mass star formation in the early universe (Bromm et al. 2001, Mackey et al. 2003, Smith & Sigurdsson 2007). There are two modes of chemical enrichment in our models. Metals are either propagated far into the IGM, not returning to the halo in less than a merger time, which is $\sim$ 20 Myr at this epoch, or are confined deep within the parent halo. As Greif et al. (2007) point out, when metals escape into the IGM they preferentially migrate into voids of low density and do not influence star formation until they either recollapse into the halo or merge with a different one. However, the remnant itself could also be prone to breakup and clumping after colliding with the HII region shell, possibly triggering a second prompt generation of star formation in the enriched gas. These stars would reside in the outer regions of the halo, at radii of 100 - 200 pc. The implications of this novel mechanism for global star formation at high redshifts remain to be investigated with three-dimensional models that include metal line cooling. Type II and pair instability supernovae would imprint very different nucleosynthetic signatures on their descendants, which is important to surveys of ultra and extremely metal-poor stars in the galactic halo.

Immediate low-mass star formation is probable when metals are confined to the halo, given the short cooling and free-fall times in gas at densities of 10^4 - 10^5 cm^{-3} and metallicities of 0.01 solar. Approximately 10^5 $M_\odot$ of baryons are enriched to these levels, and it is conceivable that this gas could cool and fracture into a swarm of less-massive and long-lived stars that are confined to radii of 10 - 20 pc by the dark matter potential of the halo. Star formation would be complicated by the presence of a central black hole with large x-ray luminosities fueled by fallback into the halo. Nonetheless, this scenario raises the intriguing possibility of globular cluster formation at high redshifts, various mechanisms for which have been studied in the past 40 years (Peebles & Dicke 1968, Peebles 1984, Kravtsov & Gnedin 2005).

3.7 Discussion and Conclusions

Primordial supernovae can be more damaging to cosmological minihalos than previous studies suggest when they are properly initialized with kinetic rather than thermal energy. This is primarily because the momentum of the ejecta cannot be radiated away, even when radiative cooling is highly efficient, as in partially ionized or neutral clouds. Even blasts that are trapped by massive halos severely disrupt them, mixing their interiors with metals and creating massive fallback onto any black hole that remains. Population III stars of lower mass that are capable of explosions (15 - 40 $M_\odot$) easily destroy halos $\lesssim 10^7$ $M_\odot$ but not more massive ones, in part because they cannot preionize them. On the other hand, primordial stars from 140 - 260 $M_\odot$ will destroy halos even more massive than 10^7 $M_\odot$ in pair instability supernova blasts. To a good approximation, any supernova will destroy any halo less massive than 10^7 $M_\odot$ when photoevaporation of the halo prior to the blast is taken into account.

Primordial supernovae evolve in one of two ways. Blasts in HII regions remain free expansions out to several pc and are decelerated first by adiabatic losses and then later by radiative losses. In addition to the light curve of the radioactive decay

of their ejecta, these remnants radiate strongly upon collision with the dense shell of the HII region, usually by 10^4 - 10^5 yr. While most of their luminosity is in atomic H and He lines, particularly powerful blasts in HII regions can channel up to 20% of their energy into the CMB. Explosions in ionized halos evacuate gas from their virial radii to densities below 10^{-4} cm^3. Our models are in qualitative agreement with earlier one-dimensional Lagrangian and three-dimensional smoothed particle hydrodynamics (SPH) calculations of Type II and pair instability SN in primordial HII regions. Our results are also consistent with early one-dimensional calculations of supernova blasts in uniform diffuse media (Chevalier 1974, Cioffi et al. 1988): they too manifest reverse shocks that separate from forward shocks at relatively small radii and exhibit multiple shock reflections throughout the interior.

On the other hand, blasts in nearly neutral halos promptly radiate most of their kinetic energy as x-rays but retain sufficient momentum for the ejecta to reach radii of 10 - 20 pc. These contained explosions leave little observational footprint but radically alter the evolution of gas within the halo, first by contamination with heavy elements and then by successive cycles of fallback and rebound. This is a departure from earlier supernovae models in neutral halos initialized with thermal rather than kinetic energy that is radiated away before launching any flow out into the halo. Again, in agreement with earlier work by Chevalier (1974) and Cioffi et al. (1988), we find that neither explosion pathway is well represented by the canonical phases of idealized remnants in uniform media (Sedov-Taylor, PDS, or MCS). In all cases inclusion of the dark matter potential is crucial; models would otherwise fail to capture fallback in trapped explosions or erroneously predict expansion of the remnant until it achieves pressure equilibrium with the IGM.

Primordial supernovae occurred in neutral halos only if the halo was $\gtrsim 10^7 M_\odot$ and the progenitor was not very massive. Given that stars normally form by H_2 cooling well before the halo reaches this mass, is it likely that such blasts ever happened? The answer is yes if one considers halos at slightly later redshifts in rising Lyman-Werner backgrounds, whose effect is to postpone star formation in halos until they reach larger masses and become self-shielded to photodissociating photons (Machacek et al. 2001, O'Shea & Norman 2008, Wise & Abel 2007). Numerical surveys indicate that when stars form in more massive halos whose virial temperatures approach the threshold for atomic line cooling, they still do so by molecular hydrogen cooling and are subject to the range in masses examined in this paper (O'Shea & Norman 2007). It is probable that explosions and fallback in more massive halos were more common at somewhat lower redshifts (15 - 20) than those of the very first stars. We also point out that there are a greater range of spin parameters for star-forming halos than are sampled in current studies. Halos with higher angular momenta exhibit markedly lower central infall rates (O'Shea et al. 2005) that lead to much less massive stars. Finally, since the processes that halt accretion onto primordial stars remains poorly understood, low-mass supernovae in relatively massive halos cannot be ruled out.

The recent discovery of the first potential pair instability supernova ever observed (Smith et al. 2007) lends hope that this sort of explosion may have occurred in the high redshift universe. Population III PISN might be seen at moderate redshift ($z \sim 6$) with current technology (Scannapieco et al. 2005), or out to significantly higher redshift with the *James Webb Space Telescope* (Weinmann & Lilly

2005). Scannapieco et al. use the KEPLER code to create mock supernova light curves and demonstrate that the typical luminosities of pair instability supernovae are not much brighter than standard Type Ia supernovae. However, they remain brighter for much longer periods of time and have distinctive spectral features, making them easy to discriminate from standard Type Ia or Type II supernovae. Unfortunately, time dilation may make the light curves of extremely high redshift supernovae difficult to detect, especially those powered by the pair instability, since they have long evolutionary times in the rest frame. Their observation would require very different survey strategies than those employed in low redshift supernova searches. Furthermore, the predicted Population III supernova rate varies widely depending on a range of basic assumptions (Weinmann & Lilly 2005, Wise & Abel 2005, Mesinger et al. 2006).

If Population III supernovae are ever observed, they may be useful probes of their immediate environments. Peculiar features in a supernova light curve can be exploited to infer the properties of circumstellar gas (Smith & McCray 2007). If Population III stars are rapidly rotating, they may explode as gamma ray bursts (Bromm & Loeb 2006) and could be used to probe the interstellar medium of the halos in which they form, as has been done in the $z < 4$ universe (Chen et al. 2005, Prochaska et al. 2006, 2007).

The ionization front of the progenitor itself would also be prone to violent dynamical instabilities in three dimensions due to H_2 cooling, forming gas clumps in the relic HII region with which the blast would interact (Whalen & Norman 2008b,a). They would be most prominent in HII regions trapped in massive halos, partly because D-type fronts better shield H_2 from Lyman-Werner photons from the star and partly because R-type I-fronts that break free of halos would tend to photoevaporate any clumps that may have formed, although numerical simulations indicate that some would survive (Whalen & Norman 2008b,a). I-front instabilities may also drive turbulence in the surrounding medium. Both fragmentation and turbulence will enhance the mixing of metals in halos and should be included for self-consistency in future three dimensional models.

Molecular hydrogen and HD could also cause the remnant to cool and fragment, a process not addressed in these models. Explosions in ionized halos would sweep up H_2 and HD that are rapidly forming in the relic HII region. However, molecular cooling would not occur until late times in our models because the remnant remains fully ionized and hot for several Myr, as shown in Figure 3.5f. At 7.93 Myr, H_2 might form in the forward shock as it partially recombines and cools to 10000 K, forming a dense shell that might be prone to breakup. In all likelihood, prior instabilities, such as Rayleigh-Taylor instabilities in the shock, would pre-empt those due to H_2 cooling, but the radiative losses might still be relevant to the kinematics of the remnant. Molecular hydrogen cooling might also be viable in trapped explosions. Figures 3.8b and f show that the leading shock in the contained blast recombines and cools at much earlier times, at about the same time instabilities would erupt in the contact discontinuity. Rayleigh-Taylor instabilities in the reverse shock and Vishniac instabilities in the forward shock mediated by H_2 cooling could evolve together, destroying the shell from within and without.

In the absence of magnetic fields in the vicinity of the progenitor, how would the free expansion interact with the HII region or neutral halo? Simple collisional

cross section arguments imply that the ejecta particles would travel to great distances with little deflection by the surrounding gas unless magnetic fields mediate hydromagnetic interactions between the blast and its environment. If no primordial fields were present, the ejecta might interact differently with the halo than predicted by the fluid equations, which are predicated upon mean free paths in the flow being far shorter than characteristic lengths in the flow itself. Nevertheless, for now it is reasonable to suppose that magnetic fields arise due to the Weibel instability (e. g. Medvedev 2007), effectively coupling the two plasma streams. This mechanism has been invoked to explain the origin of GRB afterglows (Medvedev et al. 2007).

An important phenomenon not noted in earlier surveys of primordial supernovae are the large central infall rates that can result from fallback when remnants fail to escape massive halos, in excess of 10^{-2} $M_{\odot}$ yr^{-1} and lasting 1 - 2 Myr in some instances. Such infall, although less coordinated, would certainly appear in three dimensional simulations and lead to rapid growth of the central black hole. The growth would be episodic since bounceback would periodically reverse the inflow, and three dimensional radiation hydrodynamical accretion simulations would be required to ascertain how much gas at the center of the halo would fall into the black hole. Nevertheless, this mechanism may provide the means whereby black holes of several thousand solar masses could form in pregalactic structures at $z \sim 20$, which numerical studies suggest could be the origin of the supermassive black holes occupying the centers of most massive galaxies today (Li et al. 2007). Periodic accretion onto the black hole would emit bursts of radiation from the halo that might over time contribute to an x-ray background at high redshifts and strongly affect the thermal and chemical properties of the halo.

One alternative to this scenario is that gas in the trapped explosion instead cools to tens of Kelvin by metal-line cooling and then fragments, forming many low mass stars whose peculiar motions are confined to the dark matter potential of the halo. Several tens of thousands of solar masses of gas could fuel low mass star formation in this manner. If large numbers of small stars can truly form in the halo the result could be a globular cluster 15 - 30 pc in diameter, the radii to which gas in the halo is disturbed by the blast. High dynamical range adaptive mesh refinement (AMR) simulations are necessary to determine if gas in the halo can fracture and collapse in this fashion.

Finally, our supernova models may hint at an alternative pathway for the assembly of the first primitive galaxies. Greif et al. (2007) find that the first supernovae preferentially expel metals into the voids interspersed among cosmological filaments. Since densities are relatively low there, the metals do not promote immediate star formation, and must generally await merger timescales to be taken up into a new generation of stars. If supernovae ejecta instead mix efficiently with the dense shells of relic H II regions and cause them to cool and fragment, a second generation of stars with different chemical abundance patterns might promptly form. Likewise, explosions trapped by massive halos could also create small populations of new stars before mergers with other halos. If so, the first primitive galaxies were assembled sooner, with more stars and different chemical abundances than in current cosmological models. Upcoming observations by the *James Webb Space Telescope* and *Thirty Meter Telescope* might discriminate between these two scenarios.

Acknowledgments

We thank the anonymous referee, whose detailed comments significantly improved the quality of this work. We also thank Ken Nomoto for providing us his hypernova yields and Guillermo Garcia-Segura, Alex Heger, and Lars Bildsten for helpful discussions concerning these simulations. BWO was supported by a LANL Director's Postdoctoral Fellowship (DOE LDRD grant 20051325PRD4). This work was carried out under the auspices of the National Nuclear Security Administration of the U.S. Department of Energy at Los Alamos National Laboratory under Contract No. DE-AC52-06NA25396. The simulations were performed on the open cluster Coyote at Los Alamos National Laboratory.

Chapter 4

Circumstellar Interaction of Electron Capture Supernovae

B. van Veelen, N. Langer and R. Kotak
To be submitted to Astronomy & Astrophysics

Supernova explosions arising from the lowest initial mass single stars are not thought to be triggered by iron core collapse, but rather by the electron-capture induced collapse of an oxygen-neon-magnesium core. These electron-capture supernovae are thought to arise from super-AGB stars, which undergo core carbon burning and thermal pulses which may be linked to episodes of enhanced mass loss or extremely dense winds. Recently, several observed supernova explosions have been linked to super-AGB progenitors. Here, we quantitatively investigate the effect of the interaction between supernova ejecta arising from a 9 $M_{\odot}$ progenitor, and a circumstellar medium that has been shaped by a super-AGB wind. We provide quantitative predictions for the phase of the supernova when its radiation is dominated by the interaction of the supernova ejecta with the circumstellar medium. The simulations are performed using realistic time evolution of the surface and wind parameters from stellar evolution models as input, and using the ZEUS hydrodynamic code to produce the circumstellar medium conditions at the time of the supernova explosion. The subsequent interaction of the ejecta with the circumstellar medium is followed in both 1D and 2D simulations. In accordance with recent explosion models, we simulate only low energy explosions (10^{50} erg). However, we find that our models can produce rather high interaction luminosities (up to 10^{41} erg s^{-1}), especially for the case of low ejecta masses, where the luminosity remains above that limit for roughly a year after explosion. While the forward shock in our models is mostly adiabatic and will produce X-ray emission, we find the reverse shock to be radiative and capable of producing optical light, connected to low expansion velocities. The highly unstable contact discontinuity in between the two shocks leads to significant mixing and enhancement of the optical emission. We also derive constraints on the appearance of narrow Hα lines within the framework of our models. Comparing our results with supernova observations, we find broad agreement of the luminosities and velocity evolution, suggesting that a

subset of supernovae previously assigned to the core-collapse variety may, in fact, be electron-capture supernovae.

4.1 Introduction

There is general consensus that at least two physically distinct classes of supernovae (SNe) exist in nature. Of these, the type Ia SNe are believed to arise from the thermonuclear explosion of an accreting carbon-oxygen white dwarf that has reached the Chandrasekhar limit, with the white dwarf being totally annihilated in the process. The gravitational collapse of the core of a star originally more massive than about $8M_{\odot}$ gives the second group its name, and leaves behind either a neutron star or a black hole. Core-collapse SNe come in many varieties, with the main classification based on the presence (Type II) or absence (Type I) of hydrogen in near maximum light spectra. At least some of the observed properties of core-collapse SNe are believed to be determined by the mass and extent of the hydrogen and helium envelopes of the progenitor star.

Observationally, the vast majority of SNe have absolute peak magnitudes in the $-15 \lesssim M_R \lesssim -22$ range. Much of the diversity in the observed properties of core-collapse SNe e.g. brightness, light curve shape, spectral evolution, longevity, and ejecta velocity can be attributed to some combination of the physical properties of the progenitor star (e.g. mass), the energetics of the explosion itself (influencing total ejecta mass, and production of radioactive nickel), and environmental factors such as metallicity, or the presence of circumstellar matter in the vicinity of the progenitor star with which the fast-moving SN ejecta is forced to interact. Generally, the observed properties often have to be interpreted on a case-by-case basis, although it is possible to identify broad trends within subtypes of core-collapse SNe. Not unsurprisingly, given the many, and often untractable variables involved, a range of open issues still remain. At the most basic level, an observationally-supported mapping between the mass of the progenitor star, the class of SN, and the type and mass of the remnant, continues to elude us.

To add to this mix, recent years have witnessed a surge in the discovery of transient events that have challenged this traditionally strict segregation into the thermonuclear and core-collapse varieties. These have ranged from objects with extreme luminosities at the bright and faint ends (e.g. Quimby et al. 2009, Kulkarni et al. 2007, respectively), to those with seemingly large ejecta masses, implying the explosion of an extremely massive star (Gal-Yam et al. 2009, Young et al. 2010). Furthermore, the extremes in brightness are often – but not always – coupled to other extreme attributes such as very high, or very low estimates (or stringent upper limits) of the amount of radioactive nickel synthesized in the explosion, which can be a proxy of how energetic the explosion was. In the former case, this could imply the explosion of a very massive star, while in the latter, either the explosion of a low mass progenitor ($\sim 8\,M_{\odot}$), or a black-hole forming SN with substantial fall-back could equally well be invoked (Fryer 1999, Heger et al. 2003), meaning that the amount of ^{56}Ni cannot be the sole discriminant.

For objects at the extremely bright end of the transient spectrum ($R \lesssim -23$), there seems to be an uneasy accord that such events probably involve a catastrophic

SN-like explosion of a presumably very massive ($\sim 100\,M_{\odot}$) star (e.g. Woosley et al. 2007). Alternatives such as giant outbursts of luminous blue variables e.g. that of η-Carina, would simply not be energetic enough.

At the faint end however, the nature of the transient events is much debated, with explanations ranging from luminous red novae and V838 Mon analogues (Kulkarni et al. 2007, Bond et al. 2008), to faint type II-plateau SNe (Pastorello et al. 2007a), to outbursts of luminous blue variables (Smith et al. 2009, Berger et al. 2009). Two, well-monitored and uncannily similar events in this faint category clearly stand out: SN 2008S (Prieto et al. 2008, Thompson et al. 2009, Botticella et al. 2009), and NGC 300-OT (Bond et al. 2009, Berger et al. 2009). Both have been shown to have dust enshrouded progenitors, comparable peak magnitudes, and slow spectral evolution. In particular, the spectra of neither event showed lines broader than $\sim 3000\,\mathrm{km\ s^{-1}}$ (Berger et al. 2009, Botticella et al. 2009), which is roughly a factor of two slower compared to type II-Plateau SNe at comparable epochs. The narrow ($\lesssim$ few $100\,\mathrm{km\ s^{-1}}$) emission lines in both objects are reminiscent of SNe interacting with circumstellar material (i.e., type IIn SNe.).

Several authors have suggested that the observed behavior of SN 2008S and NGC 300-OT would be consistent with being electron capture (ec) SNe (Thompson et al. 2009, Botticella et al. 2009). The possible existence of ecSNe was proposed over a quarter of a century ago (Miyaji et al. 1980, Nomoto 1984, Hillebrandt et al. 1984) and are believed to arise from stars having initial masses in a narrow range (see below) such that they pass through the so-called super-asymptotic giant branch (SAGB) phase when they are able to ignite carbon in their cores, but as they are still of sufficiently low mass, that the ignition of neon, and the subsequent passage through to (iron) core-collapse cannot occur. Two possible outcomes, dependent on the interplay between mass loss and other interior processes, are envisaged for the O-Ne-Mg core: the onset of explosive burning due to electron capture reactions on to ^{24}Mg and ^{20}Ne, leading to the birth of a neutron star, or the formation of a relatively massive O-Ne-Mg white dwarf. Several authors have investigated the detailed evolution of SAGB stars e.g. Garcia-Berro & Iben (1994), Garcia-Berro et al. (1997), Kitaura et al. (2006), Siess (2007),Poelarends et al. (2008), Wanajo et al. (2009).

The predicted characteristics of ecSNe on the one hand, consisting of low explosion energy ($\sim 10^{50}$ erg), low ^{56}Ni mass, and low ejecta velocities, and the observed characteristics of the progenitors of SN 2008S and NGC 300-OT *viz.* cool, dust-enshrouded stars with luminosities of $\sim 10^5\,L_{\odot}$ seem consistent with those of SAGB stars. However, these two events are by no means the first for which an ecSN channel has been invoked. Most notably, an ecSN origin has been invoked for the Crab SN (Davidson et al. 1982, Nomoto et al. 1982, Kitaura et al. 2006) and for sub-luminous type II-Plateau SNe Kitaura et al. (2006) i.e. those with peak luminosities of $\lesssim 10^{41.5}\,\mathrm{erg\ s^{-1}}$.

Several studies delving into the physics of SAGB stars (e.g. Siess 2007, Poelarends et al. 2008) and the effect on stellar evolutionary tracks (e.g. Pumo et al. 2009) have been conducted. However, little attention has been paid to the interaction between a circumstellar medium shaped by a star that has passed through a super-AGB phase, and has therefore experienced recent and heavy mass loss, and ejecta resulting from a SN in a mass-range appropriate for ecSNe. Here we present

the first study of this kind. We begin by describing our choice of stellar evolution model and numerical techniques, followed by a description of our findings, and comparison with appropriate observations.

4.2 Methods

4.2.1 Stellar evolution model

We based our simulations on stellar evolution models of the type calculated by Schaller et al. (1992). Specifically, we considered the evolution of a 9 $M_\odot$ model until the end of its carbon burning phase i.e., until the onset of the SAGB phase. From a comparative study of stellar evolution codes, Poelarends et al. (2008) found that the initial mass range leading to the SAGB phase spanned 7.5–9.25 $M_\odot$, but only the 9–9.25 $M_\odot$ range actually led to electron-capture SNe. They noted that the exact mass range depended on the treatment of semi-convection and convective overshoot. This is not surprising given that whether or not the core will reach the Chandrasekhar limit depends on the complex interplay between mass loss on the one hand, and details of internal physical processes (e.g. rotation, semi-convection) and the initial conditions (e.g. mass) on the other. However, given that various observational prescriptions of mass loss did not significantly alter their results (Poelarends et al. 2008, Figs. 15, 16), here we simply adopt a mass loss rate of 10^{-4} $M_\odot$ yr^{-1} for the entire duration of the SAGB phase.

Given that the underlying driving mechanism for mass loss during the SAGB phase is largely unknown, the wind velocity during this phase is similarly uncertain. Therefore, choosing a value that is in line with the escape velocity seems most logical: for a star with $L = 10^5$ $L_\odot$, $T_{\rm eff} = 3000$ K, and $M = 8$ $M_\odot$, the escape velocity is 50 km s^{-1}. However, the escape velocity is likely an upper limit to the true wind velocity. Eldridge et al. (2006) provide a formulation that can be used to modify the escape velocity taking the luminosity of the star into account, as well as incorporating commonly-used, but uncertain parametrisations of the complex physical processes that accelerate the stellar wind. With this formulation, we find that for giants, the wind velocity is a certain fraction, always less 1, of the escape velocity. For stars with the lowest effective temperature ($T_{\rm eff} \leq$ 3600 K, see Eldridge et al. 2006) this fraction can be as low as 30%. For this study, we chose a representative value of 20 km s^{-1} for the wind velocity of the SAGB model under consideration, and in the interests of simplicity, did not vary this value during the SAGB phase.

In order to study the consequences of varying the relative amount of material contained in the circumstellar medium versus the SN ejecta, we varied the total amount of time taken for the core to grow to the Chandrasekhar mass, and create an ecSN. At the end of the carbon burning phase, the mass of our 9 $M_\odot$ model has decreased to 8.605 $M_\odot$. Excluding the material contained in the core (1.375 $M_\odot$), a total of 7.23 $M_\odot$ is available to be lost either in an SAGB wind, or as SN ejecta. The amount of material shed by the wind depends naturally on the amount of time taken for the core to grow to the Chandrasekhar mass, and the assumed mass-loss rate. We chose two different lengths of the SAGB phase to probe the extreme cases whereby most of the material was either contained in the CSM or SN ejecta, and an additional intermediate case where the CSM and ejecta masses were comparable.

Table 4.1: Adopted values of the SAGB life time, the SN ejecta mass and the amount of mass in the CSM due to the SAGB wind.

$\tau[yr]$	$\Delta M_{ej}[M_\odot]$	$\Delta M_{CSM}[M_\odot]$
12 000	6.03	1.20
40 800	3.15	4.08
69 700	0.26	6.97

The lengths of the SAGB phase in each case, as well as the relative distribution of material is shown in Table 4.1.

The most distinguishable feature of an ecSN compared to its bigger core collapse supernova (CCSN) brother is the total amount of energy in the explosion. The most recent models of Kitaura et al. (2006) suggest that the explosion energy associated with ECSN is as low as 10^{50} erg. Therefore we simply adopt a single value for the supernova explosion energy equal to 10^{50} erg.

4.2.2 Numerical method

The simulations presented here were carried out with 3D magneto-hydrodynamics code, ZEUS MP (Hayes et al. 2006), but neglecting the effects of magnetic fields and gravity. Radiative cooling was included using a cooling curve from Smith et al. (2008a) calculated for a gas of solar metallicity and a number density of 1 cm^{-3}. Using this cooling curve we are able to compute a light curve resulting from the interaction of the SN ejecta with the CSM. This calculation makes use of the optically thin approximation which assumes that all the energy lost by radiative cooling immediately leaves the system and does not contribute in any way to the hydrodynamical calculation after it has been lost. We discuss this assumption further in Section 4.5, since this influences the details of the results.

The pre-SN simulation of the stellar wind flowing into the interstellar medium (ISM) was done by using the same method as applied in García-Segura et al. (1996b). At every time step, the density, velocity, and temperature in the first 5 radial grid cells is set in accordance with the current mass loss phase (Fig. 4.2).

The simulations were carried out in two consecutive steps. First, the evolution of the CSM due to the stellar wind alone was considered. We took these results of this simulation at different times i.e., corresponding to different lengths of the SAGB phase, and used these as input for the next step. This second step consisted of simulating the interaction of the SN ejecta with the CSM, which has been altered by the stellar wind. By using the output of the first step at different times, different amounts of mass in the CSM due to the SAGB wind are obtained, and the SN ejecta mass was adjusted to conserve the total amount of material in the CSM and ejecta.

We set up the density and velocity profiles for the SN ejecta in the same manner as described in Whalen et al. (2008), we assumed the following form for the density and velocity profiles of the SN ejecta:

$$\rho(v,t) = \begin{cases} F \cdot t^{-3} & \text{for} \quad v \leq v_{\text{core}} \\ F \cdot t^{-3} \cdot (\frac{v}{v_{\text{core}}})^{-n} & \text{for} \quad v_{\text{core}} < v \leq v_{\text{max}} \\ \rho_{\text{CSM}} & \text{for} \quad v > v_{\text{max}} \end{cases} , \tag{4.1}$$

$$v(r,t) = \frac{r}{t} \text{ for } t > 0\,, \tag{4.2}$$

where ρ is the density, t is the time since explosion, v is the velocity and r is the radius at which we are setting up the supernova ejecta. We set up the ejecta in the inner 80% of the initial radial range of the grid. The SN ejecta mass and energy are used to calculate F and $v_{\rm core}$, which are normalization constants. From SN observations, the maximum ejecta velocity measured is around 30 000 km s^{-1} which we accordingly set as our maximum velocity ($v_{\rm max}$). The explosion energy of the SN is assumed to be completely kinetic. The exponent n in Equation 4.1 is set to 9 for all simulations, which is a typical value assumed for the power law representation given above (Truelove & McKee 1999, Dwarkadas 2005, Chugai & Chevalier 2006).

The spatial scales on which the SN ejecta interact with the CSM change dramatically. Initially, the radial range is approximately equal to the stellar radius, while at later phases, this can become several orders of magnitude larger. In order to accommodate all necessary ranges while simultaneously maintaining a high spatial resolution at all times, we used the expanding grid option in ZEUS MP. We set the initial radial range to 10^{14} cm, and followed the expansion of the SN ejecta as it evolved. At each time step, the radial range of the grid is enlarged with the maximum velocity in the outer regions of the grid determining the scaling factor. The total number of grid cells is conserved, with the cells simply redivided over the new radial range of the grid. The number of angular grid cells of the range in the angular direction is constant. We refer the reader to Whalen et al. (2008) for further details regarding the overall numerical setup.

All simulations were carried out on a spherical grid (r, θ, ϕ). The pre-SN simulation was performed in two dimensions, assuming symmetry in the ϕ direction. The radial range was divided into two parts, with the first ranging from 0 to 8 pc with 1000 grid cells, and the second ranging from 8 to 42 pc with 500 grid cells. The angular direction contained 200 grid cells ranging from $\frac{\pi}{4}$ to $\frac{3\pi}{4}$.

The simulations for the interaction of the SN ejecta with the CSM described in Section 4.4.1 were also performed in two dimensions. For these simulations the initial maximum radius was equal to 10^{14} cm, over which 1000 grid cells were divided. The angular direction ranged from $\frac{\pi}{4}$ to $\frac{3\pi}{4}$ and comprised 320 grid cells. The results of the simulations shown in Section 4.4.2 where we attempt to derive a scaling relation between the luminosity, density structure of the CSM, and the SN ejecta are obtained from one dimensional simulations. In these simulations we only impose symmetry in the ϕ direction, with the same initial parameters in the radial direction as the two dimensional simulations described in Section 4.4.1.

4.3 Shaping the CSM

The Hertzsprung-Russell diagram in Fig. 4.1 shows the evolutionary path of the 9 $M_\odot$ stellar model from Schaller et al. (1992) that we used as input for our simulations. Using the built-in mass loss rate prescriptions for the pre-SAGB provided by this model, we calculated the evolution of the corresponding wind velocity up to, but not including the SAGB phase, using the formulation described in Eldridge et al. (2006). As described earlier, this formulation uses the escape velocity of the

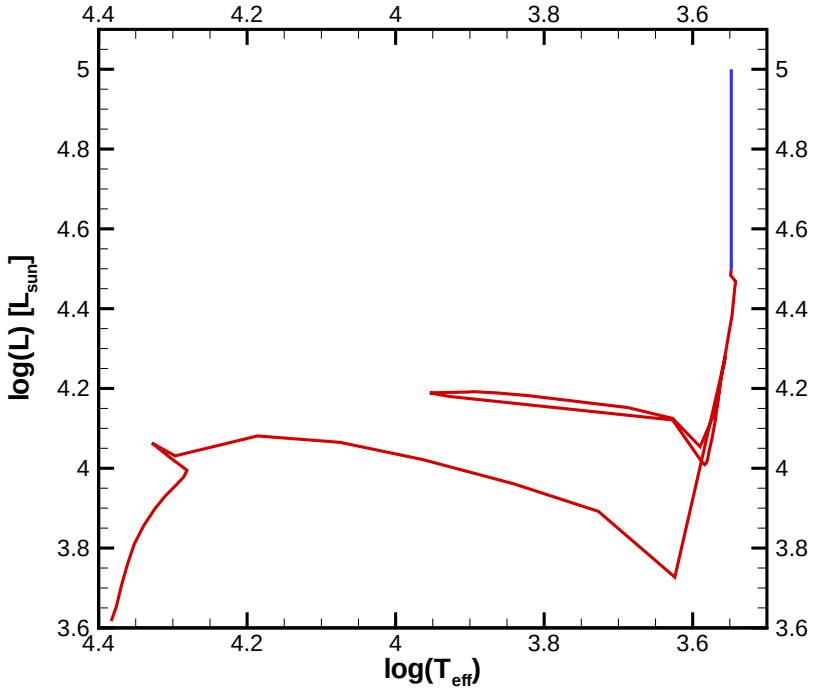

Figure 4.1: Evolution of the $9M_{\odot}$ model. The red line shows the calculations by Schaller et al. (1992), while the blue line shows our assumed values for the SAGB phase.

star, the luminosity, and a scaling factor that is determined by the effective temperature.

The results of these calculations can be seen in Fig. 4.2 where we show both the mass loss rate and the terminal wind velocity commencing at the final stages of the main sequence phase. Between 26.5 and approximately 28 Myr, the star is a RSG with a low wind velocity and a relatively high mass loss rate. This is followed by a blue loop phase that lasts for approximately 1 Myr during which the wind velocity increases, and the mass loss rate correspondingly decreases. This blue loop can also be seen in Figure 4.1 as the excursion to higher temperatures between $\log(T_{\rm eff})$ = 3.6 and 4. After the blue loop, the star enters the AGB regime where its mass loss rate slowly increases. As described earlier, for the final SAGB phase we assumed a mass loss rate of 10^{-4} $M_{\odot}$ yr^{-1} , a wind velocity of 20 km s^{-1} and a luminosity of 10^5 $L_{\odot}$. These values are shown in Figures 4.1 and 4.2 as blue lines.

In Fig. 4.3 we show a one dimensional density profile of the pre-SN CSM density structure. Although the simulation was done in two dimensions, there were no significant two dimensional effects such as turbulence due to instabilities. The features in the CSM can be linked to the different mass loss phases during the stellar evolution. The mass loss during the main sequence phase has created with a radius

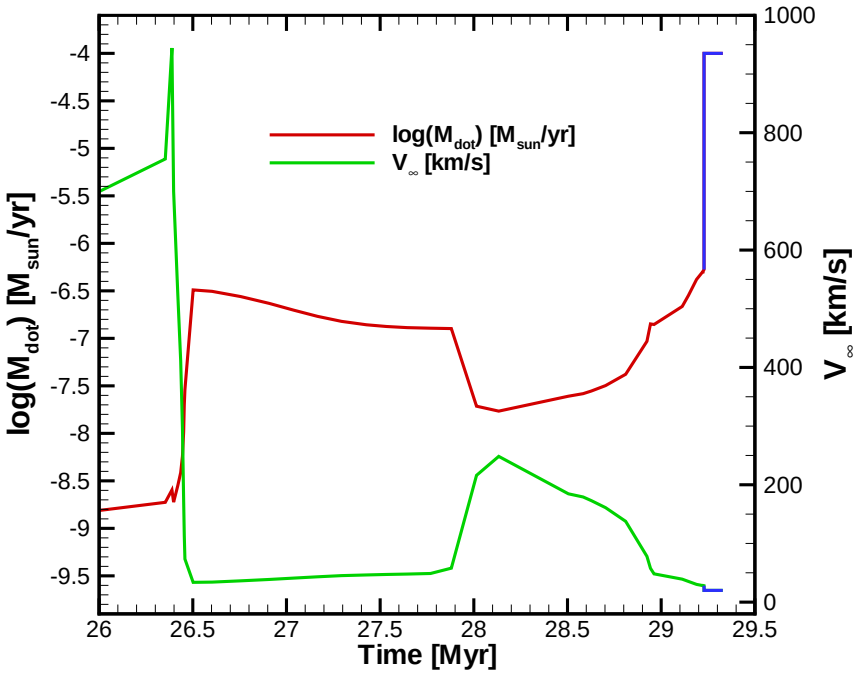

Figure 4.2: The mass loss rate and wind velocity as a function of time for the $9M_{\odot}$ model. The red and green lines show the results of calculations by Schaller et al. (1992), while the blue line shows our extension to the model corresponding to the SAGB phase. The time axis runs from the end of the main sequence phase, through the red supergiant, blue loop, and the SAGB phases.

of around 38 pc, which contains all the swept up ISM. The hot bubble inside that shell has a very low density but very high temperature and pressure. As a result, the mass lost during the following RSG phase is stalled against this high pressure region, and accumulates in the RSG shell which can be seen around 16 pc. At the end of the RSG phase (~28 Myrs) there is a strong drop in the mass loss rate and a simultaneous increase in the wind velocity due to the blue loop. Due to the higher wind velocity, the material close to the star is swept up and accumulates into another shell which can be seen around 7 pc. Following the blue loop the mass loss rate slowly increases while the velocity decreases again as the star goes up the AGB. Towards the end of its life the star enters the SAGB phase during which the mass loss rate increases dramatically to our assumed value of 10^{-4} $M_{\odot}$ yr^{-1}. The mass lost during this phase can be seen as the very high density region in the inner 1.5 pc of the CSM.

In the following section we describe the results obtained from our ejecta-CSM interaction simulations, which are considered for a maximum of ~3 years follow-

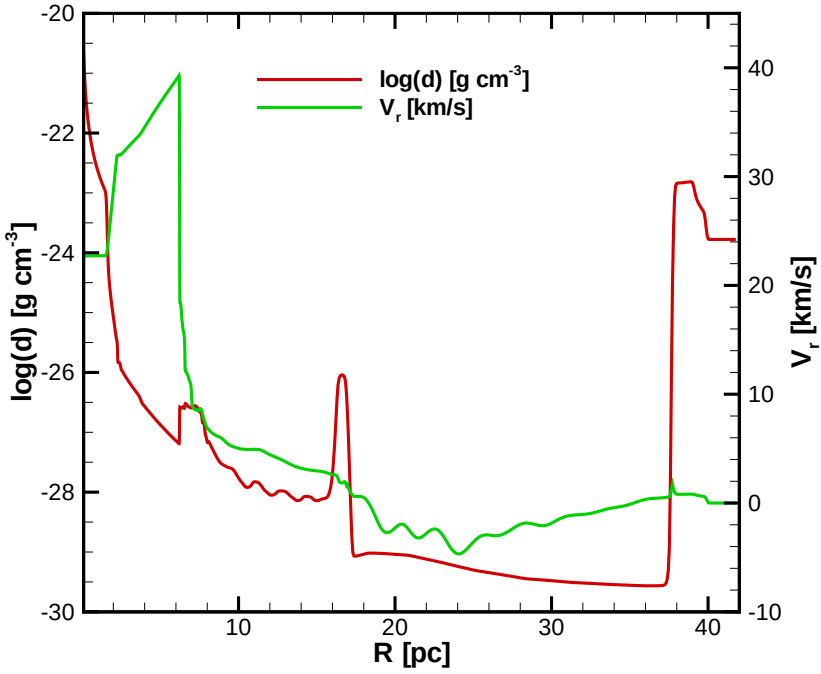

Figure 4.3: One dimensional density and velocity structure of the pre-SN circumstellar medium. The left axis shows the density, while the right axis shows the radial velocity. The inner 2 pc are shaped by the wind during the SAGB phase. The MS and RSG shell can be seen at 38 and 16 pc, respectively. During the blue loop the velocity of the wind increased over an extended amount of time. This has created another shell around 7 pc. The wind during the SAGB phase has increased the density of the inner 1.5 pc.

ing the SN explosion. Within this time the SN ejecta will not be able interact with the material beyond 1.5 pc. This means that all effects of changes in the mass loss behavior prior to the SAGB phase will have no influence on the interaction of the SN ejecta with the CSM. All the simulations described in Section 4.4.1 will encounter the same CSM. However, the remaining CSM may well have observational consequences, which we will discuss later.

4.4 Exploding in a superwind

4.4.1 2D models

The velocity distribution of the SN ejecta as a function of mass is shown in Fig. 4.4. Each model is scaled to its own amount of ejecta mass, which is shown in the legend. It is clear that the model with the lowest amount of SN ejecta mass has the

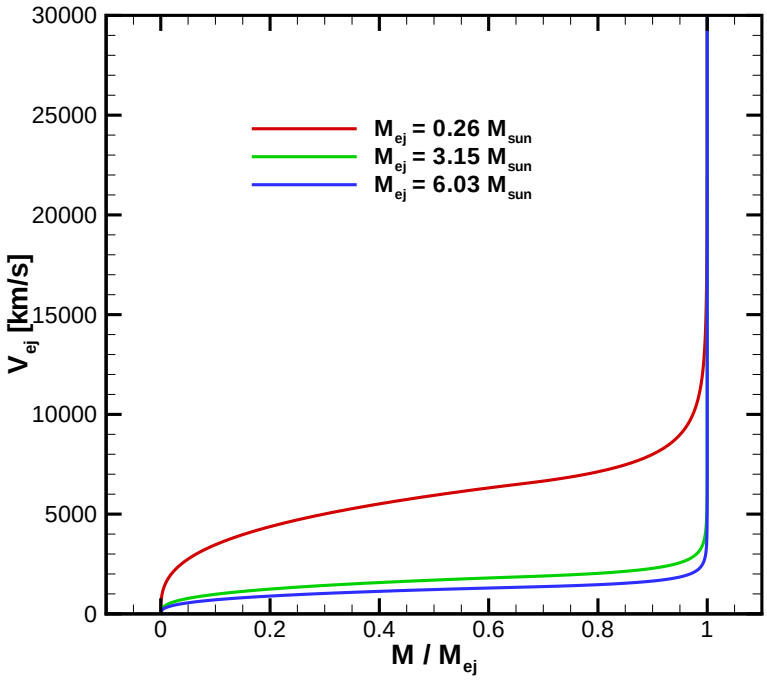

Figure 4.4: Velocity profile of SN ejecta with respect to mass coordinate. Each model was scaled to its own value of the SN ejecta mass (see legend). As the SN ejecta energy is fixed, the model with the least amount of mass has the highest average SN ejecta velocity. From this figure it can also be seen that there is only a very small amount of mass (and thus also energy) is moving at velocities exceeding 15000 km s^{-1}.

highest average ejecta velocity, which is to be expected since we have fixed the SN ejecta energy. What this figure also shows is that although we chose a maximum ejecta velocity of 30 000 km s^{-1}, the amount of mass at this velocity is extremely low. The total amount of mass at velocities above 15 000 km s^{-1} is less than 1% for all models. The effect that this part of the SN ejecta will have on the evolution will thus be negligible.

Since all models show a similar structure of the SN after 3 years, we show just one example of the resulting density structure in Fig. 4.5 for the model with an ejecta mass of 0.26 $M_{\odot}$. The forward shock can be seen around 0.022 pc and the reverse shock around 0.018 pc. The high density material in between these two shocks was once a thin shell between the reverse shock and the contact discontinuity. This thin shell was unstable due to the thin shell instability and fragmented into smaller and denser clumps. Due to the high density of the material in the thin shell and in the clumps, energy is radiated away very efficiently. The majority of the material at these high densities (>50%) consists of ejecta material.

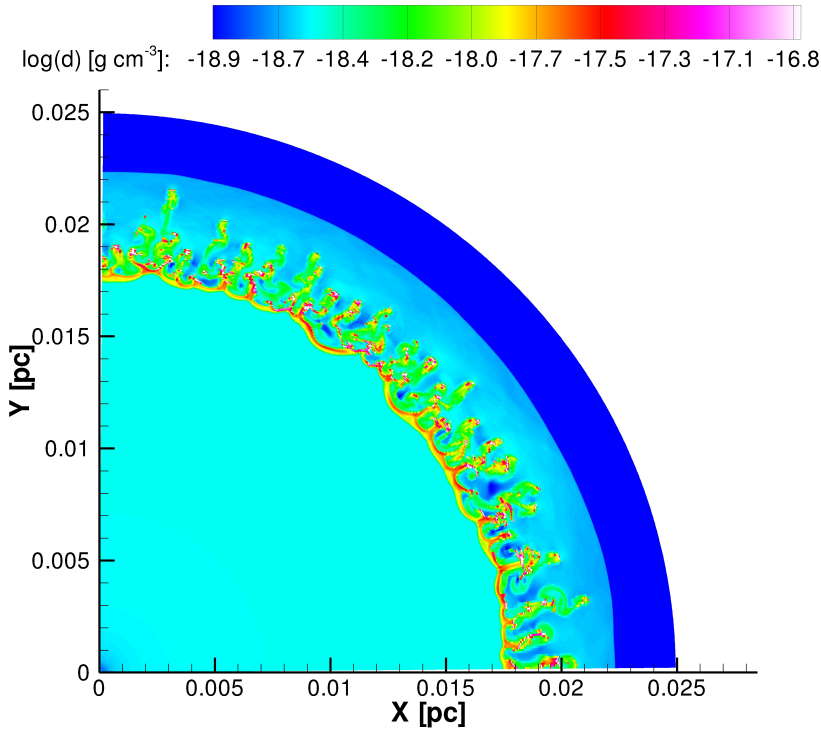

Figure 4.5: Density structure of the two dimensional model with $M_{ej} = 0.26\ M_{\odot}$, 10^8 seconds after the SN explosion. The thin shell between the contact discontinuity and the reverse shock, which was thin due to the cooling, has broken up as a result of the thin shell instability. Outside of the forward shock (~ 0.022 pc) the CSM is shaped by the free streaming SAGB wind.

Figure 4.6 shows the forward and reverse shock radii for our three models as a function of time. In all cases, the forward shock radius is so small that the region of the CSM they are expanding into is still only shaped by the free streaming SAGB wind. In this region of the CSM, the density structure still corresponds to a r^{-2} profile. This means that the amount of mass swept up by the supernovae is linearly proportional to the radius of the forward shock. Due to the higher average SN ejecta velocity of the model with the least amount of ejecta mass it is able to move outward further within the same amount of time, resulting in a larger forward shock radius and thus a larger amount of swept-up mass.

Not only does the model with the least amount of ejecta mass sweep up the highest amount of circumstellar mass in an absolute sense, but it has also swept up a much larger fractional amount of mass compared to its own amount of ejecta mass. This results in a stronger interaction of the SN ejecta with the CSM and a stronger reverse shock. A stronger reverse shock in turn leads to a larger amount of shocked ejecta mass, which increases the energy that can be radiated away.

This effect can be seen in Figure 4.7, which shows the light curves for the three

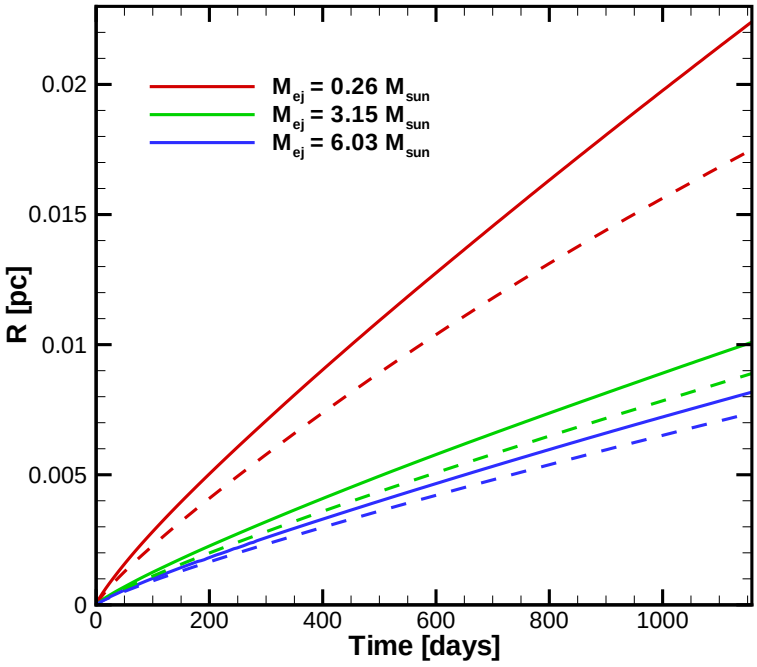

Figure 4.6: Angle-averaged radius of the forward (solid) and reverse shock (dashed) for the 3 two dimensional models as a function of time. Due to the higher average velocity of the SN ejecta mass and the fact that the supernova ejecta interacts with a small amount of mass compared to the mass in the supernova ejecta, the model with the least amount of ejecta mass has the largest shock radii.

models. We generated light curves in the following way. At each location in our grid, the amount of energy lost due to radiation is a known quantity for each time step of the simulation. Assuming that the surrounding medium is optically thin, we simply integrate over the entire grid to find a luminosity at a given time. Each panel in Figure 4.7 correspond to one model and in each panel we show the total light curve, the light coming from cold gas ($T < 10^5$K) and the light coming from hot gas ($T > 10^5$K). As expected, the model with the least amount of mass has the highest luminosity. Shortly after the supernova explosion the luminosity from the hot gas from the forward shock dominates, because the material it shocks has a high density. As the forward shock expands into a lower density medium and decelerates, the luminosity of the hot gas drops. At later times the luminosity coming from the cold gas dominates. This cold gas is material that was compressed by the reverse shock into a cold dense shell. Due to the thin shell instability, this shell has broken up and parts of it are mixed into the region of the shocked CSM, where it keeps on cooling. Since the luminosity from the cold gas, with tempera-

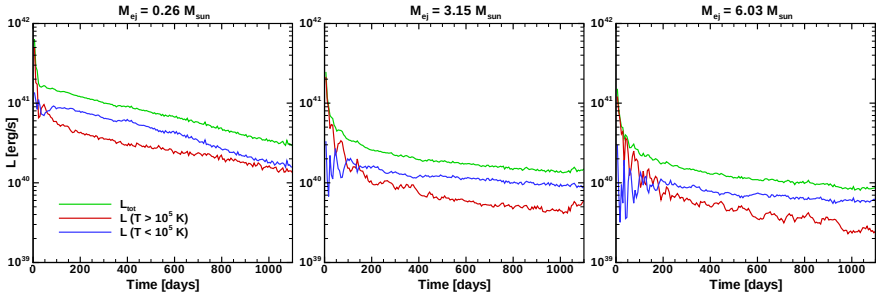

Figure 4.7: Light curves of the two-dimensional models with a different ejecta mass for each panel. From left to right we show the model with 0.26, 3.15 and 6.03 $M_\odot$ of supernova ejecta, respectively. Each panel shows the total luminosity in green and the luminosity of cold (blue) and hot (red) gas, with the boundary between hot and cold at $T = 10^5$K. Due to the larger shock radius of the model with the least amount of SN ejecta mass, this model is able to interact with more mass in the CSM. This results in a higher luminosity at any given time. The luminosity from the cold gas is most likely emitted in the optical regime and is therefore a good estimate for the optical light curves.

tures below 10^5K, will most likely be emitted in the optical regime, this is a good approximation for the optical light curve.

As a consistency check to ensure that the energy radiated away by the SN actually escaped the system, we computed the optical depth of the pre-SN CSM. As we had no information regarding the ionization fraction, we simply assumed that all material was completely ionized, providing an upper limit to the optical depth. The electron scattering optical depth is calculated using:

$$\tau = \int \kappa \, \rho \cdot \mathrm{d}r = \int 0.2 \, (1 + X) \, \rho \cdot \mathrm{d}r, \tag{4.3}$$

where κ is the electron scattering opacity, X is the hydrogen mass fraction and ρ is the density. If we take the inner radius to be at 10^{14} cm, which roughly corresponds to the stellar radius, we find a maximum optical depth of 0.8. Since this value is an upper limit, we can assume that the CSM remains optically thin to the radiation arising from the ejecta-CSM interaction.

After a steep initial decline, the total luminosity in our models remains high for a considerable amount of time. Given the fact that the light curves of the three 2D models are relatively flat after ~100 d, it is possible to define an average luminosity of the SN over the period during which the luminosity is approximately constant. The two most important parameters which define the value of the luminosity during this time are the density structure of the CSM, and the total mass of the SN ejecta. We discuss this further in the next section, where we attempt to find a scaling relation for the average luminosity.

4.4.2 1D models

In order to find a scaling relation between the average luminosity, the density structure of the CSM and the SN ejecta we ran 16 one dimensional simulations. As

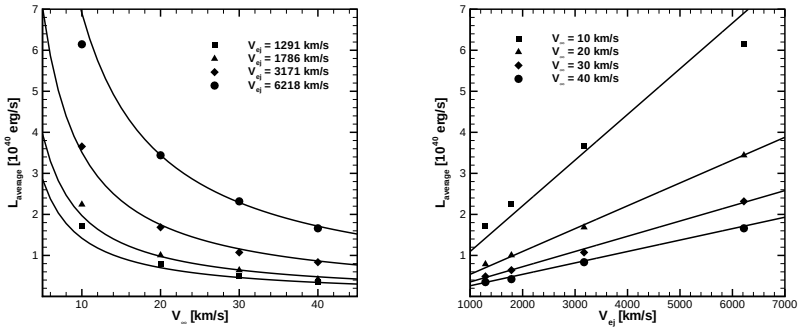

Figure 4.8: Average luminosity as a function of the SAGB wind velocity **(left)** and average SN ejecta velocity **(right)**. The squares show the values of the 1D models (Table 4.2), with each symbol representing a different value of the average SN ejecta velocity or the SAGB wind velocity (see legend). The lines show the values we would find using our scaling relation (Eq.4.6).

discussed above, there are uncertainties within the parameters we have assumed for the SAGB phase. The major uncertainties are the velocity of the SAGB wind, the length of the SAGB phase, and the mass loss rate during the SAGB phase.

We are interested in the parameters that determine the CSM density structure and the SN ejecta. For a fixed the mass loss rate, the velocity of the stellar wind during the SAGB phase is the only parameter that determines the CSM density structure, since the SN ejecta are expanding only into the free streaming part of the SAGB wind. The length of the SAGB does not play a role in this respect.

However, the length of the SAGB phase does determine the total amount of mass lost during this phase, and consequently also the amount of mass in the SN ejecta. Since we have fixed the energy of the SN explosion to 10^{50} erg, the distribution of the SN ejecta is determined solely by the amount of mass contained in the ejecta. The parameter we use to illustrate this is the average ejecta velocity, which is calculated by:

$$\overline{v_{\rm ej}} = \sqrt{\frac{2E_{\rm ej}}{M_{\rm ej}}} \tag{4.4}$$

We chose four different values for the SAGB wind velocity: 10, 20, 30, and 40 km s^{-1}. We also chose four values of the average ejecta velocity: 1291, 1786, 3171, and 6218 km s^{-1}. These values correspond to ejecta masses of 6.03, 3.15, 1.00, and 0.26 $M_\odot$ respectively. For each of the four different SAGB wind velocities we ran four simulations with the different average ejecta velocities, resulting in a total of 16 simulations (Table 4.2). All other parameters for the simulations were the same as for the two dimensional models described in the previous section.

The SAGB wind velocity and the average ejecta velocity were chosen as scaling parameters because they provide an intuitive first estimate for the expected scaling behaviour. A crude first approximation is that the average luminosity scales linearly with the average ejecta velocity, but inversely with the SAGB wind velocity. The reasoning behind the inverse linear proportionality is as follows: increasing the

wind velocity during the SAGB phase by a certain factor (say α) results in the amount of mass within a given region decreasing by α. Assuming that the behaviour of the forward shock is unchanged, one would then expect the amount of swept-up mass to also be lower by a factor of α. Now if the fractional amounts of mass shocked at both the forward and reverse shocks remain constant per given time interval, then the amount of shocked mass at the reverse shock will also decrease by a factor of α. The net result is that the average luminosity decreases by the same factor as the increase in SAGB wind velocity.

The linear proportionality with the average ejecta velocity follows from a similar line of reasoning. We begin by assuming that an increase in the average ejecta velocity by a certain factor (say ξ) will result in an increase in the velocity of the forward shock also by ξ. If, as before, this results in equal fractional amounts of mass swept up at the forward and reverse shocks, then this, in turn, will yield an increase in the average luminosity by a factor of ξ.

Both of the above lines of reasoning depend crucially on the behaviour of the forward shock. That only a relatively small amount of swept-up material results lends confidence to the assumption that the behaviour of the forward shock does not change drastically following a change of input parameters. In none of the models is the SN ejecta completely shocked. In the $3.15 M_\odot$ model the total amount of shocked ejecta is only 3% of the total ejecta mass at the end of the simulation.

The average luminosity of the 16 simulations is calculated by averaging the luminosity between 100 days and the end of the simulation, at approximately 3 years post-explosion. The first 100 days are excluded because during this time the light curves show a very strong decline due to the fast deceleration of the forward shock. We are specifically looking for an average value which corresponds to the luminosity of the SN during the phase in which the luminosity is approximately constant.

In figure 4.8 we show the average luminosity as a function of the SAGB wind velocity and the average ejecta velocity. Both panels show all 16 one dimensional simulations of the ejecta-CSM interaction that we have performed. The lines in the figures represent the values of a fitted function of the form:

$$\overline{L} = a + b \cdot \frac{\overline{v_{\rm ej}}}{v_\infty}. \tag{4.5}$$

where a and b are constants to be determined. By using a χ^2 minimization method, we found $a = -1.714 \cdot 10^{38}$ and $b = 1.113 \cdot 10^{38}$. We estimate the uncertainties as follows: If we assume a 10% uncertainty in the values of $\overline{L}$, we get errors in a and b of $3.291 \cdot 10^{38}$ and $4.683 \cdot 10^{36}$ respectively. The formal error in the slope is thus only 4%. The reduced χ^2 of this fit is 0.759. However, assuming a 20% uncertainty in the luminosity, we find the same values for a and b, but the errors become larger. The error in the slope rises to 8% with a reduced chi-square of 0.1898.

There is at least one additional factor in this function that should be taken into account. In the one-dimensional simulation we are not able to fully resolve the thin shell at the reverse shock. This introduces a discrepancy between the one-dimensional and the two-dimensional simulations. In the latter, the thin shell is able to break up (see Fig. 4.5) and create an effectively larger region which is able to radiate away energy. This gives an effective increase in the total energy radiated

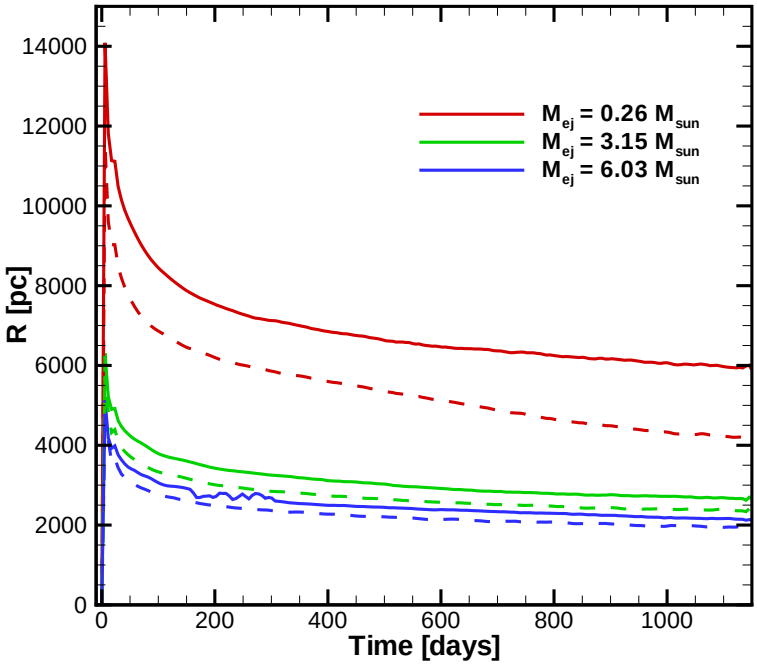

Figure 4.9: Velocity of the forward (solid) and reverse shock (dashed) of the two dimensional models as a function of time.

away at any given point in time when comparing the one-dimensional with two-dimensional simulations. Comparing the results from the one- and two-dimensional simulations, with the same parameters for the SAGB wind velocity and the average ejecta velocity, we found that the increase in the average luminosity is $1.77^{+0.21}_{-0.26}$. The final scaling relation thus becomes:

$$\overline{L} = 1.77 \cdot (-1.714 \cdot 10^{38} + 1.113 \cdot 10^{38} \cdot \frac{\overline{v_{\mathrm{ej}}}}{v_{\infty}}) \tag{4.6}$$

In Figure 4.8 it can be seen that the scaling relation gives a good prediction of the average luminosity we find in our models. Equation 4.6 thus gives us a rough indication of the luminosity one can expect for a given value of the SAGB wind velocity and the average ejecta velocity for a fixed mass loss rate and SN explosion energy.

Table 4.2: Values for the average luminosity (in 10^{40} ergs) as a function of the average ejecta and SAGB wind velocities for the 16 1D models.

v_∞ (km s^{-1}) \ $\overline{v_{ej}}$ (km s^{-1})	1291	1786	3171	6218
10	1.7140	2.2417	3.6551	6.1449
20	0.7884	1.0055	1.6856	3.4405
30	0.4887	0.6414	1.0730	2.3177
40	0.3498	0.4222	0.8351	1.6609

4.5 Comparison with observations

We compare the results of our simulations to observations of SN 2008S, which has been suggested to be the result of an ecSN (Thompson et al. 2009, Botticella et al. 2009). As the envelope of the progenitor is still present at the time of the explosion in ecSN models, it is natural to include type II-Plateau SNe in any comparison. Indeed, Kitaura et al. (2006) suggested that ecSNe may be responsible for a subset of type IIP SNe at the low luminosity end of the type IIP luminosity distribution.

For comparison with type IIP SNe, we also estimated the length of the plateau phase from our 2D simulations. By assuming that all the material in the simulation is ionized, we calculated the radius at which the optical depth would be equal to 1. This was done by integrating from the outside inward, starting just outside the forward shock, using Equation 4.3. Assuming a temperature of 5000K at this radius, we can estimate the luminosity coming from this distance. Note that since we do not account for a decrease in the radius due to recombination, the luminosity we find this way is an upper limit.

Using the calculated luminosity we define a thermal time scale: $\tau_{\rm therm} = \frac{E}{L}$, where E is the total thermal energy still remaining in the SN ejecta inward of the photospheric radius and L is the total luminosity. The point in time where the thermal time scale equals the time after the explosion is a rough estimate of the end of the plateau phase. We show the time-evolution of $\tau_{\rm therm}$ for the 2D models in Figure 4.10. All models show a very fast decline in the thermal time scale which is mainly due to the very strong decrease in the thermal energy contained in the supernova ejecta. This in turn is due to the adiabatic expansion cooling down the supernova ejecta very fast in the first few days. The estimated values for the end of the plateau phases is 9.4, 11.2 and 11.5 days for the models with 0.26, 3.15 and 6.03 $M_\odot$ of supernova ejecta respectively. Note that since the calculated luminosity is an upper limit, the values calculated for the thermal time scale are lower limits.

In Fig. 4.11, we show the quasi-bolometric light curves of SN 2008S and a sample of IIP SNe taken from the literature. We have included SNe 1999em and 2004et which were found to be at the normal-bright end of the IIP distribution to display the range in light curve shape and behavior exhibited by IIP SNe, and also because these two events were particularly well-monitored. Note that for these two events the explosion energy would be at least an order of magnitude higher than assumed in our calculations.

Two major shortcomings in the model light curves compared to the observations can be identified: first, none of the models reproduce the broad rise to peak lumi-

nosity displayed by SN 2008S; secondly, after 2-3 months, the luminosity of the models substantially exceeds the observed luminosity, with the discrepancy growing with time. When data is available for the post-plateau phase, all of the observed IIP SNe light curves shown here decline on timescales expected from the radioactive decay of ^{56}Co. We remind the reader that the entire luminosity output of the model light curves arises from interaction with the CSM, and that complex radiative transfer processes occurring in the SN ejecta and CSM are not treated in detail here. Furthermore, in order to make the problem tractable, we fixed a number of parameters (Sections 4.3, 4.4) which may not necessarily constitute the best possible choice for an individual SN. In light of this, we find the results encouraging.

The high X-ray luminosity in SN 1988Z at late times is most likely due to an interaction with the CSM (Turatto et al. 1993). Fabian & Terlevich (1996) and Schlegel & Petre (2006) find an X-ray luminosity of $3.4 \cdot 10^{40}$ erg/s and $2.7 \cdot 10^{39}$ erg/s at 2335 and 5678 days after the supernova explosion, respectively. If we compare this to $L_{\rm hot}$ of our simulations (Fig. 4.7), which can be considered a proxy for the X-ray light curve, we see that after ∼1100 days the maximum value is $\sim 10^{40}$ erg/s. The absolute values of the X-ray luminosity of SN 1988Z are higher than the predictions from our models which might be due to the higher inferred CSM densities for SN 1988Z (Aretxaga et al. 1999). The qualitative behaviour of the light curve is nevertheless very similar.

Two different models have been suggested to explain the observations of SN 1988Z. One is the interaction of the supernova ejecta with a high constant density CSM of $\sim 10^7$ cm^{-3} (Aretxaga et al. 1999). The other is a clumpy CSM in which the average mass loss rate was $\sim 10^{-4} M_\odot$ yr^{-1}during the final phase of the progenitor evolution (Williams et al. 2002). Interestingly, Williams et al. (2002) found a drop in the radio flux density after ∼1750 days, which they interpret as a drop in the number density of the clumps. Assuming 20 000 km s^{-1} for the shock velocity and 10 km s^{-1} for the pre-supernova wind velocity, they find that this change in the progenitor mass loss occurred around 10 000 years before the supernova explosion. This is roughly the same time scale of the SAGB phase in our models.

The slope, α, of the $L_{\rm hot}$ curves ($L_{\rm hot} \propto t^\alpha$) of each of our models i.e., with $M_{\rm ej}$ = 0.26, 3.15 and 6.03 $M_\odot$, are −0.8, −0.5, and −0.7, respectively. α was calculated by considering the decline in the light curve from 100 days to the end of the simulation. Our values are considerably less steep when compared to that of SN 1988Z, where a slope of −11/7 (Aretxaga et al. 1999) or −2.6 was found (Schlegel & Petre 2006). Several effects could cause this difference. First of all, the $L_{\rm hot}$ curve is only a proxy for the X-ray light curve, it is not the X-ray light curve itself. Secondly, we did not tailor any of our models to match the observed behaviour of SN 1988Z e.g., by varying the CSM density, supernova ejecta mass, and energy, all of which are likely to significantly alter the results. Finally, our estimated values of α are only valid during the first 3 years, while the slopes found in the above-mentioned studies extend over much longer periods.

Another comparison could be drawn between our simulations and SN 1986J, which also showed high late time fluxes at X-ray (Temple et al. 2005), optical (Milisavljevic et al. 2008), and radio (Bartel et al. 1991, Pérez-Torres et al. 2002) wavelengths. Models for the interaction of the supernova ejecta with the CSM estimate a pre-supernova mass loss of $\sim 10^{-4}$ $M_\odot$ yr^{-1}with a wind velocity of $\sim$ 10 km s^{-1}

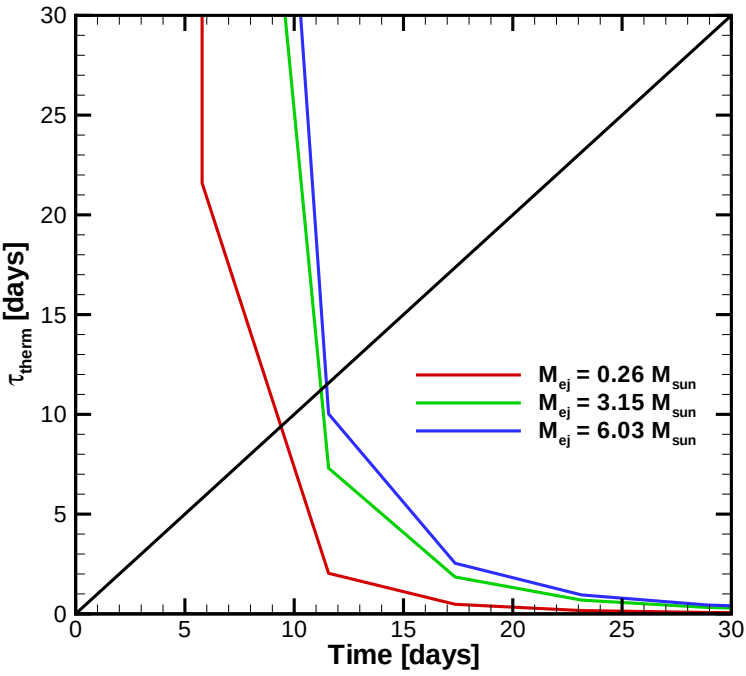

Figure 4.10: Estimated values of the thermal time scale of the optical thick part of the SN ejecta, assuming complete ionization, as a function of time. The line where the thermal time scale and the simulation timescale are equal is shown in black. The intersection between the thermal timescales for each of the different ejecta mass models and the black line yields an approximate value for the end of the plateau phase of the SN (also shown in Fig. 4.11).

(Chevalier 1987, Weiler et al. 1990, Bietenholz et al. 2010), which is again similar to the values we have assumed in our models. Here again, the observed X-ray light curve shows a steeper decay (−2, −3 Houck et al. 1998, Temple et al. 2005), respectively, compared to our models.

In order to estimate the time over which these SNe would remain visible, we make use of the forward shock velocities and the length of the SAGB phases of the two dimensional models (Fig. 4.9). If we assume that the time during which these SNe remain visible is proportional to the length of the SAGB phase, scaled by the ratio of the forward shock velocity at the end of the simulation, to the wind velocity of the SAGB phase ($\tau_{\rm SN} = \frac{V_{\rm SAGB}}{V_{\rm fs}} \cdot \tau_{\rm SAGB}$), we find time scales of approximately 40, 300, and 600 years for the models with 0.26, 3.15, and 6.03 $M_\odot$ of SN ejecta, respectively. The luminosity will not remain constant over this long period, but would remain relatively high compared to other SNe. As before, we assumed a SAGB wind velocity of 20 km s^{-1}. For comparison, if a SN had an energy output of 10^{51}erg, but the SAGB wind velocity was only 5 km s^{-1}, the above numbers

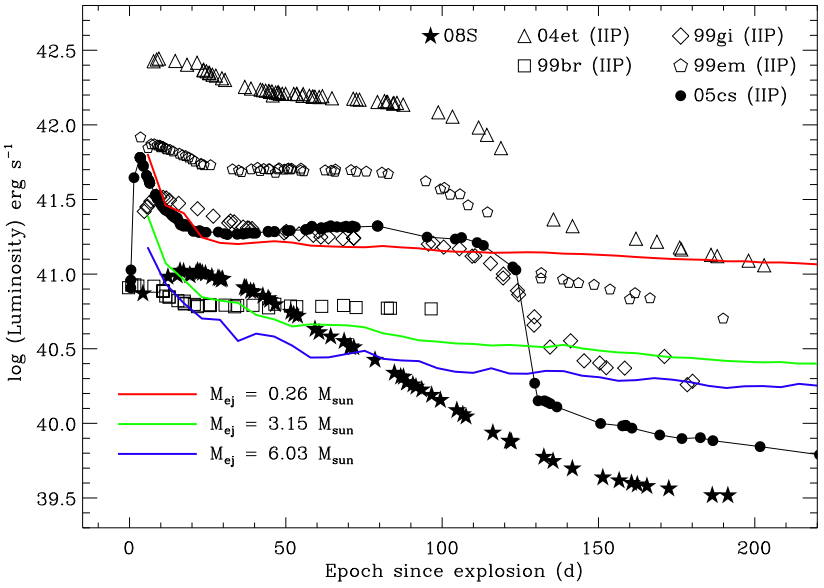

Figure 4.11: Light curves computed from the 2D models described in Section 4.4, compared to the quasi-bolometric light curves of a sample of type II-Plateau SNe and SN 2008S. As the shock radius increases inversely with ejecta mass, the lowest ejecta-mass model interacts with the largest amount of CSM, resulting in largest amount of energy being radiated away. For clarity, we only show the comparison up to a few weeks after the end of the observed plateau phase. The slope of each of the model light curves remains fairly constant until ∼1000 d, the nominal end of our simulation period. Following the end of the plateau phase, the observed light curves exhibit decline rates in line with that expected from the decay of ^{56}Co. Data for SNe 1999em, 1999gi, 1999br, 2005cs, 2004et, and 2008S have been taken from Elmhamdi et al. (2003), Leonard et al. (2002a,b), Pastorello et al. (2004, 2009), Maguire et al. (2010), and Botticella et al. (2009), respectively.

would change to 3, 24, and 50 years approximately. This is easily understood, because changing the velocity of the wind during the SAGB phase results in changes in the CSM density. Nevertheless, we expect a high luminosity during the time when the interaction is ongoing, even if we assume a higher explosion energy and a significantly lower SAGB wind velocity.

In principle, the magnitude of the observed ejecta velocities and the evolution thereof are probes of the explosion energy and the density structure of the ejecta / CSM. In Fig. 4.12 we show a comparison between the model reverse shock velocities, and a subset of the sample of the SNe shown in Fig. 4.11, for which measurements of the evolution of the photospheric velocities are available. The observed velocities for the IIP SNe shown are obtained from measurements of the P Cygni absorption trough of the Hα line. For SN 2008S which did not display P Cygni profiles at any point during the 15–256 d spectroscopic evolution reported in the literature, but which showed a multi-component Hα profile consisting of at least

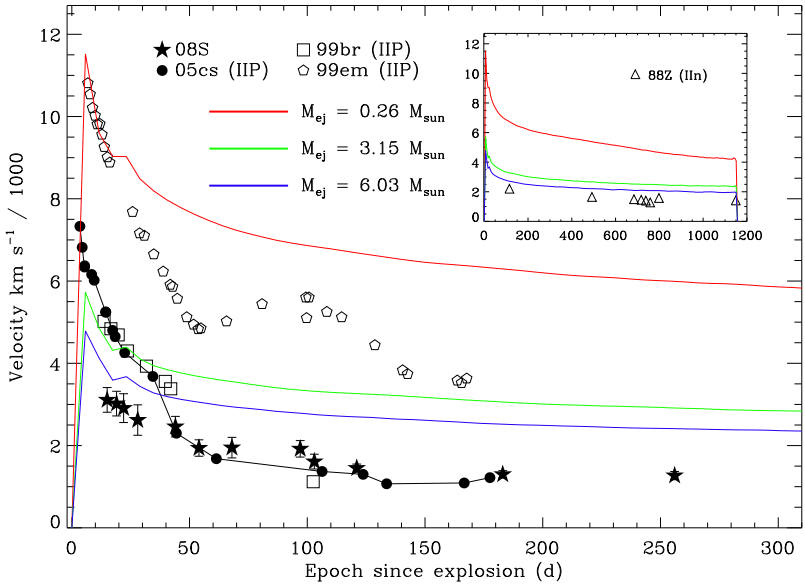

Figure 4.12: Reverse shock velocities for each of our three representative models compared with measured photospheric velocities for a sample of IIP SNe and SN 2008S. The data are from the same sources as in Fig. 4.11. The inset shows the velocity evolution of the intermediate Hα component of SN 1988Z, with the values taken from Turatto et al. (1993).

two components at all observed epochs, the velocities shown in Fig. 4.12 are those of the broad Hα component reported in Table 11 of Botticella et al. (2009). It is well known that the velocities derived from measurements of the Hα profiles generally overestimate the photospheric velocity with measurements of weaker lines such as Sc II generally being better trackers of the photospheric velocity. However, given that measurements of Hα velocities are more readily available, and that uncertainties in our model assumptions are likely to be a far greater cause of uncertainty than differences in photospheric velocity measurements from different spectral lines, we choose to show measurements from the same spectral line for all objects. As pointed out in Botticella et al. (2009), the broad Hα may not even reflect the ejecta velocity with the broad wings resulting from electron scattering. Note also that while the group of sub-luminous IIP SNe display similar spectral features and characteristics when compared to the garden variety of IIP SNe, SN 2008S shows marked deviations, even though some similarities do exist e.g. the agreement in the velocity evolution post-~40 d.The simulations show that the reverse shock velocity is an adequate approximation for the average velocity of the shocked material.

Both SN 2008S and NGC 300-OT were observed to have a narrow component to the Hα profile of between $\sim$ 150 – 300 km s^{-1} (Botticella et al. 2009, Berger et al. 2009). In order to ascertain whether such a narrow line might arise naturally in our models, we performed the following check. We assumed a fully ionized

CSM consisting solely of hydrogen, which begins to recombine. The ionization may have come from the initial flash of the SN, from the luminosity generated by the interaction of the SN with the CSM, or some combination of both. (2 asides: note that the bolometric output usually exceeds the flash in terms of energy; the narrow line is present at all epochs, including the earliest). Equation 5.2 in Dyson & Williams (1997) gives the recombination rate as a function of the number density and electron temperature. If we assume that the CSM density is shaped by a free-streaming stellar wind with an r^{-2} density profile, we can calculate an upper limit to the luminosity of the narrow Hα line, if we assume that every recombination also results in one Hα photon.

$$L_{\mathrm{H}\alpha} = \epsilon_{\mathrm{H}\alpha} \int_{R_i}^{R_o} 4\pi r^2 N_{\mathrm{rec}} \mathrm{d}r = \epsilon_{\mathrm{H}\alpha} N_{\mathrm{tot}} \tag{4.7}$$

where $L_{\mathrm{H}\alpha}$ is the luminosity of the narrow Hα line in erg s^{-1}, $\epsilon_{\mathrm{H}\alpha}$ is the energy of the Hα photon in erg, R_i and R_o are the inner and outer radius of the ionized region in cm, N_{rec} is the recombination rate in units s^{-1} cm^{-3}, and N_{tot} is the total recombination rate in units of s^{-1}. The requirement for the r^{-2} density profile certainly holds for the inner $\sim$ 1.5 pc of our simulations. At larger radii the density is lower, so the value of $\mathrm{L}_{\mathrm{H}\alpha}$ yielded from the calculation above should be considered an upper limit. Combining Equation 4.7 with equation 5.2 of Dyson & Williams (1997) and the assumption of a r^{-2} density profile gives:

$$N_{\mathrm{tot}} = \frac{L_{\mathrm{H}\alpha}}{\epsilon_{\mathrm{H}\alpha}} = \frac{2 \cdot 10^{-10}}{4\pi} T_\mathrm{e}^{-3/4} \left(\frac{\dot{M}}{m_\mathrm{h} v_\mathrm{w}} \right)^2 \left(\frac{1}{R_\mathrm{i}} - \frac{1}{R_\mathrm{o}} \right) \tag{4.8}$$

where T_e is the electron temperature in K, $\dot{M}$ and v_w are the mass loss rate and wind velocity, in g/s and cm/s, corresponding to the r^{-2} density profile and m_h is the mass of hydrogen in g. Solving Equation 4.8 for R_o, we find a requirement for R_i which has to be met to be able to obtain a solution.

$$R_\mathrm{i} < \frac{2 \cdot 10^{-10} \cdot \epsilon_{\mathrm{H}\alpha}}{4\pi L_{\mathrm{H}\alpha}} T_\mathrm{e}^{-3/4} \left(\frac{\dot{M}}{m_\mathrm{h} v_\mathrm{w}} \right)^2 \tag{4.9}$$

This tells us that the inner boundary of the region that is needed to explain an observed luminosity of the narrow Hα line has to be smaller than the value obtained from Equation 4.9. The closer R_i is to this value, the larger R_o has to be in order to explain the Hα luminosity. Note that for this entire region, an r^{-2} density profile is assumed.

This radius requirement can also be interpreted as the maximum radius the forward shock of the SN could have to be able to explain an observed narrow Hα line following the explosion. The result of this calculation is shown in Figure 4.13 for different values of the observed Hα luminosity. On the right y-axis the figure also shows the maximum time after the SN explosion that this narrow Hα line would be visible for, assuming an average forward shock velocity of 10000 km s^{-1}.

We also used Equation 4.8 to estimate the Hα luminosity which could be observed for our models. By putting in the forward shock radius for R_i and assuming R_o was small enough to be neglected, we can calculate the maximum Hα luminosity that could be observed, given the same assumptions as used to derive the

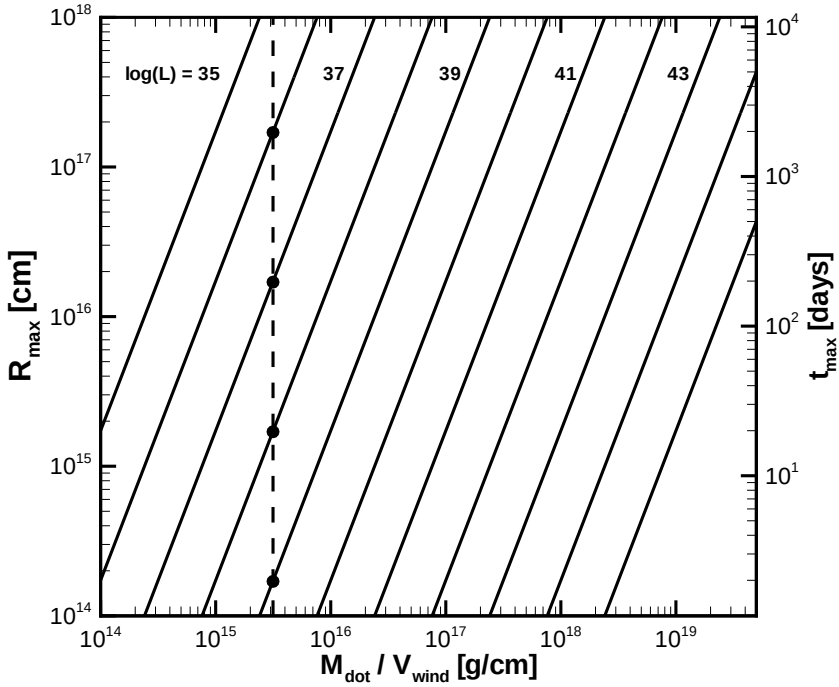

Figure 4.13: For different observed luminosities of the narrow Hα line, the solid lines show the maximum radius the forward shock can have before it is no longer possible to observe the narrow Hα line, as a function of the wind parameters $\dot{M}$ and v_w (which determine the r^{-2} density profile). The right hand y-axis shows the maximum time the narrow Hα line would be visible if we assume an average forward shock velocity of 10000 km s^{-1}. The dashed vertical line shows the value of $\frac{\dot{M}}{v_w}$ corresponding to the SAGB wind, with the dots marking the intersections between the solid and dashed lines.

above equations. Already after ~50 days the maximum Hα luminosity that can be observed in any of our models is below 10^{38} erg s^{-1}.

4.6 Summary

Based on the time evolution of stellar evolution models including the super-AGB phase, we modelled the pre-explosion circumstellar medium of ecSN, and the interaction of the resulting SN ejecta with this medium, using 1D and 2D hydrodynamic simulations. We obtained the interaction luminosities as function of time, and find the forward shock to produce mostly X-ray emission, while the reverse shock in our models is mostly radiative and may produce optical photons. Our 2D models show highly unstable contact discontinuities, and while these instabilities remain partly under-resolved, we find them to enhance the optical emission considerably.

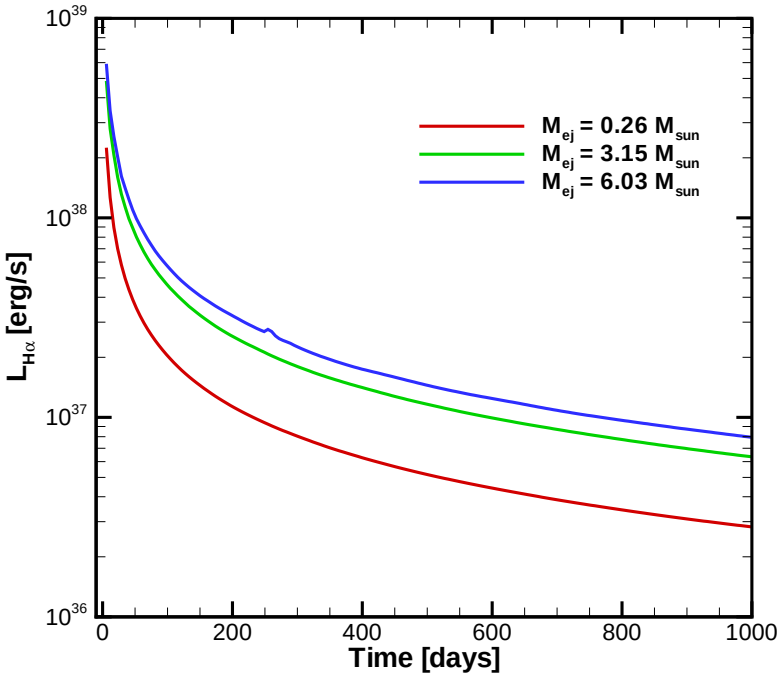

Figure 4.14: Maximum Hα luminosity in the narrow emission component for the three 2D models calculated with help of Equation 4.8. This number decreases with time due to the increase in the forward shock radius. The lowest mass model has the largest forward shock radius and therefore the lowest Hα luminosity.

Our models predict the behaviour of ecSN to depend sensitively on the remaining envelope mass in the SN progenitor at the time of explosion. For a low envelope mass (0.26 $M_{\odot}$), the ejecta speed is quite high ($\sim$ 8000 km/s) in spite of the assumed low explosion energy of 10^{50} erg. This results in a bright (several 10^{41} erg/s) and potentially long-lasting interaction phase. The reverse shock velocity, which may correspond to expansion velocity measured in optical spectra, is of the order of $\sim$ 5000 km/s. Our models with higher envelope masses produce slower velocities (2000...3000 km/s for both, forward and reverse shock), and while the interaction luminosity is not as high as in the case of a low envelope mass, it remains above 10^{40} erg/s for more than 3 years for the two lower SN ejecta mass simulations and for roughly 2 years for the simulations with 6.03 $M_{\odot}$ of supernova ejecta. We also provide a simple fitting formula that predicts the average luminosity of ecSNe during the first few years for different explosion energies and pre-supernova wind parameters, based on a grid of 1D-models (Eq. 5).

While our models do not include the thermal SN energy, we can estimate that their plateau phase may be quite short, i.e. of the order of two weeks. While we

do not attempt to estimate the luminosities during the plateau phase, they might be quite high due to the very large radii of the SN progenitors ($\sim 1000\,R_\odot$). After this short plateau phase, the interaction luminosity is likely the dominant contribution of the light curve, as the nickel production of ecSN is presumed to be very low (Kitaura et al. 2006).

While our method does not allow us to predict any quantitative information about the spectral appearance of ecSNe, we do estimate the Hα luminosity in a narrow emission component due to hydrogen recombination in the circumstellar medium (ignoring excitation from the X-rays produced by the forward shock). We find the narrow Hα luminosity to start out at the level of 10^{39} erg/s, but to drop rapidly with time (Figs. 13, 14). Electron-capture supernovae observed very early might be classified as type IIn supernovae.

In Section 4.5, we compared our models to observations for a sub-set of type IIP supernovae as well as SN 2008S. We found that the luminosities predicted by our simulations were of the same order as the luminosities of the SNe with which we compared them. At later times the predicted light curves exceeded those of the observations, which are typically dominated by radioactive decay. Therefore, a potentially important point to bear in mind from an observational point of view, is that ecSNe should not be dismissed as low luminosity events on the basis of their low explosion energy. This is more evident when we make the comparison with the X-ray luminosities of SN 1988Z (a type IIn supernova), whose slow decline of the X-ray light curve is similar to the predictions we make. While a higher CSM density in SN 1988Z can be the cause of the quantitative difference we find, the qualitative similarity of the light curves is striking. Additionally, the drop in the observed radio emission could be linked to a change in the pre-supernova mass loss. If so, this change occurred roughly 10 000 years before the SN explosion, which again is tantalizingly similar to the length of the SAGB phase.

The comparison of the photospheric velocities in the observations with the reverse shock velocities in our models shows once more the similarity between both. Although it was not aiming to reproduce or fit any specific set of SN observations, we found that the results of our models showed several properties having similar behaviour when compared to the observations. Some of these SNe may therefore represent ecSNe.

Acknowledgments

We thank Michael L. Norman and the Laboratory for Computational Astrophysics for the use of ZEUS MP. This work was sponsored by the Stichting Nationale Computerfaciliteiten (National Computing Facilities Foundation, NCF) for the use of supercomputer facilities, with financial support from the Nederlandse Organisatie voor Wetenschappelijk Onderzoek (Netherlands Organisation for Scientific Research, NWO).

Chapter 5

Pulsating Red Supergiants as possible progenitors for type IIn supernovae

B. van Veelen, N. Langer, M. Cantiello and S.C. Yoon
To be submitted to Astronomy & Astrophysics

Recent observations of type IIn supernovae have inspired ideas concerning enhanced stellar winds or even eruptions of massive stars shortly before they explode. We investigate the influence of a pulsationally driven super wind (PDSW) during the red supergiant phase, as recently suggested, on the circumstellar medium evolution of a $\sim$20 $M_\odot$ star prior to its supernova explosion. Subsequently we investigate the interaction of the supernova ejecta with the circumstellar medium to look for possible signatures of type IIn supernovae. We perform two-dimensional hydrodynamical simulations using ZEUS MP. We first compute the CSM evolution during the red supergiant phase, using the output of stellar evolution calculations which include a PDSW stage. Then, we model the supernova explosion into this CSM structure. By choosing three different times at which the supernova explodes, we mimic somewhat different timings between the pulsational mass ejection and the supernova explosion, which may relate to slightly different initial masses. A supernova explosion at the peak of the PDSW phase, where the supernova expands in a very dense stellar wind, produces a bright interaction supernova radiating at a level of several 10^{41} erg/s for several years. During the first one or two months, our models indicate the occurrence of narrow Hα emission with a luminosity of about 10^{39} erg/s. The models in which the supernova occurs 4 000 yr or 60 000 yr after the end of the PDSW phase show enhanced emission several years after the supernova outbursts, however, at a significantly lower level of up to 10^{38} erg/s. When the forward shock hits the dense circumstellar shell produced by the PDSW phase, it slows down significantly, which temporarily leads to close proximity of forward and reverse shock, a feature which has been assigned to to cosmic ray acceleration and/or hydrodynamical instabilities in some observed young supernova remnants.

5.1 Introduction

Type IIn supernovae are characterized by the occurrence of a narrow Hα emission line in the supernova spectra, which is indicative of a dense hydrogen-rich circumstellar medium (CSM). The type IIn supernovae do not form a homogeneous class. Since the narrow Hα emission line, which is required for the classification, comes from the unshocked circumstellar medium, the underlying supernova could even be of any type. An example is SN2002ic, which seems to be a hybrid Ia/IIn supernova (Hamuy et al. 2003). Since type IIP explosions are the most common type of supernova explosion, it is reasonable to search for possible progenitors of type IIn supernovae among the red supergiants (RSG).

Both, Smartt (2009) and Smith et al. (2010) find that the observed number of type IIP explosions can be accounted for when a initial mass range of 8.5-16.5 $M_{\odot}$ is considered. Stellar evolution calculations however show that stars with an initial mass as high a 25 $M_{\odot}$ might explode as type IIPs (Schaller et al. 1992, Meynet et al. 1994, Hirschi et al. 2004). A possible way to understand this discrepancy is to consider a very strong mass loss towards the end of the RSG evolution (Heger et al. 1997). While most stellar evolution calculations apply the mass loss prescriptions from de Jager et al. (1988) (JNH88) for the RSG stage, Yoon & Cantiello (2010) (YC10) describe a mechanism in which pulsations in the envelope of a RSG become increasingly strong and cause a Pulsationally Driven Super Wind (PDSW). They find that the mass loss during the PDSW phase might be strong enough to blow away a large part of the envelope before the supernova explosions occurs. This mechanism would result in a decrease in the number of type IIP explosion at higher masses. YC10 find the critical mass, above which no type IIP explosion would occur, to drop to from 25 $M_{\odot}$ to approximately 20 $M_{\odot}$.

In this paper we investigate what the influence of the PDSW is on the CSM and on the interaction of the supernova ejecta with the CSM. We use a detailed model of YC10 as input for our CSM modelisation, and investigate the emission produced by the supernova interaction. We also estimate the strength of narrow Hα emission lines. The layout of this paper is as follows. In Section 5.2 we describe the stellar evolution calculations that were used to investigate the evolution of the CSM under the influence of the stellar wind. We describe the numerical methods of the calculations in Section 5.3. The resulting structure of the CSM at different times during the evolution of the star can be found in Section 5.4, while in Section 5.5 we describe the interaction of the supernova ejecta with the evolved CSM for three different models, and compare our results with observations. Finally we discuss and summarize our results in Section 5.7

5.2 Stellar evolution models

As input to our hydrodynamical calculations we have used the mass loss history of a 20 $M_{\odot}$ star evolved including the effects of a PDSW during the RSG phase. The evolutionary calculation corresponds to the 20 $M_{\odot}$ model described in YC10. This is a model of a non-rotating massive star that is evolved including a wind enhancement during the RSG phase induced by strong pulsations. In fact, non-rotating massive stars above $\sim$ 17 $M_{\odot}$ are unstable to strong pulsations when the

temperature in the envelope decreases below $T \sim 10000$ K and the ratio of luminosity to mass (L/M) is sufficiently high (see Heger et al. 1997, YC10). This is due to H-recombination, which increases the opacity in the extended outer layers of the star. Using their code, YC10 studied the pulsational properties of unstable RSGs, and obtained a relation for the pulsation growth-rate η as function of the stellar structure. Then they assumed that the mass loss rate of a supergiant is significantly enhanced compared to the rate of JNH88 if pulsations are strong enough to be detected with their hydrodynamic stellar evolution code, i.e. if the pulsation growth-rate η is bigger than 1. During the RSG phase they used the following mass loss prescription:

$$\dot{M} = \eta^{\alpha} \dot{M}_{\mathrm{JNH88}}, \tag{5.1}$$

where $\dot{M}_{\mathrm{JNH88}}$ is the mass loss rate of JNH88, η is given in Equation 1 in YC10 and α a free parameter which is set to 1.75. While the physics of the pulsationally enhanced mass loss in RSGs is not well understood, it may be mentioned that, in principle, mass loss rates as high as 10^{-2} $M_{\odot}$ yr^{-1}are energetically possible, assuming terminal wind velocities of the order of the escape velocity from the stellar surface.

The evolution in the Hertzsprung Russell (HR) diagram of the 20 $M_{\odot}$ star including this mass loss prescription is shown in Figure 5.1. The corresponding values of mass loss and wind velocity as function of time are given in Figure 5.2. The wind velocity is calculated with help of the semi-empirical Equations 1 and 2 in Eldridge et al. (2006). This formulation gives a value for the wind velocity based on the escape velocity of the star, modified by the luminosity and effective temperature.

As the star evolves past H-core burning, it expands and reaches the red supergiant stage. In this phase the star becomes unstable to pulsations and the mass loss rate increases according to Equation 5.1. As the star gradually loses mass, the ratio L/M increases. As a consequence also the pulsation growth-rate η increases, resulting in a runaway process. This is shown in Figure 5.2, where the mass loss rate grows exponentially and reaches a peak at about $3 \cdot 10^{-4}$ $M_{\odot}$ yr^{-1}. This peak of the mass loss rate is attained when the helium mass fraction at the centre of the star decreases to 0.031, and the total mass to 6.90 $M_{\odot}$. As shown in Figure 5.2 the velocity of the PDSW is low, as the star is very extended in this phase. Eventually the mass loss decreases abruptly when the star moves toward the blue in the HR diagram, away from the region that is unstable to pulsations. This runaway increase of mass loss followed by rapid decrease can occur repeatedly as the star moves in and out the unstable regime (see Fig. 5.2). Note that the wind velocity can increase substantially when the star moves toward the blue and becomes more compact. The star finally ends its life as a yellow supergiant of $M_{\mathrm{tot}} = 6.1$ $M_{\odot}$, with only a small amount of hydrogen left (about 0.05 $M_{\odot}$).

As discussed by YC10, the PDSW occurs earlier in more massive stars, since these stars reach high values of the ratio L/M earlier in their evolution. While for the 20 $M_{\odot}$ model the peak of the mass loss occurs when the He mass fraction in the core is about 0.031, in the 25 $M_{\odot}$ model calculated by YC10 the PDSW phase occurs already when the He mass fraction in the core is about 0.54, and the peak in the mass loss takes place few hundred thousand years before core collapse (see

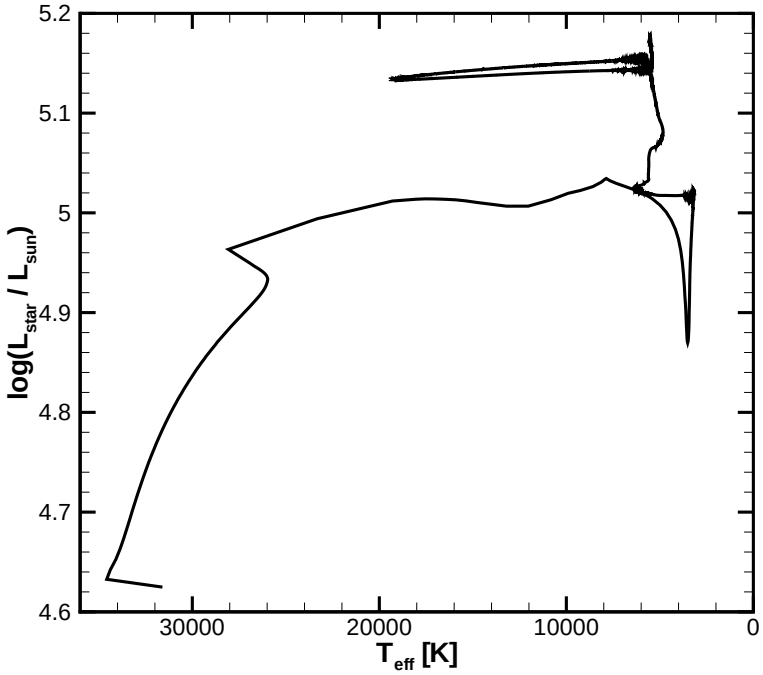

Figure 5.1: Hertzsprung-Russel diagram showing the evolution of the 20 $M_\odot$ model which is used as the bases of our hydrodynamic calculations, which experiences a pulsationally driven super wind (PDSW) during the RSG phase.

Fig. 4 in YC10). In lower mass models, the mass loss peak may thus be expected to occur later in the evolution, with the high mass loss present during the supernova explosion. In this paper, we therefor use the mass loss history depicted in Fig. 5.2, starting the supernova calculations at three different times (as indicated by dots in the figure), where the ones starting about 60 000 yr before the collapse of the 20 $M_\odot$model, — i.e. at the absolute peak of the mass loss, and shortly thereafter — might represent stars of slightly smaller initial mass.

5.3 Method

The stellar evolution model discussed in Section 5.2 is used as input for the simulations of the evolution of the CSM under the influence of the stellar wind. All simulations are performed with the three dimensional magneto hydrodynamics code ZEUS MP (Hayes et al. 2006).

Two separate steps are taken to simulate the interaction of the supernova ejecta with the CSM. First we perform a simulation of the evolution of the CSM due to the the stellar wind. We use the output at different times of this simulation as input

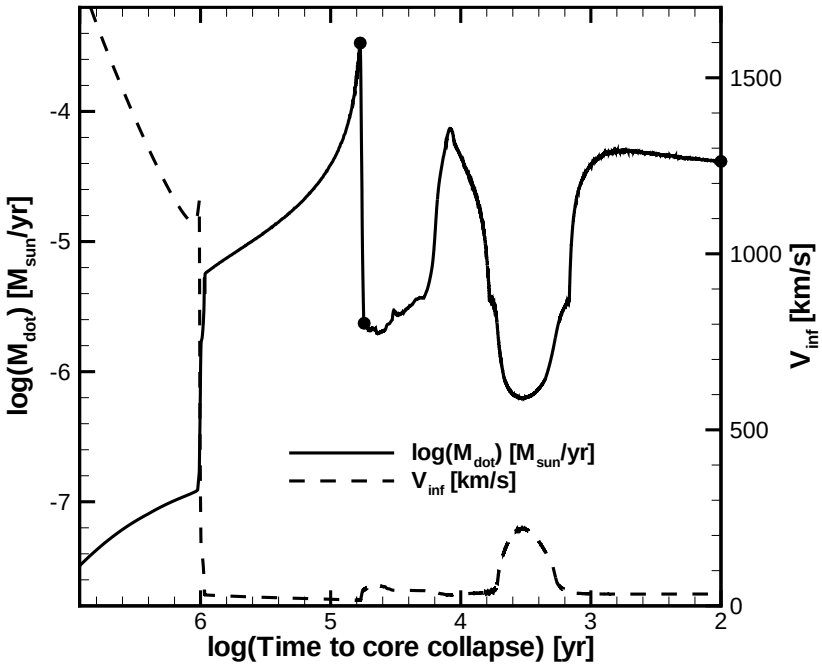

Figure 5.2: Mass loss rate and terminal wind velocity as a function of time until core collapse, for the 20 $M_\odot$ model displayed in Fig. 1. The dots represent the times at which we start the supernova simulations shown in Sect. 5.

for the second step. The second step is simulating the interaction of the supernova ejecta with the output of the previous simulation. By combining the output of three instances of the pre-supernova structure of the CSM at different times with three different supernova explosions, we obtain three models for the interaction of the ejecta with the CSM (see Table 5.1).

Table 5.1: Model parameters for the simulations of the supernova ejecta interacting with the CSM: Model number, the amount of time in the stellar evolution after the peak in the mass loss phase at which the supernova explosion occurs($\tau_{\rm SN}$), the supernova ejecta mass ($M_{\rm ej}$) and energy ($E_{\rm ej}$) and the time during which we follow the interaction of the supernova ejecta with the CSM ($\tau_{\rm post-SN}$).

Model	$\tau_{\rm SN}$ [yr]	$M_{\rm ej}$ [$M_\odot$]	E_{ej} [10^{51} erg]	$\tau_{\rm post-SN}$ [yr]
Model 1	0	5.4	1	2
Model 2	4 000	5.1	1	25
Model 3	60 000	4.6	1	500

The setup of the supernova ejecta was done in a similar fashion as described in

Whalen et al. (2008). We start with the following assumptions for the supernova ejecta:

$$\rho(v,t) = \begin{cases} F \cdot t^{-3} & \text{for} \quad v \leq v_{\rm core} \\ F \cdot t^{-3} \cdot (\frac{v}{v_{\rm core}})^{-n} & \text{for} \quad v_{\rm core} < v \leq v_{\rm max} \\ \rho_{\rm CSM} & \text{for} \quad v > v_{\rm max} \end{cases} , \tag{5.2}$$

$$v(r,t) = \frac{r}{t} \quad \text{for} \quad t > 0 \, . \tag{5.3}$$

Here t is the time, v is the velocity, ρ is the density and r is the radius. The normalization constants F and $v_{\rm core}$ are are determined by making use of the assumed SN explosion energy and ejecta mass. The maximum velocity ($v_{\rm max}$) is set to $3 \cdot 10^4$ km/s, which roughly corresponds to the maximum observed velocity in core collapse supernovae. The supernova explosion energy is assumed to be kinetic. The value for the exponent n is set to 9 for all simulations, which is a number that is usually assumed for core collapse supernovae (Truelove & McKee 1999, Dwarkadas 2005, Chugai & Chevalier 2006).

The density and velocity profile is set up in the inner 80% of the initial grid. To be able to maintain a high resolution at all times during the simulation we have made use of the expanding grid option in ZEUS MP. This method checks the radial velocity of the outer 10% of the grid and expands the grid according to the maximum velocity found, while keeping the number of cells constant. In this way the forward shock remains within the grid at all times. For a more detailed description regarding the setup of the supernova ejecta and the expanding grid we refer the reader to Whalen et al. (2008).

All the simulations were performed in spherical geometry in two dimensions, with an assumed symmetry in the φ direction. In the angular (θ) direction the number of grid cells for all simulations was equal to 320, ranging from 0 to $\frac{\pi}{2}$. The number of grid cells in the radial direction was always equal to 1000. For the pre-supernova simulation the outer radius was set to 1.4 pc. For the simulations of the supernova ejecta interacting with the CSM the initial outer radius was set to 10^{14} cm. The final outer radius of those simulations depends on the specific expansion of the supernova ejecta and is therefore different for each simulation.

Energy losses due to radiative cooling were also included, with help of a cooling curve that Smith et al. (2008a) calculated for a gas of solar metallicity and a number density of 1 cm^{-3}. We use the energy losses due to radiation to construct light curves for our models. We assume optically thin cooling, which says that all energy lost by the gas in the form of radiation is not absorbed at a later time and therefore does not contribute any more to the hydrodynamic calculations.

5.4 pre-supernova CSM evolution

Figure 5.3 shows the structure of the CSM close to the star for all three models, at the time of the assumed supernova explosion. Although the simulations were performed in one and in two dimensions, we chose to show the 1D results, since we found very little difference in both calculations, due to the lack of hydrodynamical instabilities which could break the spherical symmetry.

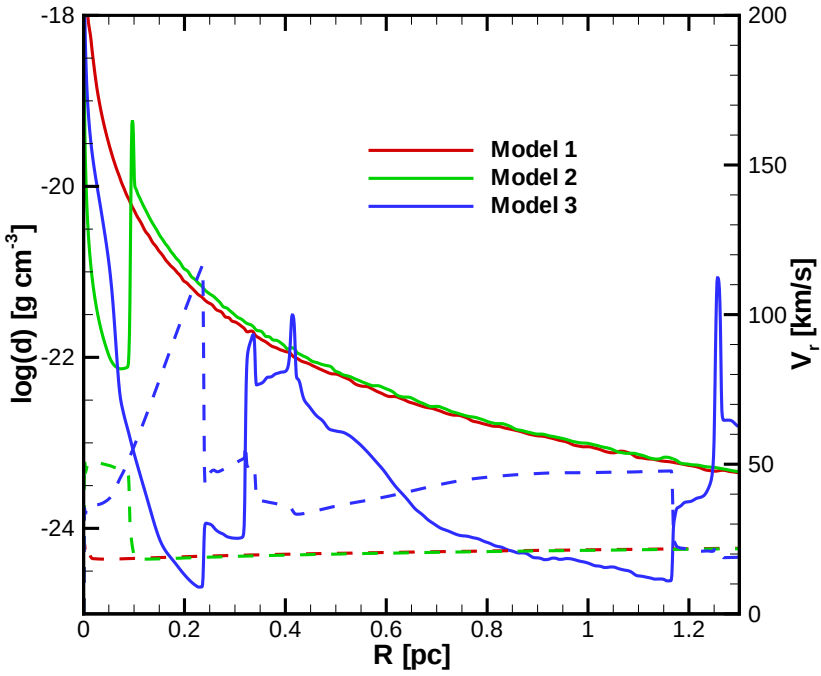

Figure 5.3: Pre-supernova CSM density (solid) and velocity (dashed) at the assumed times of the supernova explosions for our three models. At the peak of the RSG mass loss (Model 1; at approximately 8.45 Myr after the start of the main sequence), the density structure closely resembles an r^{-2} profile with a constant velocity. About 4000 years later (Model 2), the mass loss rate had gone down and the velocity had increased, causing a shell to be formed which is now located at a distance of about 0.1 pc. In Model 3, some 56 000 yr later, this shell has reached a distance of about 1.25 pc, while more shells have formed closer to the star due to several jumps in mass loss rate and wind velocity in the last few $\sim$ 10 000 years of the stars life (Model 3).

5.4.1 Model 1

At the end of the PDSW phase the CSM has an r^{-2} density profile with a constant velocity of approximately 20 km s^{-1}. Even though there is a strong peak in the mass loss rate at the end of the PDSW phase, the changes are not abrupt enough to create a shell at this point in time. Not shown in the plot is the CSM outside of 1.3 pc which contains the RSG shell and the MS shell. The RSG shell, which collects the RSG wind at the location where its ram pressure is balanced by the thermal pressure of the main sequence bubble, is located at approximately 9.5 pc from the central star, and the MS shell can be found at a distance of 52 pc.

5.4.2 Model 2

Approximately 4000 yrs after the end of the PDSW phase a shell has been formed due to the increase in the wind velocity from 20 to 50 km s^{-1}. As the faster wind is still relatively slow, the shell does not move outward at a high velocity. Also, the difference in the velocities is not high enough to cause hydrodynamical instabilities that might cause the shell to break up. Instabilities do occur when a star transitions from a RSG phase to a WR phase (García-Segura et al. 1996a).

At this point in time the shell contains approximately 0.4 $M_{\odot}$. At the peak of the PDSW phase, the mass contained within the region at which the shell currently is, is lower when compared to the mass of the shell. Again this is due to the low velocity difference between the two phases. A part of the material that was occupying the region within the current shell radius has had the time to move away from this region.

5.4.3 Model 3

At the very end of the evolution of the star, which provides the time of the supernova for Model 3, the shell created shortly after the end of the PDSW phase has moved out to almost 1.3 pc and now contains approximately 1.8 $M_{\odot}$. Two more shells have appeared, which can be seen around 0.35 and 0.45 pc. The first is a result of the jump in the mass loss rate approximately 10^4 yrs before the core collapse, while the second one results from the jump in the wind velocity somewhat later. The final phase, in which the mass loss rate increases prior to the core collapse, does change the innermost region of the CSM but this phase does not last long enough to create a shell. Inward of the innermost shell at 0.35 pc a region with a relatively flat density can be seen. This region has a very high temperature and is a region similar to the hot bubble created during the MS phase. Similar to Model 2, the jump in wind velocity which creates the innermost shell is not strong enough to cause instabilities in the shell.

5.5 Interaction of SN ejecta with the CSM

As a proxy for considering different progenitor masses we have chosen different times at which the supernova explodes. For the simulations of the interaction of the supernova ejecta with the CSM we have chosen different time scales over which we follow the interaction depending on the time at which the supernova explodes (see Table 5.1).

5.5.1 Model 1

In the first model the supernova explodes in a CSM which is shaped by the free streaming wind of the PDSW phase. The CSM has a density structure which roughly corresponds to a r^{-2} profile, similar to the models investigated by van Veelen et al. (2010 in prep.). In Figure 5.4 we show the light curve of Model 1 up to two years after the supernova explosion. The initial fast decrease is due to the decelerating forward shock and the decrease in the density of the material that

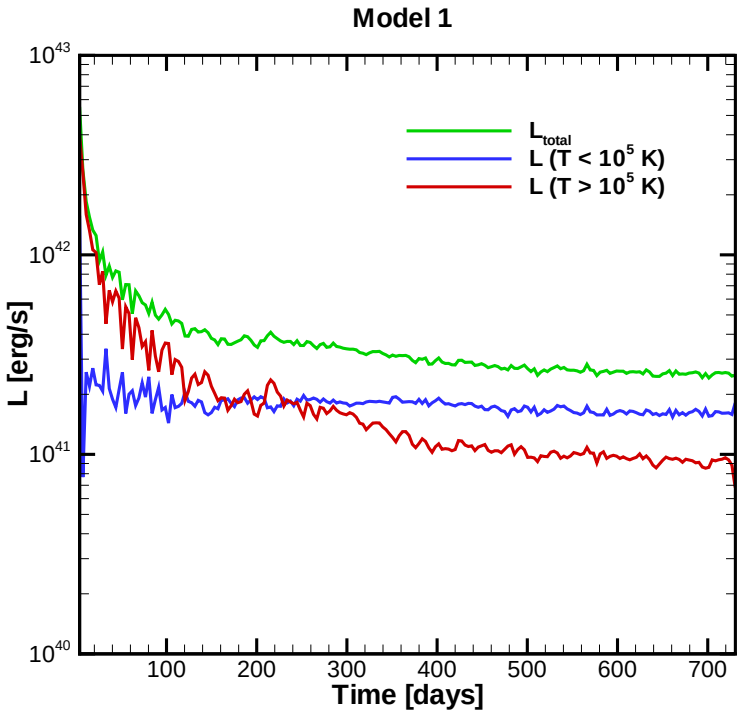

Figure 5.4: Light curves of Model 1. The green line shows the total emitted light coming from all the gas. $L_{\rm hot}$ and $L_{\rm cold}$ show the emitted light coming from gas above and below 10^5 K respectively. The total luminosity has a steep initial drop due to the forward shock decelerating, and it flattens because the forward shock velocity becomes rather constant. At late times, the cold gas is the dominating component of the emission, which indicates that the majority of the light may be emitted in the optical. Note that only the light from the interaction process is shown, while neither a possible plateau phase nor energy input from radioactive decay is computed here.

it encounters. After this initial fast decrease the light curve flattens. This behaviour is similar to what found by van Veelen et al. (2010 in prep.).

We have separated the light curve into two components, for light emitted by gas above and below 10^5 K. Since cooling is strong at 10^5 K, generally small amounts of gas are found with a temperature near this value, where the cooler component represents generally gas which as gone through a radiative shock, while the hotter component represents gas which as gone through an adiabatic shock. While the cool component may radiate most of its light in the optical regime, the gas of the hot component is generally so hot that it might predominantly produce X-ray emission. Initially the majority of the emitted radiation comes from the region behind the forward shock which is shocking the highest density material close to the star. Because the forward shock is not radiative, $L_{\rm hot}$ dominates shortly after the supernova explosion. At later times the radiation from the material shocked by the

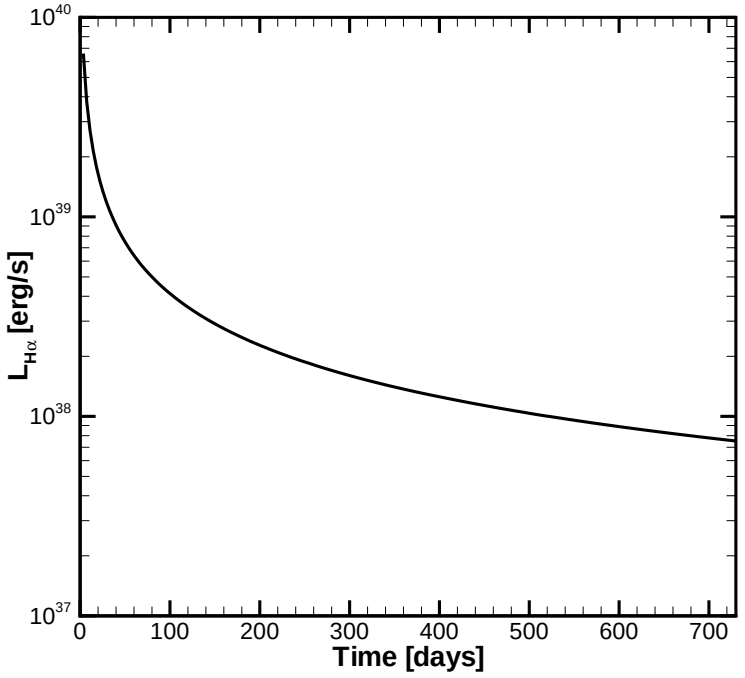

Figure 5.5: Estimated maximum Hα luminosity in a narrow emission component, for Model 1 as a function of time, calculated using Eq. (8) in van Veelen et al. (2010 in prep.). The decrease in the luminosity is a result of the increase in the forward shock radius.

reverse shock becomes increasingly important (see Figure 5.6), which is cooler, and therefore $L_{\rm cold}$ dominates. The material shocked by the reverse shock is accumulated into a cold dense shell which is unstable to the thin shell instability. This can be seen because this shell has broken up and is mixed with the region of hot shocked CSM, which causes an enhanced emission, as in the models of van Veelen et al. (2010 in prep.). Since $L_{\rm cold}$ dominates at late times, the majority of the light at late times will be emitted in the optical.

In this model the progenitor star still has a large part of its envelope and will therefore most likely explode as a type IIP supernova. To estimate the length of the plateau phase for this model we assumed that all material in the simulation is ionized. We then calculate at which radius the optical depth, due to Thomson scattering, is equal to 1. This was done by integrating from the outside inwards, starting just outside the forward shock. Assuming a temperature of 5000 K at the location where the optical depth is equal to 1, we can calculate a luminosity. Since we do not assume any recombination, the radius we find is an upper limit.

By using the calculated luminosity a thermal time scale can be defined; $\tau_{\rm therm} = \frac{E}{L}$, where E is the total thermal energy still remaining in the SN ejecta inward of the

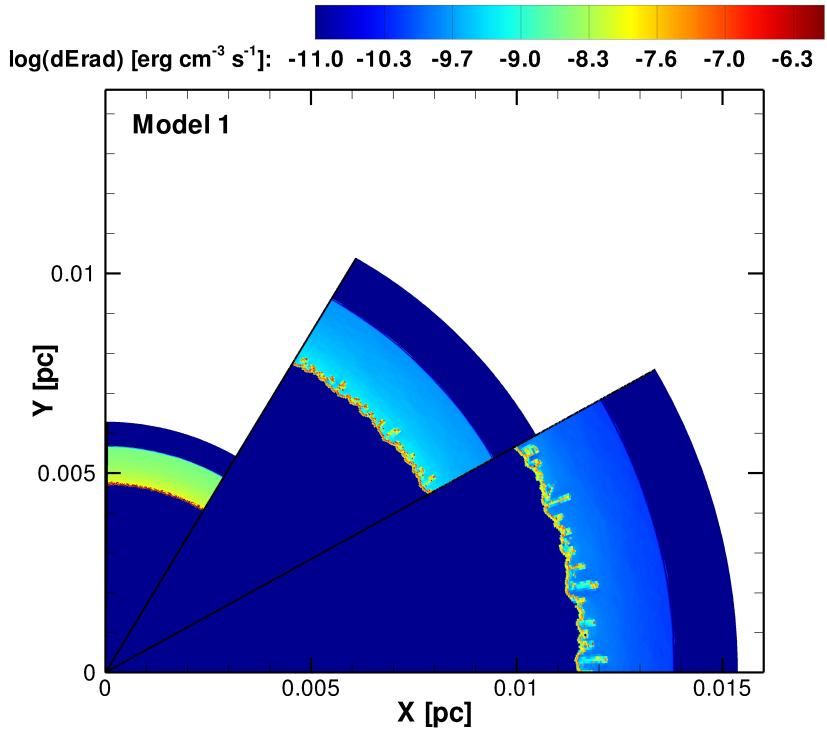

Figure 5.6: Emissivity of the supernova of Model 1; 256, 548 and 730 days after the SN explosion, moving clockwise. All the emitted light comes from the region between the forward shock and the reverse shock. The region between the reverse shock and the contact discontinuity was initially a thin dense shell, but has broken up due to the thin shell instability. The structure of the supernova does not change significantly over time due to the smooth CSM it is interacting with.

photospheric radius. The end of the plateau phase is then assumed to occur when the thermal time scales equals the time elapsed since the supernova explosion. With this method we estimated the length of the plateau phase to be 13 days.

Since the CSM has a r^{-2} density profile, we can estimate the luminosity in a narrow Hα emission component we might get from the flash-ionized CSM in the same manner as in van Veelen et al. (2010 in prep.). If we use their Eq. (8) and replace $R_{\rm i}$ by the forward shock radius as a function of time, we obtain the maximum possible Hα luminosity (neglecting secondary excitation) as function of time (see Fig. 5.5). Up to approximately 50 days, a luminosity of 10^{39} erg/s is possible, while a luminosity of 10^{38} erg/s can be seen until 500 days after the supernova explosion.

Note that the maximum Hα luminosity we get at any given point after the explosion is based on the assumption that the CSM is initially fully ionized. The Hα luminosity that is shown in Figure 5.5 also assumes that the value for the outer radius ($R_{\rm o}$) is set to infinity. However, if the outer radius would be set to twice the value

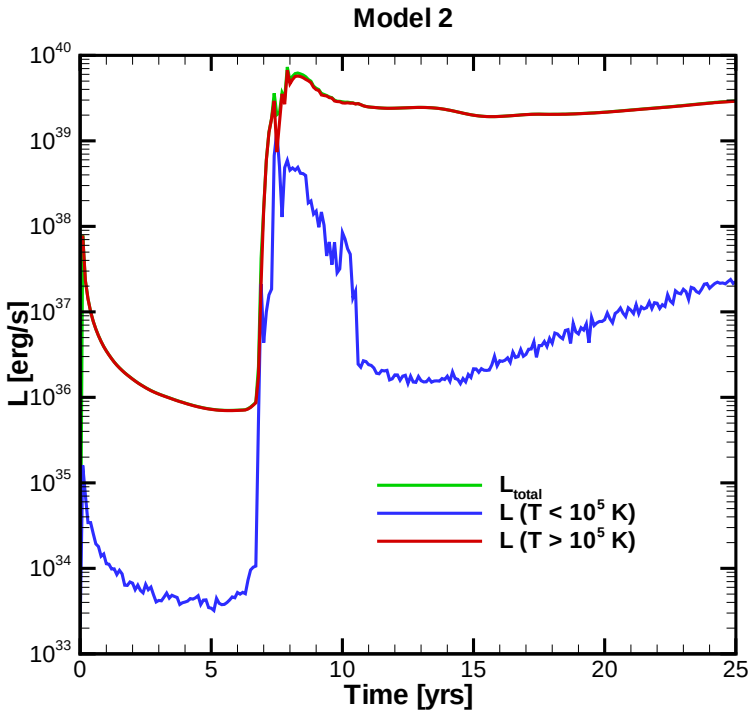

Figure 5.7: Light curves of Model 2, as in Figure 5.4. After a gradual decline following the explosion, the supernova rebrightens approximately 7 years later due the collision with the CSM shell (cf., Fig. 3). During this time the cold gas shows a significant contribution for a short time, due to a short period in which the forward shock is radiative. Note that the peak luminosity is about ten times lower than the luminosity found in Model 1 (Figure 5.4)

of the inner radius, the Hα luminosity would only decrease by a factor of 2.

The amount of energy that is needed to ionize 1 $M_\odot$ of hydrogen is equal to $2.6 \cdot 10^{46}$ erg. If we consider the region up to 0.03pc (which is roughly twice the radius of the forward shock at the end of the simulation), the mass contained within that region is approximately 0.5 $M_\odot$. Soderberg et al. (2008) found that the shock breakout of SN2008D already provided a burst in X-rays of $2{\cdot}10^{46}$ erg. Considering the fact that other wavelength bands would also contribute to the energy that will be used for ionization of the CSM, plus the fact that the interaction itself provides a high amount of ionizing flux, the assumption of a fully ionized CSM seem to be justifiable.

5.5.2 Model 2

In this model we look at the interaction of the supernova ejecta with the CSM containing a single shell. This shell was created by the sudden drop in the mass loss rate and the simultaneous increase in wind velocity after the PDSW phase. Similar

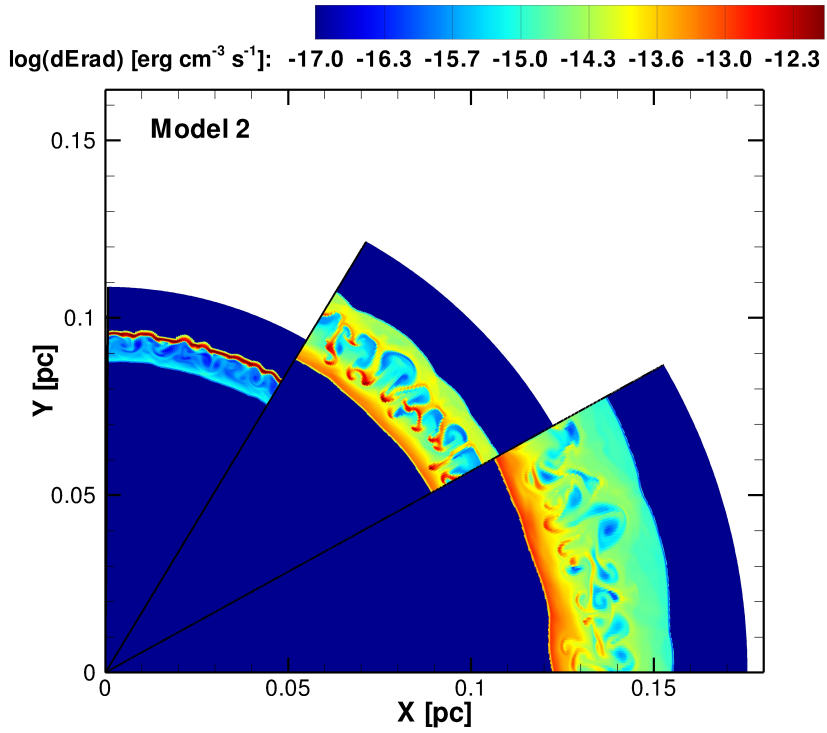

Figure 5.8: Emissivity of the supernova in Model 2; 10, 18 and 25 years after the SN explosion, moving clockwise. The first slice shows the supernova remnant shortly after the collision with the CSM shell, which is still radiating strongly at this point. The second slice shows that several years later the forward shock has overcome the shell and is now moving through the r^{-2} density structure of the CSM. The remnants of the shell are still visible as the strongly radiating clumps. In the final slice the region close to the reverse shock becomes more and more important in the radiative energy loss. This is not a result of a radiative reverse shock but due to the high density of the supernova ejecta that is shocked by the reverse shock.

to the previous model we have plotted the light curve and made the distinction between the hot and cold gas (see Fig. 5.7).

Compared to Model 1 the supernova ejecta initially encounters a lower density CSM, which allows the supernova ejecta to expand faster but also to emit less light. The interaction luminosity, especially of the cool gas, is so low that it will not contribute significantly to the supernova light. Even the luminosity of the hot gas decreases down to 10^{36} erg/s. At this point the supernova ejecta collides with the shell and a re-brightening occurs. The sudden increase in the density of the material encountered by the forward shock causes a short phase during which the forward shock is radiative. Therefore a sudden increase in $L_{\rm cold}$ occurs, which makes the interaction luminosity the dominant contribution to the supernova light at this late stage. It takes approximately 2 years for the forward shock to cross the dense shell. Then the shock accelerates again and becomes non-radiative once more. $L_{\rm cold}$ drops

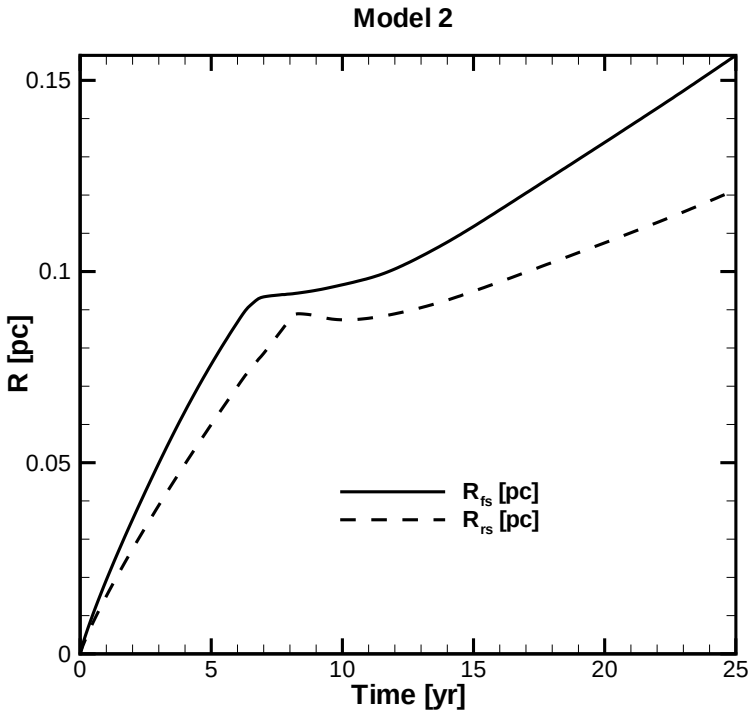

Figure 5.9: Forward (solid) and reverse (dashed) shock radius as a function of time. When the supernova ejecta collide with the shell, the forward and reverse shock come very close to one another for a short period of time. At later times, the reverse shock has decelerated (in the observers frame) due to the collision, while the forward shock is now plowing through the free streaming wind outside of the shell.

and the luminosity is dominated by the emitted radiation from the hot gas.

Intuitively one might expect that this case would give a higher luminosity when compared to Model 1, due to the energetic collision with the CSM. This is not the case, the luminosity of Model 2 never reaches the values obtained in Model 1, since the shocks remain mostly non-radiative in Model 2. The forward shock only becomes radiative once the supernova ejecta overrun them. In Model 1 the reverse shock is radiative during most of the time in the 2 year time span. This results in a higher rate of energy loss due to radiation. The fact that the total energy lost in Model 1 after 2 years is $2.6 \cdot 10^{49}$ erg, while the total amount of energy lost by Model 2 after 25 years is equal to $1.5 \cdot 10^{48}$ erg, emphasizes this result.

The evolution of the CSM structure at different times after the supernova explosion can be seen in Figure 5.8. In the first slice (counting clockwise), just after the collision with the shell, the majority of the light comes from the shocked shell. This shell is currently being broken up due to the density perturbations in the supernova ejecta. These perturbations originated from the thin shell instabilities that occurred

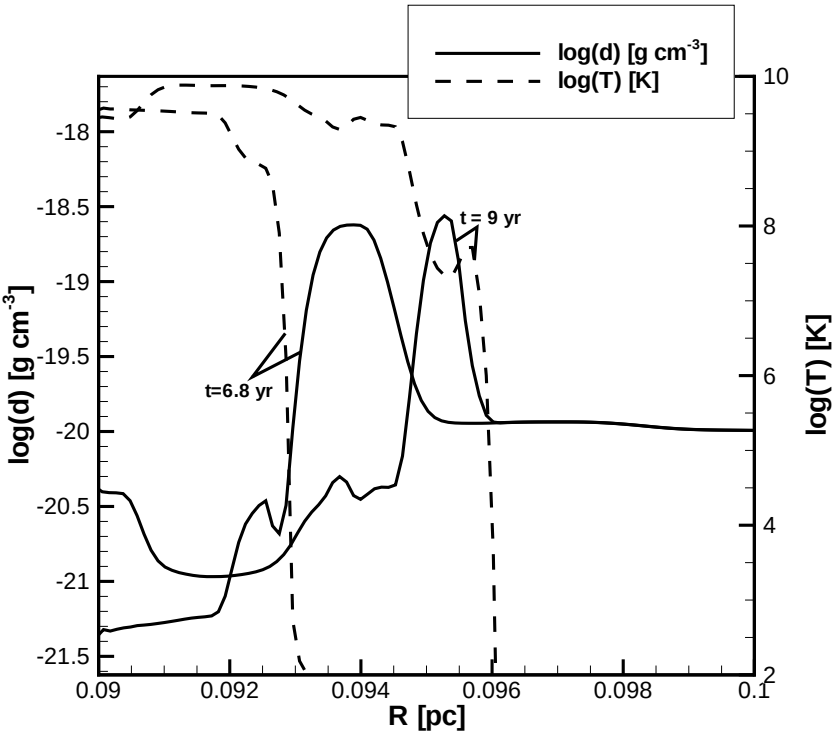

Figure 5.10: Density (solid) and temperature (dotted) of the CSM at two different times after the supernova explosion of Model 2. These lines show the forward shock sweeping over the thin shell. The strong drop in the temperature indicates the location of the forward shock. It takes roughly 2 years for the forward shock to completely sweep over the shell. While the inner part can already be shocked, the radiation coming from this shocked material might ionize the outer parts of the shell.

in the shell of shocked supernova ejecta between the reverse shock and the contact discontinuity. Several years later (second slice) the forward shock has moved past the shell, which can still be seen as the strongly radiating red clumps. Because these high density clumps contain a relatively large amount of mass with respect to their surroundings it is more difficult for the supernova ejecta to accelerate them. In the final slice, the remnants of the shell can still be distinguished. The reverse shock is non-radiative at this point but is shocking material with a high density, and therefore has a significant contribution to the total light emitted, presumably in the X-ray regime.

We show the radius of the forward and reverse shock as a function of time for Model 2 in Figure 5.9. Before the collision of the supernova ejecta with the shell, both the forward and reverse shock expand fast and remain relatively close to each another. The forward shock does not sweep up a significant amount of mass compared to the mass in the ejecta and therefore the reverse shock does not become very strong. After the collision with the shell the velocity of the forward

shock drops first, after which the reverse shock follows. The time delay between the deceleration of both shocks causes them to come as close as 0.005 pc from one another. Some time after the collision the gap between the two shocks widens again and the reverse shock begins to shock supernova ejecta at a faster rate.

To estimate if a narrow Hα line might be seen from Model 2 due to the ionization and subsequent recombination of the high density shell, we again made use of the recombination rate, Equation 5.2 in Dyson & Williams (1997). If we assume that the entire CSM is ionized and then assume that every recombination gives an Hα photon, we can estimate the Hα luminosity for a given density. If we then integrate this value over our shell we obtain an Hα luminosity. The integrated value is approximately $4 \cdot 10^{37}$ erg/s.

The ionizing flux can have two sources in this simulation. First, there is the ionizing flash that occurs during the supernova explosion. Secondly, the collision of the supernova ejecta with the shell can also give a high ionizing flux. From the lightcurve it can be seen that the luminosity has already increased to values above 10^{39} erg/s soon after the collision. Since it takes roughly 2 years to completely overcome the shell (see Fig. 5.10), the ionizing flux that arises due to the increasing luminosity is a possible source of ionization for the shell itself. Both instances of ionization do therefore predict the occurrence of a narrow emission component in the Hα emission line.

5.5.3 Model 3

In our final model we have evolved the CSM under the influence of the stellar wind towards the end of the stellar evolution model. The light curve for this model (Fig. 5.11) show several jumps that can be connected to the collisions with the shells in the CSM. After the collision with the first shell there is a short period in which the luminosity coming from the cold gas contributes significantly to the total luminosity. When the ejecta collide with the more massive second shell the reverse shock becomes non-radiative and the luminosity of the cold gas drops again. Although $L_{\rm cold}$ increases once more when the ejecta hit the third shell at approximately 1.3 pc, the increase is not strong enough to contribute significantly to the total luminosity.

The collision of the supernova ejecta with the CSM shells can be seen in the evolution of the forward and reverse shock radii (Fig. 5.12). The collision with the first shell can be seen as the sudden decrease of the forward shock expansion at ~20 years after the supernova explosion. Because the first shell contains a relatively small amount of mass the reverse shock does not show a reaction to the collision with the first shell. The collision with the second shell takes place around ~50 years. Since the forward shock was already decelerated at that point, there is no clear signature of this collision in the forward shock evolution. Similar to the previous model, there is a delay in the reaction of the reverse shock, which is only seen after ~70 years. The collision with the final shell ~150 years after the supernova explosion decelerates the forward shock once again. The distance between the forward and reverse shock also becomes smaller once again. This evolution clearly shows that relative radii of the forward and reverse shock change strongly as a function of time. Considering observations of young supernova remnants, a close proximity of forward and reverse shock might considered as evidence of a

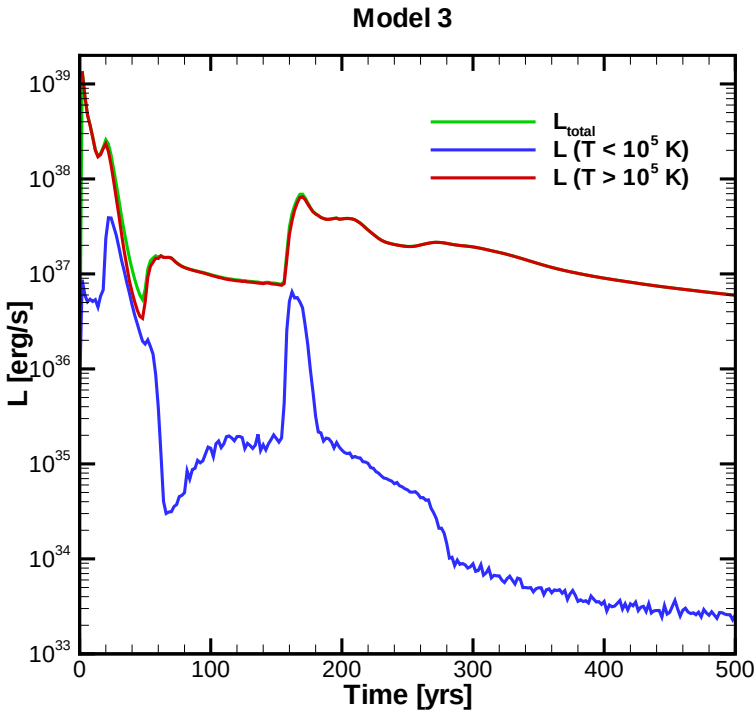

Figure 5.11: Lightcurve of Model 3, as in Figure 5.4. Around 20 and 50 years, the collision with the inner 2 shells (see Figure 5.3 around 0.4 pc) increases the luminosity, although not by much. This is a result of the small amount of mass contained within these shells. The collision with the shell at 1.2 pc is much more violent and creates a stronger rebrightening. Up to approximately 60 years, the cold material can still contribute at some points in time. At later times practically all the material in the supernova (remnant) has a temperature above 10^5 K.

recent interaction of the forward shock with a dense shell.

In Figure 5.13 we show the evolution of the emissivity of the supernova remnant at several points in time after the explosion. Three slices show the emissivity 240, 360 and 500 years after the supernova explosion, counting clockwise. In the first slice we show the time at which the ejecta has recently collided with the third shell (at ~1.3 pc) in the CSM. Since this shell contains a significant amount of mass compared to the mass in the supernova ejecta this collision creates a strong reflected shock. This shock can be seen between the forward and reverse shock with a high emissivity. The reflected shock moves inward with respect to the reverse shock and will eventually overtake it and become the 'new' reverse shock. In the next slice, 120 years later, the emissivity shows the remnants of the broken up CSM shell close to the forward shock and a shell consisting of shocked ejecta close to the reverse shock. These two shells show a similar emissivity at this point in time. After 500 years the emissivity in the shell of shocked ejecta has decreased and only the

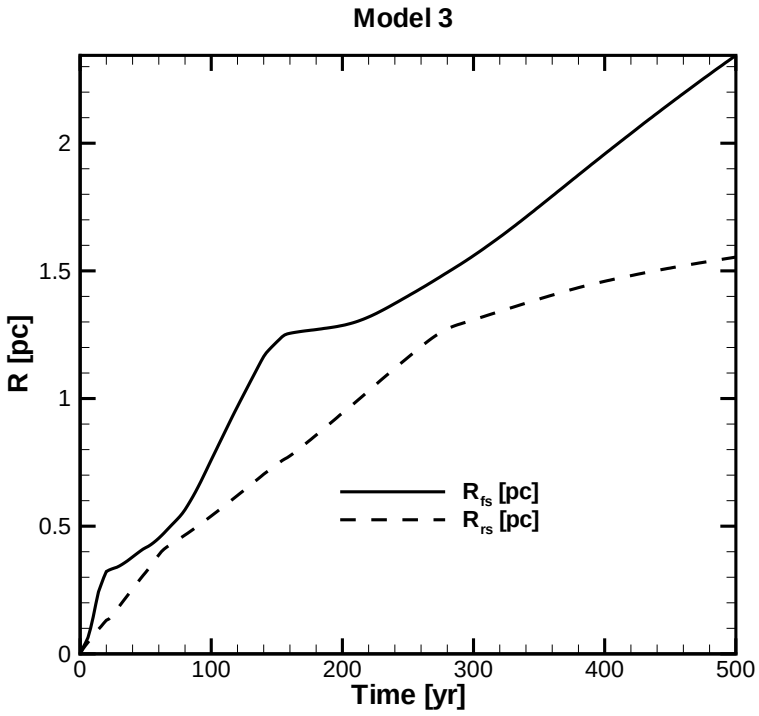

Figure 5.12: Forward (solid) and reverse (dashed) shock radii as a function of time. The shell collision around 20, 50 and 150 years cause a deceleration of the forward shock. The result is a strongly changing ratio between the forward and reverse shock radius at different points during the evolution of the supernova remnant.

remnants of the shocked CSM shell are still clearly distinguishable. The structure of the supernova remnant can take on largely different forms depending on the time of observation.

If we perform the same calculation as we did for Model 2 in the previous section, we obtain a luminosity in the narrow Hα emission line from the shells of $9.1 \cdot 10^{34}$ erg. This model is therefore not a likely progenitor model for type IIn supernovae.

5.6 Comparison with observations

5.6.1 Model 1

Since the CSM in this model is shaped by a free streaming wind, its analysis is performed similarly as those in van Veelen et al. (2010 in prep.). If we use the scaling relation (Eq. 5) from that paper and apply it to this model, with $\overline{v_{\rm ej}}$ equal to 4315 km s^{-1}, and v_∞ equal to 20 km s^{-1}, we obtain an average luminosity of

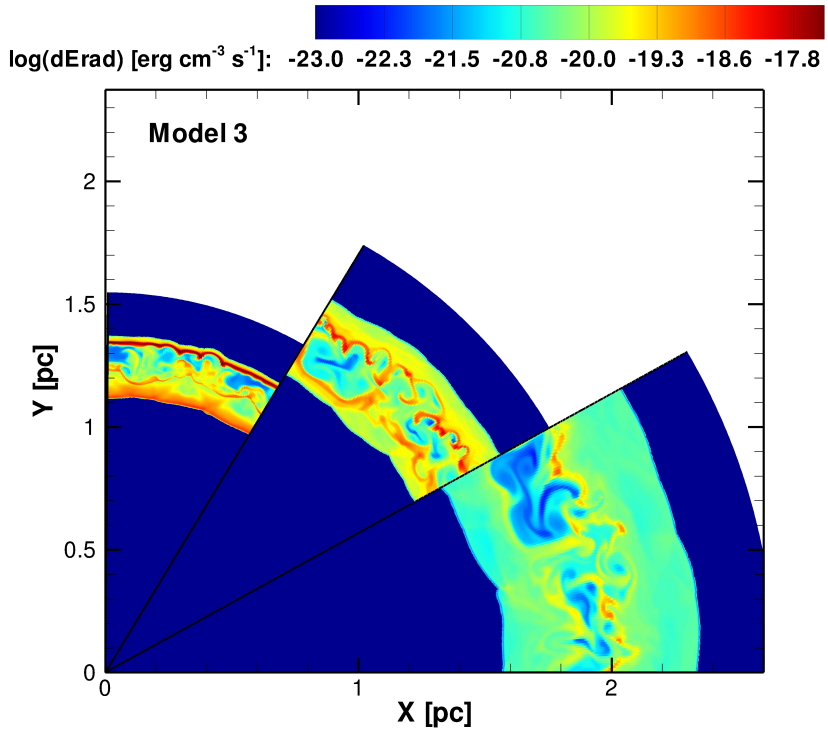

Figure 5.13: Emissivity of the supernova remnant of Model 3; 240, 360 and 500 years after the SN explosion, moving clockwise. The first slice shows the moment shortly after the collision with the outermost shell. Besides the forward and reverse shock, a third shock in between both can be distinguished. This shock is the reflected shock that was created when the supernova ejecta hit the shell in the CSM. After 360 years this reflected shock has overtaken the original reverse shock, and there are only two shock visible in the second slice. The two shells of shocked ejecta and shocked CSM have approximately the same emissivity at this point in time. In the final slice the most strongly radiating part of the remnant are the remainders of the shell.

$1.3 \cdot 10^{41}$ erg/s. Note that this value has been multiplied with a factor of 3, since the mass loss rate in this model is roughly a factor of 3 higher. The value we find from the 2D simulations of Model 1 is $3.1 \cdot 10^{41}$ erg/s.

In observed type IIn supernovae the emission in the narrow component is assumed to be coming from the undisturbed CSM which is being ionized by the emission coming from the supernova. In this model we have estimated the expected emission, given the r^{-2} density structure of the CSM. We find that up to about 50 days one could observe a narrow Hα emission line of 10^{39} erg/s. While some observations show higher values over a longer period of time (e.g Kotak et al. 2004, Aldering et al. 2006, Miller et al. 2010) the luminosity we find has been observed for type IIn supernovae at later times (Trundle et al. 2008).

The results of this model are similar to the observations of SN1998S, which was observed to have a high X-ray, radio and optical luminosity roughly 3 years

after the explosion (Pooley et al. 2002). While we predict a luminosity of the hot gas of $\sim 10^{41}$ ergs after approximately 2 years, the measured X-ray luminosity of SN1998S after 3 years was $\sim 10^{40}$ ergs. The slope α of the $L_{\rm hot}$ light curve ($L_{\rm hot} \propto t^{\alpha}$) over the last year in this model is approximately -0.7 . (Pooley et al. 2002) finds a somewhat steeper slope of -1.3. Note that $L_{\rm hot}$ is not necessarily equal to the X-ray light curve and that the times at which these slopes are calculated is different in the observations and in our model. The inferred mass loss rate of SN1998S was around 10^{-4} $M_{\odot}$ yr^{-1}, which is similar to the mass loss rate we have used during the PDSW.

Fransson et al. (2002) inferred that the type IIn supernova 1995N showed signs of interaction with a high density CSM creating unresolved narrow emission lines, including an Hα line, with a FWHM $\lesssim$ 500 km s^{-1}. The simultaneous high X-ray emission from this supernova (Fox et al. 2000) was most likely the ionizing source of the CSM. The inferred high density of the CSM led Fransson et al. (2002) to suggest that the progenitor star of SN1995N was comparable to the RSG VY CMa, which has a mass loss rates in the range of 10^{-4} $M_{\odot}$ yr^{-1} (Danchi et al. 1994).

At the peak of the PDSW phase, the star still has a significant fraction of hydrogen left in its envelope. If we would exclude the presence of a narrow Hα emission line we would expect the supernova explosion to be of type IIP.

5.6.2 Model 2

The light curve for Model 2 tells us that the interaction of the supernova ejecta with the CSM becomes strong enough to be observed after roughly 7 years. At this point the ejecta collide with the shell in the CSM and the supernova rebrightens. Rebrightening supernovae are hard to find since after the initial decline in the light curve, there is no longer an apparent reason to observe them. In some cases however, supernovae are seen to rebrighten years after the supernova explosion (e.g Bauer et al. 2008, Stockdale et al. 2004).

After roughly 2 years SN2004et showed signs of rebrightening in the MIR, NIR and optical (Kotak et al. 2009, Maguire et al. 2010). Interestingly Figure 4 in Kotak et al. (2009) also shows a late time (~823 days) appearance of a narrow Hα emission line. Similar to our results, this line could be coming from the shell in the CSM that was ionized by the radiation coming from the interaction with the supernova ejecta. In our results this emission feature can only be visible for roughly 2 years, at later phases the forward shock has overrun the shell completely and no recombination can take place any more.

Similar to the result of Model 1, the expected luminosity in the narrow Hα emission line is lower than some of the observed type IIn supernovae. In this case however, it might be easier to distinguish the emission line at late times when the amount of light coming from other regions of the supernova have decreased.

5.6.3 Model 3

Since the shells in Model 3 are further away from the center of the explosion it takes more time for the supernova ejecta to reach them. Only after decades does

the ejecta collide with the high density shells in the CSM. This model is therefore of more interest in light of supernova remnants (SNR).

A striking feature in the results of our model is the relative radius of the forward and reverse shock as a function of time. Depending on the time of observation the two shock can be very close to each other due to the collision with the CSM shells. For a comparison consider Tycho's SNR. Note that this supernova was most likely a type Ia explosion and we must be mindful of the comparison we want to make. Warren et al. (2005) concluded that the forward shock in Tycho was a site for cosmic ray acceleration due to the proximity of the contact discontinuity and the forward shock, among other observables. While we do not want to suggest that this is not the case nor want to suggest that our model is representative for Tycho's SNR, we merely want to emphasize that the occurence of a collision of the forward shock with a dense shell can have the same effect, a suggestion also made by Kosenko et al. (2010). The suggestion for a more complex structure of the CSM was also made by Dwarkadas & Chevalier (1998), whose models are better applicable with respect to Tycho's SNR. Hydrodynamical instabilities occurring in the interaction of supernova ejecta with a smooth CSM can also play an important role (Fraschetti et al. 2010).

5.7 Discussion and conclusions

In this paper we have investigated the influence of a pulsation-driven superwind (PDSW) occurring during the RSG phase on the surroundings of a star, and its effects on an ensuing supernova explosion. We have computed light curves for the emission due to the interaction of the supernova ejecta with the circumstellar medium, where we distinguish between hot gas emitting mostly in X-rays, and cooler gas emitting mostly in the optical range. By assuming flash-ionisation and subsequent recombination of the unshocked CSM, we derive limits on the luminosity emitted in a narrow Hα emission line component as function of time.

We emphasize that the details of the mechanism of pulsationally enhanced mass loss are far from fully understood. The prescription that was used in YC10 and employed here has large uncertainties, which in turn create large uncertainties in the mass loss rate and the time at which the PDSW occurs. The fact that, in the hydrodynamical stellar evolution models, the PDSW occurs earlier in more massive stars allows us to investigate three time differences between the peak of the PDSW and supernova outburst, i.e. their coincidence (Model 1), and a supernova 4 000 yr (Model 2) and 60 000 yr (Model 3) after the PDSW ended (Table 1).

For Model 1, we found that the optical emission due to the collision of the supernova with the dense progenitor wind remains rather constant at the high level of $2\,10^{41}$ erg/s for at least two years, and therefore become the dominant light contribution after a possible plateau phase ends. A narrow Hα emission line component with a rapidly decreasing luminosity could be observable during the first few weeks at a level of several times 10^{39} erg/s. In some observed supernovae, the narrow Hα luminosity is an order of magnitude higher, even at later times than 50 days. While we are not able to explain those observations with our specific models, we can account for a subset of the observations with lower luminosities. The un-

certainties in the prescription of the PDSW may leave room for even higher values of the mass loss, which would increase the density in the CSM, and consequently the narrow Hα luminosity. Alternatively, one might consider the an enhanced narrow Hα luminosity due to the CSM ionisation by high predicted X-ray luminosity (several 10^{41} erg/s during the first months) of the forward shock.

In Model 2, which features a supernova exploding into a rather low density CSM that encounters a dense shell at a distance of about 0.1 pc, we obtain a low interaction luminosity for ∼7 yr, but a strong rebrightening at this age, due to the supernova ejecta colliding with the circumstellar shell. This collision causes a period (∼2 years) during which the interaction luminosity may dominate the optical emission. The high X-ray flux generated by the collision could once again ionize the outer part of the shell which has not yet been overrun by the forward shock. Consequently the collision might result in a reoccurrence of a narrow Hα emission line, something which has tentatively been seen in SN2004et (Kotak et al. 2009).

The observed width of the narrow Hα emission lines is typically upward of 100 km s^{-1} (e.g Smith et al. 2008b, Prieto et al. 2007). The velocities of the CSM in Model 1 and the velocity of the shell in Model 2 lie well below that (see Fig. 5.3). Velocities upward of a 100 km s^{-1} are hard to explain with the progenitor evolution we investigated. Even if the wind velocity itself might rise above 100 km s^{-1}, as happens during the last phases of the evolution (see Fig. 5.2), the shell that is created by the fast wind sweeping up the material in the surroundings of the star only moves at roughly 50 km s^{-1}.

It is instructive to compare Models 1 and 2, which interact with the same amount of CSM during the first years. However, this material has a r^{-2} density distribution in the first model, while it is all compressed into a dense shell with a radius of 0.1 pc in the second model. We found that in particular the optical emission of Model 2 falls much below that of Model 1. This might seem counter-intuitive since sweeping up material in a dense shell creates an energetic collision when compared to the interaction of supernova ejecta with a CSM in which the density scales with r^{-2}. The lower amount of light emitted is due to a difference that occurs in the shocks. In Model 2 the forward and reverse shock are almost continuously adiabatic, with the exception of the forward shock becoming radiative for a short amount of time during the collision with the shell. In Model 1 the reverse shock is continuously radiative and thus loses a larger amount of energy during the interaction.

In both Model 2 and 3 we found that, depending on the time at which the supernova is observed, the forward and reverse shock can have largely different distances from each other. When observed during or just after the collision with a shell, the two shock are close to each other, while at other times they might be far apart. The proximity of two shocks in observed young supernova remnants is sometimes attributed to the effects of cosmic ray acceleration (e.g Warren et al. 2005), or to the presence of hydrodynamical instabilities (e.g Fraschetti et al. 2010). While the models presented here are not tailored to make predictions regarding any specific supernova, we would like to point out that the presence of shells plays an equally important role in this respect. To be able to fully understand observed shocks, all effects must be taken into account.

We have shown that the occurrence of PDSW during the RSG phase of a star

can alter the CSM of these stars in such a way that the final supernova explosion will be observed as a type IIn explosion in stead of a type IIP. Observations of supernovae like SN1998S and SN1995N seem to agree with this idea. Due to the predicted smooth pre-supernova mass loss of type IIP supernova progenitors, late time observations of X-ray, optical and radio emission from these supernovae is seen as a good test site for investigating the structure of the CSM and the interaction of the supernova ejecta with the CSM (Chevalier & Fransson 1994, Chevalier et al. 2006). While in general this is still true, the PDSW during the RSG phase we have investigated complicates this picture. The CSM structure of a RSG is not necessarily shaped by a free streaming wind, with the density having a smooth r^{-2} power law profile. Type IIP supernova explosions, and the late evolution of their RSG progenitors, might not always be as simple as is often thought.

Acknowledgments

We thank Michael L. Norman and the Laboratory for Computational Astrophysics for the use of ZEUS MP. This work was sponsored by the Stichting Nationale Computerfaciliteiten (National Computing Facilities Foundation, NCF) for the use of supercomputer facilities, with financial support from the Nederlandse Organisatie voor Wetenschappelijk Onderzoek (Netherlands Organisation for Scientific Research, NWO).

Bibliography

Abel, T., Bryan, G. L., & Norman, M. L. 2000, ApJ, 540, 39

Abel, T., Bryan, G. L., & Norman, M. L. 2002, Science, 295, 93

Abel, T., Wise, J. H., & Bryan, G. L. 2007, ApJ, 659, L87

Aldering, G., Antilogus, P., Bailey, S., et al. 2006, ApJ, 650, 510

Alvarez, M. A., Bromm, V., & Shapiro, P. R. 2006, ApJ, 639, 621

Anninos, P., Zhang, Y., Abel, T., & Norman, M. L. 1997, New Astronomy, 2, 209

Aretxaga, I., Benetti, S., Terlevich, R. J., et al. 1999, MNRAS, 309, 343

Arnett, W. D. 1982, ApJ, 253, 785

Baraffe, I., Heger, A., & Woosley, S. E. 2001, ApJ, 550, 890

Bartel, N., Rupen, M. P., Shapiro, I. I., Preston, R. A., & Rius, A. 1991, Nature, 350, 212

Bauer, F. E., Dwarkadas, V. V., Brandt, W. N., et al. 2008, ApJ, 688, 1210

Berger, E., Cenko, S. B., Fox, D. B., & Cucchiara, A. 2009, ApJ, 704, 877

Bietenholz, M. F., Bartel, N., & Rupen, M. P. 2010, ApJ, 712, 1057

Bond, H. E., Bedin, L. R., Bonanos, A. Z., et al. 2009, ApJ, 695, L154

Bond, H. E., Walter, F. M., & Velasquez, J. 2008, IAU Circ., 8946, 2

Borkowski, K., Szymkowiak, A. E., Blondin, J. M., & Sarazin, C. L. 1996, ApJ, 466, 866

Botticella, M. T., Pastorello, A., Smartt, S. J., et al. 2009, MNRAS, 398, 1041

Branch, D. & Tammann, G. A. 1992, ARA&A, 30, 359

Bromm, V., Coppi, P. S., & Larson, R. B. 1999, ApJ, 527, L5

Bromm, V., Ferrara, A., Coppi, P. S., & Larson, R. B. 2001, MNRAS, 328, 969

Bromm, V. & Loeb, A. 2006, ApJ, 642, 382

Bromm, V., Yoshida, N., & Hernquist, L. 2003, ApJ, 596, L135

Cassam-Chenaï, G., Hughes, J. P., Reynoso, E. M., Badenes, C., & Moffett, D. 2008, ApJ, 680, 1180

Chakrabarty, D., Homer, L., Charles, P. A., & O'Donoghue, D. 2001, ApJ, 562, 985

Chen, H., Prochaska, J. X., Bloom, J. S., & Thompson, I. B. 2005, ApJ, 634, L25

Chen, X. & Miralda-Escudé, J. 2004, ApJ, 602, 1

Chevalier, R. A. 1974, ApJ, 188, 501

Chevalier, R. A. 1982, ApJ, 258, 790

Chevalier, R. A. 1987, Nature, 329, 611

Chevalier, R. A. 1997, ApJ, 488, 263

Chevalier, R. A. & Fransson, C. 1994, ApJ, 420, 268

Chevalier, R. A., Fransson, C., & Nymark, T. K. 2006, ApJ, 641, 1029

Chevalier, R. A. & Imamura, J. N. 1982, ApJ, 261, 543

Chevalier, R. A. & Oishi, J. 2003, ApJ, 593, L23

Chugai, N. N. & Chevalier, R. A. 2006, ApJ, 641, 1051

Churchwell, E. 2002, ARA&A, 40, 27

Cioffi, D. F., McKee, C. F., & Bertschinger, E. 1988, ApJ, 334, 252

Cox, D. P. 1972, ApJ, 178, 159

Danchi, W. C., Bester, M., Degiacomi, C. G., Greenhill, L. J., & Townes, C. H. 1994, AJ, 107, 1469

Davidson, K., Gull, T. R., Maran, S. P., et al. 1982, ApJ, 253, 696

de Jager, C., Nieuwenhuijzen, H., & van der Hucht, K. A. 1988, A&AS, 72, 259

DeLaney, T., Rudnick, L., Fesen, R. A., et al. 2004, ApJ, 613, 343

DeLaney, T. A. 2004, Univ. Minnesota

Dwarkadas, V. V. 2005, ApJ, 630, 892

Dwarkadas, V. V. & Chevalier, R. A. 1998, ApJ, 497, 807

Dyson, J. E. & Williams, D. A. 1997, The physics of the interstellar medium (Bristol: Institute of Physics Publishing, 1997. ISBN: 0750303069)

Eldridge, J. J., Genet, F., Daigne, F., & Mochkovitch, R. 2006, MNRAS, 367, 186

Elmhamdi, A., Danziger, I. J., Chugai, N., et al. 2003, MNRAS, 338, 939

Fabian, A. C. & Terlevich, R. 1996, MNRAS, 280, L5

Fesen, R. A. 2001, ApJS, 133, 161

Fesen, R. A., Becker, R. H., & Blair, W. P. 1987, ApJ, 313, 378

Fowler, W. A. & Hoyle, F. 1964, ApJS, 9, 201

Fox, D. W., Lewin, W. H. G., Fabian, A., et al. 2000, MNRAS, 319, 1154

Franco, J., Tenorio-Tagle, G., & Bodenheimer, P. 1990, ApJ, 349, 126

Fransson, C., Chevalier, R. A., Filippenko, A. V., et al. 2002, ApJ, 572, 350

Fraschetti, F., Teyssier, R., Ballet, J., & Decourchelle, A. 2010, A&A, 515, A104+

Fryer, C. L. 1999, ApJ, 522, 413

Gal-Yam, A., Mazzali, P., Ofek, E. O., et al. 2009, Nature, 462, 624

Galli, D. & Palla, F. 1998, A&A, 335, 403

Gao, L., Yoshida, N., Abel, T., et al. 2007, MNRAS, 378, 449

Garcia-Berro, E. & Iben, I. 1994, ApJ, 434, 306

Garcia-Berro, E., Ritossa, C., & Iben, Jr., I. 1997, ApJ, 485, 765

García-Segura, G., Langer, N., & Mac Low, M.-M. 1996a, A&A, 316, 133

García-Segura, G. & Mac Low, M.-M. 1995, ApJ, 455, 160

García-Segura, G., Mac Low, M.-M., & Langer, N. 1996b, A&A, 305, 229

Gotthelf, E. V., Koralesky, B., Rudnick, L., et al. 2001, ApJ, 552, L39

Greif, T. H., Johnson, J. L., Bromm, V., & Klessen, R. S. 2007, ApJ, 670, 1

Hamuy, M., Phillips, M. M., Suntzeff, N. B., et al. 2003, Nature, 424, 651

Hayes, J. C., Norman, M. L., Fiedler, R. A., et al. 2006, ApJS, 165, 188

Heger, A., Fryer, C. L., Woosley, S. E., Langer, N., & Hartmann, D. H. 2003, ApJ, 591, 288

Heger, A., Jeannin, L., Langer, N., & Baraffe, I. 1997, A&A, 327, 224

Heger, A. & Woosley, S. E. 2002, ApJ, 567, 532

Helder, E. A. & Vink, J. 2008, ApJ, 686, 1094

Hillebrandt, W., Nomoto, K., & Wolff, R. G. 1984, A&A, 133, 175

Hirschi, R., Meynet, G., & Maeder, A. 2004, A&A, 425, 649

Houck, J. C., Bregman, J. N., Chevalier, R. A., & Tomisaka, K. 1998, ApJ, 493, 431

Hwang, U., Laming, J. M., Badenes, C., et al. 2004, ApJ, 615, L117

Imamura, J. N., Wolff, M. T., & Durisen, R. H. 1984, ApJ, 276, 667

Janka, H., Langanke, K., Marek, A., Martínez-Pinedo, G., & Müller, B. 2007, Phys. Rep., 442, 38

Johnson, J. L., Greif, T. H., & Bromm, V. 2007, ApJ, 665, 85

Kitaura, F. S., Janka, H., & Hillebrandt, W. 2006, A&A, 450, 345

Kitayama, T. & Yoshida, N. 2005, ApJ, 630, 675

Kitayama, T., Yoshida, N., Susa, H., & Umemura, M. 2004, ApJ, 613, 631

Kosenko, D., Helder, E., & Vink, J. 2010, ArXiv e-prints

Kotak, R., Meikle, W. P. S., Adamson, A., & Leggett, S. K. 2004, MNRAS, 354, L13

Kotak, R., Meikle, W. P. S., Farrah, D., et al. 2009, ApJ, 704, 306

Krause, O., Birkmann, S. M., Usuda, T., et al. 2008, Science, 320, 1195

Kravtsov, A. V. & Gnedin, O. Y. 2005, ApJ, 623, 650

Kudritzki, R. 2000, in The First Stars, ed. A. Weiss, T. G. Abel, & V. Hill, 127–+

Kulkarni, S. R., Ofek, E. O., Rau, A., et al. 2007, Nature, 447, 458

Lamers, H. J. G. L. M. & Cassinelli, J. P. 1999, Introduction to Stellar Winds (Cambridge University Press)

Langer, N. 2009, Nature, 462, 579

Lawrence, S. S., MacAlpine, G. M., Uomoto, A., et al. 1995, AJ, 109, 2635

Leonard, D. C., Filippenko, A. V., Gates, E. L., et al. 2002a, PASP, 114, 35

Leonard, D. C., Filippenko, A. V., Li, W., et al. 2002b, AJ, 124, 2490

Li, Y., Hernquist, L., Robertson, B., et al. 2007, ApJ, 665, 187

Mac Low, M.-M. & Norman, M. L. 1993, ApJ, 407, 207

MacDonald, J. & Bailey, M. E. 1981, MNRAS, 197, 995

Machacek, M. E., Bryan, G. L., & Abel, T. 2001, ApJ, 548, 509

Mackey, J., Bromm, V., & Hernquist, L. 2003, ApJ, 586, 1

Madau, P., Ferrara, A., & Rees, M. J. 2001, ApJ, 555, 92

Maguire, K., di Carlo, E., Smartt, S. J., et al. 2010, MNRAS, 404, 981

Massey, P., Waterhouse, E., & DeGioia-Eastwood, K. 2000, AJ, 119, 2214

McKee, C. F. & Ostriker, J. P. 1977, ApJ, 218, 148

Medvedev, M. V. 2007, Ap&SS, 307, 245

Medvedev, M. V., Lazzati, D., Morsony, B. C., & Workman, J. C. 2007, ApJ, 666, 339

Mesinger, A., Johnson, B. D., & Haiman, Z. 2006, ApJ, 637, 80

Meynet, G., Ekström, S., Maeder, A., et al. 2008, in American Institute of Physics Conference Series, Vol. 990, First Stars III, ed. B. W. O'Shea & A. Heger, 212–216

Meynet, G. & Maeder, A. 2005, A&A, 429, 581

Meynet, G., Maeder, A., Schaller, G., Schaerer, D., & Charbonnel, C. 1994, A&AS, 103, 97

Milisavljevic, D., Fesen, R. A., Leibundgut, B., & Kirshner, R. P. 2008, ApJ, 684, 1170

Miller, A. A., Silverman, J. M., Butler, N. R., et al. 2010, MNRAS, 404, 305

Miyaji, S., Nomoto, K., Yokoi, K., & Sugimoto, D. 1980, PASJ, 32, 303

Morse, J. A., Fesen, R. A., Chevalier, R. A., et al. 2004, ApJ, 614, 727

Nomoto, K. 1984, ApJ, 277, 791

Nomoto, K. 1987, ApJ, 322, 206

Nomoto, K., Sugimoto, D., Sparks, W. M., et al. 1982, Nature, 299, 803

Nugis, T. & Lamers, H. J. G. L. M. 2000, A&A, 360, 227

Oh, S. P., Cooray, A., & Kamionkowski, M. 2003, MNRAS, 342, L20

Oort, J. H. 1951, in Problems of Cosmical Aerodynamics, 118–+

O'Shea, B. W., Abel, T., Whalen, D., & Norman, M. L. 2005, ApJ, 628, L5

O'Shea, B. W., Bryan, G., Bordner, J., et al. 2004, ArXiv Astrophysics e-prints

O'Shea, B. W. & Norman, M. L. 2007, ApJ, 654, 66

O'Shea, B. W. & Norman, M. L. 2008, ApJ, 673, 14

Pastorello, A., Della Valle, M., Smartt, S. J., et al. 2007a, Nature, 449

Pastorello, A., Smartt, S. J., Mattila, S., et al. 2007b, Nature, 447, 829

Pastorello, A., Valenti, S., Zampieri, L., et al. 2009, MNRAS, 394, 2266

Pastorello, A., Zampieri, L., Turatto, M., et al. 2004, MNRAS, 347, 74

Patnaude, D. J. & Fesen, R. A. 2008, ArXiv e-prints

Peebles, P. J. E. 1984, ApJ, 277, 470

Peebles, P. J. E. & Dicke, R. H. 1968, ApJ, 154, 891

Pérez-Rendón, B., García-Segura, G., & Langer, N. 2009, ArXiv e-prints

Pérez-Torres, M. A., Alberdi, A., Marcaide, J. M., et al. 2002, MNRAS, 335, L23

Pinto, P. A. & Eastman, R. G. 2001, New Astronomy, 6, 307

Poelarends, A. J. T., Herwig, F., Langer, N., & Heger, A. 2008, ApJ, 675, 614

Pooley, D., Lewin, W. H. G., Fox, D. W., et al. 2002, ApJ, 572, 932

Prieto, J. L., Garnavich, P. M., Phillips, M. M., et al. 2007, ArXiv e-prints

Prieto, J. L., Kistler, M. D., Thompson, T. A., et al. 2008, ApJ, 681, L9

Prochaska, J. X., Chen, H., & Bloom, J. S. 2006, ApJ, 648, 95

Prochaska, J. X., Chen, H., Dessauges-Zavadsky, M., & Bloom, J. S. 2007, ApJ, 666, 267

Puls, J., Vink, J. S., & Najarro, F. 2008, A&A Rev., 16, 209

Pumo, M. L., Turatto, M., Botticella, M. T., et al. 2009, ApJ, 705, L138

Qiu, J., Shu, C., Liu, J., & Fang, L. 2008, New Astronomy, 13, 1

Quimby, R. M., Kulkarni, S. R., Kasliwal, M. M., et al. 2009, ArXiv e-prints

Reed, J. E., Hester, J. J., Fabian, A. C., & Winkler, P. F. 1995, ApJ, 440, 706

Ricotti, M., Gnedin, N. Y., & Shull, J. M. 2001, ApJ, 560, 580

Rodríguez, L. F. 2005, in IAU Symposium, Vol. 227, Massive Star Birth: A Crossroads of Astrophysics, ed. R. Cesaroni, M. Felli, E. Churchwell, & M. Walmsley, 120–127

Scannapieco, E., Madau, P., Woosley, S., Heger, A., & Ferrara, A. 2005, ApJ, 633, 1031

Schaerer, D. 2002, A&A, 382, 28

Schaller, G., Schaerer, D., Meynet, G., & Maeder, A. 1992, A&AS, 96, 269

Schlegel, E. M. & Petre, R. 2006, ApJ, 646, 378

Schure, K. M., Vink, J., García-Segura, G., & Achterberg, A. 2008, ApJ, 686, 399

Sedov, L. I. 1959, Similarity and Dimensional Methods in Mechanics (Academic Press)

Siess, L. 2007, A&A, 476, 893

Smartt, S. J. 2009, ARA&A, 47, 63

Smith, B., Sigurdsson, S., & Abel, T. 2008a, MNRAS, 385, 1443

Smith, B. D. & Sigurdsson, S. 2007, ApJ, 661, L5

Smith, N., Chornock, R., Li, W., et al. 2008b, ApJ, 686, 467

Smith, N., Ganeshalingam, M., Chornock, R., et al. 2009, ApJ, 697, L49

Smith, N., Li, W., Filippenko, A. V., & Chornock, R. 2010, ArXiv e-prints

Smith, N., Li, W., Foley, R. J., et al. 2007, ApJ, 666, 1116

Smith, N. & McCray, R. 2007, ApJ, 671, L17

Soderberg, A. M., Berger, E., Page, K. L., et al. 2008, Nature, 453, 469

Stockdale, C. J., Van Dyk, S. D., Sramek, R. A., et al. 2004, IAU Circ., 8282, 2

Stone, J. M. & Norman, M. L. 1992, ApJS, 80, 753

Tammann, G. A. & Schroeder, A. 1990, A&A, 236, 149

Tananbaum, H. 1999, IAU Circ., 7246, 1

Taylor, G. 1950, Royal Society of London Proceedings Series A, 201, 159

Tegmark, M., Silk, J., & Evrard, A. 1993, ApJ, 417, 54

Temple, R. F., Raychaudhury, S., & Stevens, I. R. 2005, MNRAS, 362, 581

Thompson, T. A., Prieto, J. L., Stanek, K. Z., et al. 2009, ApJ, 705, 1364

Thorstensen, J. R., Fesen, R. A., & van den Bergh, S. 2001, AJ, 122, 297

Tominaga, N., Umeda, H., & Nomoto, K. 2007, ApJ, 660, 516

Truelove, J. K. & McKee, C. F. 1999, ApJS, 120, 299

Trundle, C., Kotak, R., Vink, J. S., & Meikle, W. P. S. 2008, A&A, 483, L47

Turatto, M., Cappellaro, E., Danziger, I. J., et al. 1993, MNRAS, 262, 128

van den Bergh, S. & Kamper, K. 1985, ApJ, 293, 537

van Loon, J. T., Marshall, J. R., & Zijlstra, A. A. 2005, A&A, 442, 597

van Veelen, B., Langer, N., & Kotak, R. 2010 in prep., Chapter 4

Vink, J. 2004, New Astronomy Review, 48, 61

Vink, J., Bloemen, H., Kaastra, J. S., & Bleeker, J. A. M. 1998, A&A, 339, 201

Vink, J., Kaastra, J. S., & Bleeker, J. A. M. 1996, A&A, 307, L41

Vink, J. S., de Koter, A., & Lamers, H. J. G. L. M. 2001, A&A, 369, 574

Vishniac, E. T. 1983, ApJ, 274, 152

Voit, G. M. 1996, ApJ, 465, 548

Wanajo, S., Nomoto, K., Janka, H., Kitaura, F. S., & Müller, B. 2009, ApJ, 695, 208

Warren, J. S., Hughes, J. P., Badenes, C., et al. 2005, ApJ, 634, 376

Weaver, R., McCray, R., Castor, J., Shapiro, P., & Moore, R. 1977, ApJ, 218, 377

Weiler, K. W., Panagia, N., & Sramek, R. A. 1990, ApJ, 364, 611

Weinmann, S. M. & Lilly, S. J. 2005, ApJ, 624, 526

Whalen, D., Abel, T., & Norman, M. L. 2004, ApJ, 610, 14

Whalen, D. & Norman, M. L. 2006, ApJS, 162, 281

Whalen, D. & Norman, M. L. 2008a, ApJ, 673, 664

Whalen, D., van Veelen, B., O'Shea, B. W., & Norman, M. L. 2008, ApJ, 682, 49

Whalen, D. J. & Norman, M. L. 2008b, ApJ, 672, 287

Williams, C. L., Panagia, N., Van Dyk, S. D., et al. 2002, ApJ, 581, 396

Willingale, R., Bleeker, J. A. M., van der Heyden, K. J., & Kaastra, J. S. 2003, A&A, 398, 1021

Willingale, R., Bleeker, J. A. M., van der Heyden, K. J., Kaastra, J. S., & Vink, J. 2002, A&A, 381, 1039

Wise, J. H. & Abel, T. 2005, ApJ, 629, 615

Wise, J. H. & Abel, T. 2007, ApJ, 671, 1559

Wise, J. H. & Abel, T. 2008a, ApJ, 684, 1

Wise, J. H. & Abel, T. 2008b, ApJ, 685, 40

Woltjer, L. 1972, ARA&A, 10, 129

Woosley, S. E., Blinnikov, S., & Heger, A. 2007, Nature, 450, 390

Woosley, S. E., Heger, A., & Weaver, T. A. 2002, Reviews of Modern Physics, 74, 1015

Woosley, S. E., Langer, N., & Weaver, T. A. 1993, ApJ, 411, 823

Yoon, S. & Cantiello, M. 2010, ApJ, 717, L62

Yoshida, N., Oh, S. P., Kitayama, T., & Hernquist, L. 2007, ApJ, 663, 687

Young, D. R., Smartt, S. J., Valenti, S., et al. 2010, A&A, 512, A70+

Young, P. A., Fryer, C. L., Hungerford, A., et al. 2006, ApJ, 640, 891

Nederlandse Samenvatting

Wanneer een ster zwaarder is dan ongeveer acht keer de massa van onze zon zal deze aan het einde van zijn leven ontploffen. Deze ontploffing wordt ook wel een supernova (meervoud: supernovae) genoemd. Als gevolg van de supernova vliegen de buitenste lagen van de ster met enorme snelheden van soms wel meer dan 10 000 km/s weg. Afhankelijk van de precieze massa van de ster aan het begin van zijn leven zal deze na de supernova een neutronenster of een zwart gat achterlaten.

De buitenste lagen van de ster, die door de ontploffing het heelal worden ingeslingerd, bewegen met een enorme snelheid. Na verloop van tijd zal de materie die al in de omgeving van de ster was voordat de explosie plaatsvond, opgeveegd worden door deze buitenste lagen. De manier waarop de materie in de omgeving van de ster is verdeeld, beinvloedt hoe de omgeving van de ster (het supernova restant) er uit gaat zien na de explosie.

Niet alleen tijdens de supernova explosie maar ook al gedurende zijn leven heeft de ster materie uitgestoten. Dit is gebeurd door middel van een stellaire wind. Dit is een stroom van heet gas dat van het oppervlak van de ster wordt geblazen. Als gevolg van deze uitstoot kan de omgeving van de ster sterk veranderen. In dit proefschrift kijken we naar hoe de omgeving van de ster, die de ster zelf heeft veranderd, de evolutie van de supernova explosie en van het supernova restant beïnvloedt.

De evolutie van een ster

Een ster zal ongeveer gedurende de eerste 90% van zijn leven in zijn kern waterstof fuseren tot helium. Deze fase heet de hoofdreeks fase. De energie die bij de fusie vrijkomt, is nodig om te compenseren voor het energieverlies dat optreedt aan het oppervlak van de ster, in de vorm van de straling die wij zien.

Tijdens de hoofdreeks fase heeft de ster een stellaire wind, die materie van het oppervlak van de ster wegblaast. Dit gaat sneller dan de geluidssnelheid in de omgeving van de ster en daardoor onstaat er een schok. De stellaire wind veegt de omringende materie op in een dunne schil die naar buiten beweegt. Hierdoor ontstaat er een bel rondom de ster, waarbinnen er nog maar zeer weinig materie is.

Na de hoofdreeks fase zwelt de ster op en vormt een rode reus. De wind van de ster zal gedurende deze fase afnemen in snelheid maar toenemen in dichtheid, waardoor er een tweede schil ontstaat. In veel gevallen is deze fase de laatste in het leven van de ster en ontploft hij dus wanneer hij een rode reus is. Wanneer de ster aan het begin van zijn leven echter zwaarder is dan ongeveer 30 keer de massa van

de zon dan kan er nog een fase komen, waarin de stellaire wind weer verandert. Hierdoor kunnen er nog meer schillen gevormd worden of kunnen er schillen die al eerder gevormd zijn, vernietigd worden.

De ster stoot over het algemeen in alle richtingen evenveel matarie uit in de stellaire wind. Dit wekt de verwachting dat de verandering van de omgeving in alle richtingen hetzelfde zal blijven, ofwel de omgeving is sferisch symmetrisch. Echter, de schillen die gevormd worden in de verschillende fases van de stellaire wind hoeven niet noodzakelijk sferisch symmetrisch te blijven. Door instabiliteiten in een schil kan hij kapot gaan en zich opsplitsen in een groot aantal kleinere gebieden waar zich dan een klont materie bevindt. Deze klontering laat een specifiek beeld achter wanneer de materie van de supernova explosie hier een interactie mee heeft.

De supernova explosie

De minimum massa van ongeveer acht keer de massa van onze zon is nodig om een supernova explosie te vormen, omdat dit minimum ervoor zorgt dat in de kern van de ster alle fases van kernfusie kunnen plaatsvinden. Gedurende zijn leven zal een ster beginnen met het fuseren van waterstof. Daarna volgt de fusie van helium, koolstof, neon, zuurstof en uiteindelijk silicium. Aan het einde van al deze fusiereacties zal de kern van de ster bestaan uit ijzer. Zodra dit het geval is kan de ster geen energie meer verkrijgen door het fuseren van ijzeratomen tot een nog zwaarder atoom en zal de fusie stoppen.

In de kern van de ster is er gedurende het leven van de ster altijd een evenwicht tussen de zwaartekracht - die alles naar het centrum probeert toe te trekken - de druk van het gas in de kern en ook de druk die vrijkomt als gevolg van het fusieproces. Wanneer het fusieproces in de kern stopt, valt dus een deel van de druk weg. Het uiteindelijke gevolg is dat de kern van de ster eerst een implosie ondergaat en iets later een explosie: de supernova.

De materie die wordt uitgestoten tijdens de explosie wordt met snelheden van soms wel meer dan 10 000 km/s het heelal ingeslingerd. De veranderingen die de ster in zijn omgeving heeft veroorzaakt hebben invloed op wat er precies gebeurt met de supernova materie. Wanneer de supernova materie zich voortbeweegt in een omgeving waarin alles heel gelijkmatig is verdeeld dan zal de interactie heel geleidelijk plaatsvinden. Als gevolg hiervan zal het licht dat wij zien van de interactie van de supernova materie met de omgeving geen plotselinge veranderingen bevatten. Wanneer de supernova materie echter ineens botst met een massieve schil, zal de hoeveelheid licht die we zien ineens sterk toenemen.

Dit proefschrift

Om de interactie van supernovae met hun omgeving te bekijken hebben we in dit proefschrift gebruik gemaakt van een hydrodynamische code. Deze hydrodynamische code is gebruikt om computermodellen te maken van alle gassen en de bewegingen van deze gassen, die we vervolgens analyseren en vergelijken met waarnemingen. Omdat het uitvoeren van deze berekeningen erg veel rekentijd kost op

een computer, maken we vaak versimpelde aannames. In realiteit is alles natuurlijk driedimensionaal. In het computermodel volstaat het echter vaak om maar in twee of soms zelfs maar één dimensie te rekenen. Er treden dan echter wel andere problemen op. In één dimensionale berekeningen is het niet mogelijk om de instabiliteiten die optreden in schillen mee te nemen. Wanneer deze een belangrijke rol spelen is het dus onmogelijk om maar één dimensie te gebruiken.

Hoofdstuk 2: De hydrodynamica van de supernova restant Cassiopeia A

De supernova restant Cassiopeia A is een van de meest waargenomen en daarom ook best bestudeerde supernova restanten. Er zijn echter nog steeds open vragen over de voorloper van deze supernova restant. Hoe is de evolutie van de ster die deze restant heeft gemaakt verlopen? Één van de vragen is of de ster wel of geen Wolf-Rayet fase heeft gehad. Deze Wolf-Rayet fase volgt op de rode reus fase en zorgt voor een schil met materie in de omgeving, die naarmate hij zich verder voortbeweegt steeds klonteriger wordt. In de waarnemingen van de supernova restant zijn er klonten met materie gezien die overeen zouden kunnen komen met de klonten die ontstaan in de schil van de Wolf-Rayet fase. Uit ons onderzoek bleek echter dat deze overeenkomst niet klopte. Al was het mogelijk om de schokstructuur van de supernova restant ruwweg kloppend te krijgen wanneer we een Wolf-Rayet fase toelieten, het bleek dat de verdeling van de klonten en hun snelheden uit onze modellen niet overeenkwamen met de waarnemingen. Onze conclusie was dan ook dat de voorloper van deze supernova restant geen Wolf-Rayet fase heeft gehad.

Hoofdstuk 3: De vernietiging van kosmologische minihalos door de oudste supernovae

De eerste sterren in het vroege heelal hadden een erg belangrijke rol. Ze bevonden zich een een massieve halo van materie waarbinnen zij explodeerden. Vanwege de enorme massa van deze halo werd vaak gedacht dat een supernova explosie er niet voor zou kunnen zorgen dat de supernova materie ver buiten de halo verspreid kon worden. De materie van deze sterren is echter van groot belang voor de vorming van de tweede generatie sterren, omdat deze supernova materie veel zware elementen bevat. Omdat de eerste sterren nog helemaal geen zware atomen bevatten hebben ze geen stellaire wind. De ionizerende straling die van het oppervlak van de ster af komt gedurende zijn leven daarom de belangrijkste rol. Als gevolg van de veranderende druk die onstaat door de ionizerende straling worden de binnenste regionen van de halo opgeveegd en wordt het voor de supernova materie in eerste instantie makkelijker om zich te verspreiden. Ons onderzoek laat een aantal verschillende modellen zien, waarbij wordt gekeken naar verschillende halo's en verschillende supernova explosies. In specifieke gevallen kan de supernova materie de complete halo vernietigen.

Hoofdstuk 4: De omgevingsinteractie van electron vangst supernovae

Wanneer een ster maar net iets meer dan acht keer de massa van de zon weegt, verloopt de evolutie en de explosie van deze ster anders dan voor 'normale' sterren. Aan het einde van het leven van de ster is er een sterke toename in het massaverlies van de ster, waardoor er een grote hoeveelheid materie relatief dichtbij de ster te vinden is. De energie die gepaard gaat met de supernova explosie is in dit geval echter een factor 10 kleiner dan normaal. Uit ons onderzoek bleek dat, hoewel de energie een factor 10 kleiner was dan normaal, de hoeveelheid licht dat we zien van dit soort explosies vergelijkbaar is met de hoeveelheid licht dat we zien van normale explosies. We hebben onze resultaten ook vergeleken met een aantal waargenomen supernovae. Sommige van deze waarnemingen vertonen sterke vergelijkenis met de resultaten van onze modellen.

Hoofdstuk 5: Pulserende rode reuzen als mogelijke voorlopers van type IIn supernovae

In sommige gevallen kunnen sterren tijdens hun rode reus fase een verhoogd massaverlies hebben van hun stellaire wind, omdat ze pulseren. Dit mechanisme is recentelijk in meer detail bestudeerd en is in dit hoofdstuk voor het eerst toegepast op de evolutie van de omgeving van de pulserende rode reus. Omdat het mechanisme dat het verhoogde massa verlies veroorzaakt nog niet heel goed bekend is, hebben we gevariëerd in de tijd tussen het einde van de pulserende fase en de supernova explosie. Deze variatie komt ruwweg overeen met een variatie in de massa die de ster had aan het begin van zijn leven. De modellen zijn vervolgens vergeleken met de waarnemingen van type IIn supernovae. Deze supernovae kenmerken zich door de aanwezigheid van een sterke en smalle spectraallijn die van waterstof afkomstig is. Omdat deze spectraallijn heel nauw is, moet hij wel afkomstig zijn van de materie rond de supernova explosie. Dit betekent dus dat de supernova explosie ons een beeld geeft van de omgeving van de ster die gevormd is voorafgaand aan de supernova explosie. Zodra de materie in de omgeving een interactie heeft met de supernova materie zal deze spectraallijn verdwijnen. Aan de hand van onze theoretische modellen hebben we kunnen aantonen dat het mogelijk is dat sommige van deze pulserende rode reuzen inderdaad de voorlopers kunnen zijn van dit soort supernovae.

Acknowledgments / Dankwoord

To Be Done

Curriculum Vitae

I was born on May 22 1983 in Nijmegen, The Netherlands. From 1995 untill 2001 I attended high school at the Lorentz College in Arnhem, where I received my VWO diploma.

My interest in astrophysics led me to University Utrecht where I started my studies in 2001. During the final year of my Master's studies in 2006 I started working on my thesis under the supervision of Prof. dr. Norbert Langer. This work continued during my time as a Ph.D student, which started in November 2006. As Ph.D student I was given the opportunity to visit Los Alamos National Laboratory for 6 weeks in 2007 to work as a Graduate Research Assistant. In Los Alamos, at conferences I have visited during the last four years and at the Sterrenkundig Instituut Utrecht I have presented my research and shared the knowledge with the scientific community. The work done during my Ph.D studies has ultimately resulted in this thesis: 'Supernovae Interacting with their Circumstellar Medium'.